Surface acoustic waves as testbed for electron flying qubits

Junliang Wang Wang

Université Grenoble Alpes

THÈSE

Pour obtenir le grade de

DOCTEUR DE L'UNIVERSITÉ GRENOBLE ALPES

Spécialité : PHYSIQUE APPLIQUEE

Arrêté ministériel : 25 mai 2016

Présentée par

Junliang WANG WANG

Thèse dirigée par **Christopher BÄUERLE**, Université Grenoble Alpes

préparée au sein de **l'Institut Néel - CNRS**
dans **l'École Doctorale Physique**

Ondes acoustiques de surface comme banc d'essai pour les qubits volants d'électrons

Surface acoustic waves as testbed for electron flying qubits

Thèse soutenue publiquement le **27 juin 2022**,
devant le jury composé de :

Monsieur Hubert KRENNER
Professeur, Westfälische Wilhelms-Universität Münster, Rapporteur
Monsieur Christian GLATTLI
Ingénieur HDR, CEA Centre de Paris-Saclay, Rapporteur
Monsieur Andrew CLELAND
Professeur, University of Chicago, Examinateur
Madame Saskia FISCHER
Professeur, Humboldt-Universität zu Berlin, Examinatrice
Monsieur Hervé COURTOIS
Professeur des Universités, Université Grenoble Alpes, Présidente

Abstract

Besides their massive use in telecommunication industry, surface acoustic waves (SAWs) are finding more and more impressive applications in quantum science. Using in particular a surface-gate-defined nanocircuit, a SAW can transport a single electron between distant quantum dots. This capability enabled to perform SAW-driven electron-quantum-optics experiments at the single-particle level. The maturity of the essential building blocks such as highly efficient single-electron source and detector, on-demand in-flight partitioning and precise synchronization of multiple sources, makes the SAW-assisted flying electron a promising candidate for quantum information processing.

In this work, we investigate the feasibility of quantum logic implementations with SAW-driven flying electrons. We exploit in particular the charge degree of freedom using a single-electron circuit with two coupled transport channels. We first develop an electrostatic modeling tool to optimize the surface-gate design of the electronic nanocircuit. Benchmarking the simulations with a large experimental dataset, we validate the predictive power of our electrostatic model for semiconductor nanodevices.

Employing the optimized single-electron circuit with a coupled quantum rails, we investigate the electron-electron interaction between a synchronized pair of flying electrons. We perform in particular Hong-Ou-Mandel interferometry by sending two electrons in the same or different SAW minima. By contrasting the full-counting statistics from single-shot measurements, we observe an increased antibunching probability up to 80 %. Using numerical electrostatic simulations, we find that Coulomb interaction plays the dominant role. Estimating the interaction strength between the flying electrons, we anticipate its application for two-qubit-gate implementations.

Aiming at coherent in-flight manipulations, we have developed a novel technique to control the quantum state of a flying electron in real time. Specifically, we apply tailored voltage pulses to the tunnel barrier to turn on or off the coupling on demand. Preliminary results show already signatures of electron dynamics during its propagation. The demonstration of this time-resolved technique lays the groundwork for quantum logic implementations of SAW-assisted flying electrons.

Finally, we present a novel SAW engineering method to generate a single, strongly compressed acoustic pulse. Using this on-demand SAW pulse to transfer a single electron in a linear channel, we observe a competitive transport efficiency exceeding 99 %. The demonstrated synthesis technique paves the way for a SAW-driven platform of single-electron transport that is precise, synchronized and scalable.

L'abrégé

Outre leur utilisation massive dans l'industrie des télécommunications, les ondes acoustiques de surface (SAW) trouvent des applications de plus en plus impressionnantes en science quantique. En utilisant en particulier un nanocircuit défini par une grille de surface, une onde acoustique de surface peut transporter un électron unique entre des boîtes quantiques distantes. Cette capacité a permis de réaliser des expériences d'optique quantique électronique au niveau de la particule unique à l'aide de SAW. La maturité des éléments constitutifs essentiels tels que la source et le détecteur d'électrons uniques hautement efficaces, le partitionnement en vol à la demande et la synchronisation précise de sources multiples, fait de l'électron volant assisté par SAW un candidat prometteur pour le traitement de l'information quantique.

Dans ce travail, nous étudions la faisabilité de l'implémentations de logique quantique avec des électrons volants pilotés par SAW. Nous exploitons en particulier le degré de liberté de la charge en utilisant un circuit à un seul électron avec deux canaux de transport couplés. Nous développons d'abord un outil de modélisation électrostatique afin d'optimiser la conception grille de surface du nanocircuit électronique. En comparant les simulations avec un grand ensemble de données expérimentales, nous validons le pouvoir prédictif de notre modèle électrostatique pour des nanodispositifs semi-conducteurs.

En utilisant le circuit optimisé à électron unique avec des rails quantiques couplés, nous étudions l'interaction électron-électron entre une paire synchronisée d'électrons volants. Nous réalisons en particulier l'interférométrie de Hong-Ou-Mandel en envoyant deux électrons dans le même minimum de la SAW ou dans des minima différents. En comparant les statistiques de comptage complet à partir de mesures à monocoup, nous observons une augmentation de la probabilité d'antibunching jusqu'à 80 %. En utilisant des simulations électrostatiques numériques, nous trouvons que l'inte-raction de Coulomb joue le rôle dominant. En estimant la force d'interaction entre les électrons volants, nous anticipons son application pour les implémentations de portes logiques à deux qubits.

Dans le but de réaliser des manipulations cohérentes en vol, nous avons développé une nouvelle technique pour contrôler l'état quantique d'un électron volant en temps réel. Plus précisément, nous appliquons des impulsions de tension à la barrière tunnel pour activer ou désactiver le couplage à la demande. Les résultats prélimi-naires montrent déjà des signatures de la dynamique de l'électron pendant sa propagation. La démonstration de cette technique résolue en temps réel jette les bases de la mise en œuvre de la logique quantique des électrons volants assistés par SAW.

Enfin, nous présentons une nouvelle méthode d'ingénierie SAW pour générer une impulsion acoustique unique et fortement compressée. En utilisant cette impulsion SAW à la demande pour transférer un électron unique dans un canal

linéaire, nous observons une efficacité de transport compétitive dépassant 99 %. La technique de synthèse démontrée ouvre la voie à une plateforme de transport d'électrons uniques pilotée par SAW, précise, synchronisée et évolutive.

Contents

List of publications

[Wan22b]
"Generation of a single-cycle acoustic pulse: A scalable solution for transport in single-electron circuits"
J. Wang*, S. Ota*, H. Edlbauer*, *et al.*
Physical Review X **12**, 031035 (2022)

[Edl22]
"Semiconductor-based electron flying qubits: Review on recent progress accelerated by numerical modelling"
H. Edlbauer, **J. Wang**, *et al.*
EPJ Quantum Technology **9**, 21 (2022)

[Edl21]
"In-flight distribution of an electron within a surface acoustic wave"
H. Edlbauer, **J. Wang**, *et al.*
Applied Physics Letters **119**, 114004 (2021) – Editor's pick

[Tak19]
"Sound-driven single-electron transfer in a circuit of coupled quantum rails"
S. Takada, H. Edlbauer, H. V. Lepage, **J. Wang**, *et al.*
Nature Communications **10**, 4557 (2019)

[Wan22a]
"Coulomb-mediated antibunching of an electron pair surfing on sound"
J. Wang, *et al.*
(In preparation)

[Cha22]
"Unveiling the charge distribution of a GaAs-based nanoelectronic device: A large experimental data-set approach"
E. Chatzikyriakou*, **J. Wang***, *et al.*
(Submitted; see preprint arXiv:2205.00846)

* equal contribution

List of abbreviations

2DEG	two-dimensional electron gas
AB	Aharonov–Bohm
AlGaAs	aluminium gallium arsenide
a.u.	arbitrary unit
AWG	arbitrary waveform generator
DAC	digital-to-analog converter
DC	direct current; constant bias
EM	electromagnetic
FFT	fast Fourier transform
FPGA	field-programmable gate array
FWHM	full width at half maximum
GaAs	gallium arsenide
GS/s	giga-sampling per second
HBT	Hanbury-Brown-Twiss
HOM	Hong-Ou-Mandel
IDT	interdigital transducer
IPA	isopropanol
MIBK	Methyl isobutyl ketone
MZ	Mach–Zehnder
NMP	N-methyl-2-pyrrolidon
OM	optical microscopy
OSC	oscilloscope
PCB	printed circuit board
PMMA	poly(methyl methacrylate)
QD	quantum dot
QPC	quantum point contact
RF	radio frequency; 20 kHz to 300 GHz
SAW	surface acoustic wave
SEM	scanning electron microscopy
SEP	single-electron pump
TCW	tunnel-coupled wire
VNA	vector network analyzer

List of constants

e	elementary charge, $e \approx 1.60 \cdot 10^{-19}$ C
G_0	quantum conductance, $G_0 = 2e^2/h \approx 7.75 \cdot 10^{-5}\ \Omega^{-1}$
h	Planck constant, $h \approx 4.14 \cdot 10^{-15}$ eV s
$\hbar$	Reduced Planck constant, $\hbar = h/(2\pi)$
m_0	free electron rest mass, $m_0 \approx 9.11 \cdot 10^{-31}$ kg
m_e	effective electron mass in a GaAs crystal, $m_e \approx 0.067 \cdot m_0$
μ_B	Bohr magneton, $\mu_\mathrm{B} = e \cdot \hbar/(2m) \approx 5.78 \cdot 10^{-5}$ eV/T
ε_0	vacuum permitivity, $\varepsilon_0 \approx 8.85 \cdot 10^{-12}$ F m^{-1}
ε_r	relative dielectric constant of GaAs, $\varepsilon_r \approx 12.88$

Introduction

In the early twentieth century, the idea of energy quantization introduced by Max Planck dramatically changed our interpretation of Nature. This concept was so radically different from the deterministic description that one of the founders of quantum mechanics, Erwin Schrödinger, said "I do not like it, and I am sorry I ever had anything to do with it"[1]. Despite his rejection, countless experimental observations such as the quantum tunneling effect, remote entanglement or superconductivity have been validating over and over again this counter-intuitive description of our universe.

After the birth of quantum physics, the focus was not only on fundamental investigations, but also on harnessing the quantum properties for real applications. In the field of semiconductors in particular, the invention of the modern transistor [Bar56; Bra56; Sho56] marked the beginning of the *second quantum revolution* [DM03]. Understanding the photon emission led to the development of lasers [MAI60]; investigations on the nuclear magnetic moment [Rab38] stimulated the invention of the Magnetic Resonance Imaging (MRI); and the first demonstration of an atomic clock [Mar58] triggered the redefinition of the second and the realization of the Global Positioning System (GPS). These are just few examples of the myriad benefits obtained by exploiting the fundamental laws of physics.

Particularly in information processing, two theoretical breakthroughs by P. Shor [Sho94] and L. K. Grover [Gro96] sparked the interest in a brand new approach to solve computing algorithms. Rather than storing the information as a binary digit, *i.e.* bit, the superposition of quantum states allows to have 0 and 1 *at the same time*. This novel building bock is known as a *qubit*. Harnessing the quantum entanglement or, in words of Einstein, the "spooky action at a distance" [EBB71], parallel processing of entangled qubits enables for instance exponentially faster computation algorithms than their classical counterparts [NC09].

The first experimental realization of a qubit came soon after. Groups led by S. Haroche [Bru96] and D. J. Wineland [Mee96] independently manipulated the quantum state of a single photon and a single ion, respectively. These outstanding demonstrations initiated the race towards building the so-called quantum computer.

At the beginning of this century, DiVincenzo proposed a set of criteria for physically implementing a quantum computer [DiV00]. In short, the state of each qubit needs to be prepared, manipulated and measured with high fidelity,

[1] `https://shorts.quantumlah.org/quantum-quotes`

and faster than the decoherence time. Moreover, we have to be able to entangle multiple qubits in a scalable architecture. From this perspective, one of the main challenge is to achieve an accurate interplay between the qubit isolation from the environment and the on-demand coupling to external influences to manipulate and to readout the quantum state.

In order to fulfill these criteria, a variety of qubits has been proposed and realized [Lad10]. Examples of promising platforms include superconducting junctions [NPT99; DWM04; Aru19], defects in diamonds [Dut07; Neu08; Wan20], trapped ions [Win98; Wri19], neutral atoms [MO06], nanomechanical systems [PCB21], electron charge [Hay03; Fuj04; Pet10] or spin qubits [Pet05; Han07; Liu08; Sim09; Zwa13; Mau16; GZ21].

In the aforementioned approaches, the information is stored *stationary* in a quantum node. Following this classification, there is another kind of qubit where the quantum state manipulation is performed during propagation. One of the main advantage of such *flying* qubits is the simplified connectivity between quantum nodes for a scalable quantum computer.

The photon is a natural candidate as a flying qubit. Owing to the advanced field of quantum optics, photonic circuits represent a promising alternative for quantum logic implementations [KLM01; O'B03; BL05; PMO09; Car15]. Such a photon-based platform has however two major drawbacks. First, although the bosonic nature enables long decoherence time, achieving interaction between photons for multi-qubit operations represents a challenging task. Second, the circuit performance is currently limited by the efficiency of the single-photon sources [Eng13; Pae20] and detectors [Naj14; ASY15].

Similar to the linear-optics approach, it was proposed to use electrons in semiconductor solid-state devices as flying qubits [Ber00; IAU01]. Such an implementation requires the following building blocks: single-electron source and detector, an adiabatic and coherent transport medium, a tunable beam splitter and a phase shifter. Outstanding progress has been shown during the last decade [Bäu18; Edl22] that involves mesoscopic capacitors [Fèv07; FDJ08; Boc13; Bar20], single-electron pumps (SEP) [Blu07; Fle13; Ubb14; Fle19; Fre20] and exotic quasiparticles called levitons [Dub13; Jul14; Gla20]. Except for SEP [Fre20], the present lack of a single-electron detector however limits these platforms to realize the electron-flying-qubit scheme at a single-particle level.

To accomplish this goal, surface acoustic waves (SAW) emerged as a promising candidate [BSR00; For17; Bäu18; Edl22]. The associated potential modulation can confine and transfer single electrons between distant quantum dots [Her11; McN11]. The combination of surface-gate defined structures and non-invasive electrometers [Fie93] allow the isolation and the detection of single electrons with near-unity efficiency. To implement the quantum logic architecture, our

group has investigated recently a SAW-driven circuit of coupled transport paths [Tak19]. Using this setup, three important milestones were achieved: highly-efficient single-electron transport exceeding 99 %, on-demand partitioning of a flying electron and a synchronization method for multiple single-electron sources.

For the realization of a SAW-driven electron flying qubit, there are still however two missing building blocks. First, the preparation of a coherent superposition state of a single flying electron; and second, the observation of in-flight interaction between a synchronized electron pair. Overcoming these challenges is the scope of this thesis, which brings us to the outline of the present manuscript.

In Chapter 1, we introduce the relevant concepts related to a flying qubit based on the electron charge. We briefly review the state of the art, with especial emphasis on the electron transport based on quantum Hall effect, levitons and surface acoustic waves. Chapter 2 focuses on the semiconductor GaAs/AlGaAs heterostructure that is employed in all the presented experiments. We have developed in particular a predictive electrostatic model for surface-gate defined nanodevices. Chapter 3 describes in details the characterization and simulation methods for our single-electron transport mechanism: surface acoustic waves. In Chapter 4, we explain the experimental setup for the investigations of in-flight manipulations. We start by presenting the sample design process, nanofabrication, cryogenics and electrical characterizations. We then describe the employed calibration protocols for single-electron transport in the optimized circuit of coupled quantum rails. In Chapter 5, we present our investigations on electron-electron interaction by performing collision experiments with a synchronized electron pair. With the aid of numerical simulations, we identify the main mechanism of in-flight interaction and discuss its applicability for quantum entanglement. Chapter 6 shows preliminary measurements towards in-flight quantum state manipulations in the currently investigated sample. Specifically, we apply sub-nanosecond voltage pulses on a central barrier gate to dynamically control the coupling in *real time*. Finally, Chapter 7 focuses on solving an intrinsic limit of SAW related to its spatial extend. We demonstrate a novel SAW compression technique for single-electron transport that is precise, synchronized and scalable.

CHAPTER 1

Electron flying qubit: state of the art

A quantum computer can solve computational problems exponentially faster than their classical counterparts. Central examples are the Grover's searching algorithm for large databases [Gro96], the Shor algorithm for prime number factorization [Sho94] and, as Richard Feynman proposed in 1982, the direct simulation of quantum physics [Fey82]. Such a speedup is possible by exploiting mainly three fundamental quantum properties: superposition of states, quantum tunneling and quantum entanglement. Due to their typical energy scale, these phenomena are easily perturbed by the surrounding environment such as thermal excitations, external electromagnetic radiations or charge noise. Consequently, the quantum information encoded in the qubit can be easily lost, thus degrading the computational performance.

The implementation of a quantum computer becomes even more challenging when an ensemble of qubits has to interact with each other as well as with neighboring quantum nodes. In this regard, it is not enough to realize a perfect qubit, but also to consider the hardware architecture. Numerous designs have been proposed during the last decade for different qubit platforms, each with its own advantages and limitations [Lad10].

In the following, we skip some promising platforms that are still at their infancy stage [Wan20; GZ21; Mąd22; Xue22; Noi22] to focus on the three most advanced architectures: superconducting qubits, trapped ions and linear optics.

A superconducting circuit, especially the charge-insensitive transmon qubit [Koc07], is at the frontier of the quantum hardware. Its microscopic size offers unique advantages: high reproducibility, easy integration of manipulation and readout components, and efficient modeling with equivalent circuit diagrams. Figure 1.1a shows the state-of-the-art architecture of 53 superconducting qubits realized by Google [Aru19]. The qubits are distributed on the chip surface with tunable couplers between neighboring circuits. This architecture is compatible with error-correction surface codes that avoid information loss during computation. To implement such corrections however, several physical qubits are required to behave as a single *logical* qubit, and thus increasing the hardware overhead.

The another leading platform is based on trapped ions. Figure 1.1b depicts schematically the architecture employed to benchmark 11 qubits from the company IonQ [Wri19]. A linear chain of $^{171}Yb^{+}$ ions is spatially confined near

a micro-fabricated surface electrode trap. Using a global (red) and individual (blue) laser beams, each ion can be uniquely addressed. This addressing technique further allows to achieve fully entangled quantum node, representing the main advantage of this system.

For a scalable quantum computer, the quantum information needs to be transmitted between distant quantum nodes. In the case of superconducting circuits, it has been shown that such quantum state transfer can be mediated via microwave photons [Axl18; Zho19] or acoustic phonons [Bie19]. More impressively, the high-fidelity transmission is also possible via a direct connection with a super-

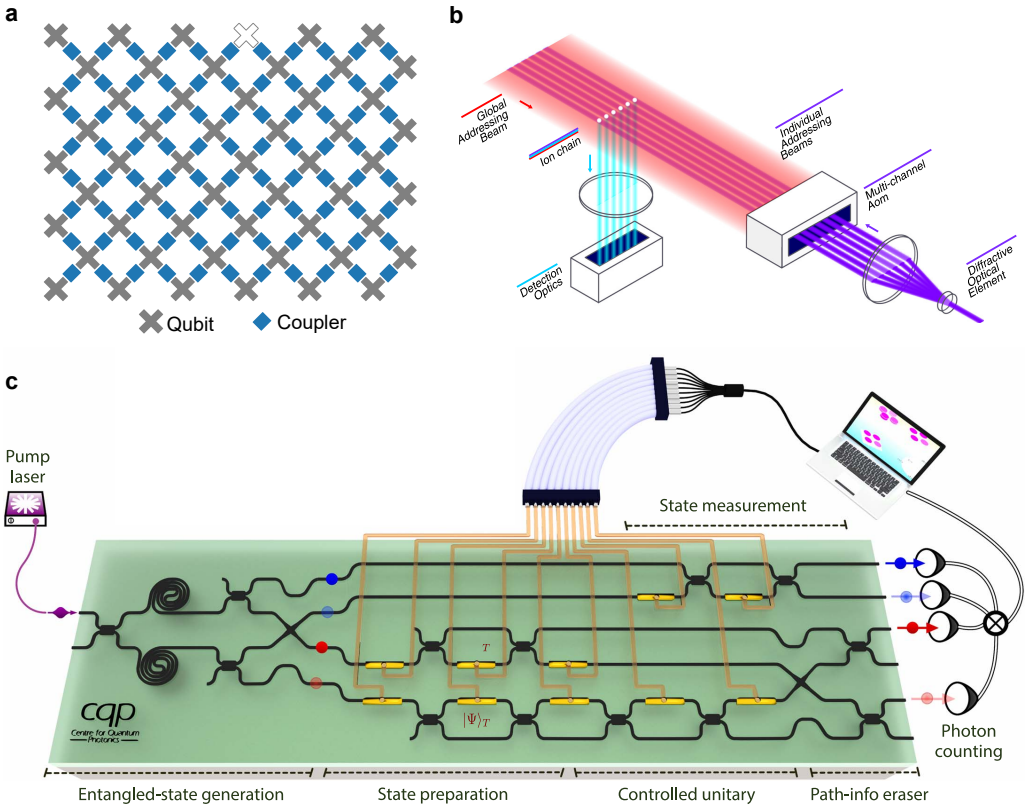

Figure 1.1: Examples of quantum computing architectures. (a) 53-qubits architecture employed by Google. Schematic top view of superconducting qubits (grey) with adaptive couplers (blue). Reprinted from Ref. [Aru19] with permission from Springer Nature. **(b)** 11-qubits hardware used by IonQ. Trapped ions in a linear chain is detected and manipulated via optical components. Reprinted from Ref. [Wri19] with permission from Springer Nature. **(c)** Architecture based on linear optics that is employed by PsiQuantum. Photons propagate across the define paths (black lines) with quantum logic gates and coupling regions. Reprinted from Ref. [San18] with permission from American Association for the Advancement of Science (AAAS).

conducting coaxial cable [Zho21]. Similarly, the quantum state of a trapped ion can be converted into a single photon, and then be transmitted through optical fibers [Mon14]. Owing to these outstanding progresses, superconducting qubits and trapped ions are paving their way into commercial applications.

In contrast to these *stationary* qubits, a system based on a *flying* qubit with single photons is advancing rapidly. Figure 1.1c shows a schematic of the linear-optics architecture for a universal quantum computer envisioned by PsiQuantum [San18; Bar21]. Here, the quantum state is encoded spatially in two transport paths where the quantum logic manipulations are then performed during the flight. In such dual-rail qubit the loss is heralded, meaning that it is easier to implement error correction codes. Moreover, the on-chip single photon can be directly transmitted via an optical fiber avoiding the quantum state degradation due to conversion losses. Having these exemplary advantages in mind, the company is confident to deliver 10^6 qubits[1].

Following a similar architecture, flying qubit based on the electron charge emerged as a promising candidate [Ber00; IAU01]. In contrast to photons that do not interact with each other, electrons can be directly entangled via Coulomb interaction. Furthermore, despite the young field of electron quantum optics, many building blocks such as single-electron sources and detectors are nowadays readily available.

In this chapter, we introduce the basic concept of an electron flying qubit and the quantum logic operations. We then present the state of the art of the essential building blocks. In particular, we focus on the recent progress in electron transport using surface acoustic waves.

1.1 A flying qubit based on charge

Let us start by defining a charge qubit in a double-well confinement potential as depicted in Fig. 1.2a. We denote the quantum states $|0\rangle$ ($|1\rangle$) to the presence of a single electron at the left (right) side relative to the central barrier. In a low-barrier regime, the two lowest eigenstates hybridize into the symmetric $|S\rangle$ and the antisymmetric $|A\rangle$ quantum states

$$|\mathrm{S}\rangle = \frac{1}{\sqrt{2}}\left(|0\rangle + |1\rangle\right) \tag{1}$$

$$|\mathrm{A}\rangle = \frac{1}{\sqrt{2}}\left(|0\rangle - |1\rangle\right) \tag{2}$$

with an energy splitting $\Delta E = E_\mathrm{A} - E_\mathrm{S}$.

[1]For more information, see `https://psiquantum.com`

An alternative way to illustrate a qubit is using a Bloch sphere as shown in Fig. 1.2b where the surface represents all the possible quantum states. It is easy to see that an arbitrary state $|\Psi\rangle$ can be prepared by controlling the angles θ and φ via rotations along the respective y- and z-axis. Using a matrix representation, these rotations correspond to

$$S_y(\theta) = \begin{pmatrix} \cos\frac{\theta}{2} & -\sin\frac{\theta}{2} \\ \sin\frac{\theta}{2} & \cos\frac{\theta}{2} \end{pmatrix} \tag{3}$$

and

$$S_z(\varphi) = \begin{pmatrix} e^{-i\frac{\varphi}{2}} & 0 \\ 0 & e^{i\frac{\varphi}{2}} \end{pmatrix}. \tag{4}$$

Let us now extend this stationary scenario to a propagating electron and describe the building blocks for single-qubit manipulations. We employ two transport paths spatially separated as the basis for an electron flying qubit (see

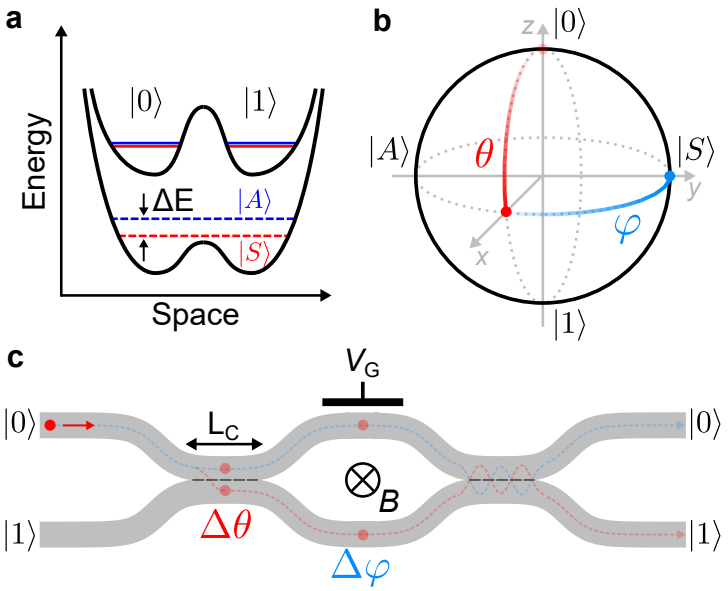

Figure 1.2: Electron flying qubit. **(a)** Schematic of the double-well potential that defines a charge qubit for a high (top) and a low tunnel barrier (bottom). The presence of an electron in the left (right) corresponds to the state $|0\rangle$ ($|1\rangle$). The lowest energy levels are hybridized into the symmetric $|S\rangle$ and the antisymmetric $|A\rangle$ states. **(b)** Qubit representation on a Bloch sphere. The quantum state is defined by the angles θ and φ. **(c)** Flying qubit based on a propagating electron (red circle). Two transport paths define the quantum states $|0\rangle$ and $|1\rangle$. $\Delta\theta$ is achieved via a tunnel-coupled region of length L_C (dashed black line). The Aharonov-Bohm (AB) ring allows to introduce a phase shift $\Delta\varphi$ via the magnetic field B or the electrostatic gate voltage V_G. This particular example is the electronic version of the optical Mach-Zehnder (MZ) interferometer.

schematic in Fig. 1.2c). Let us assume that the electron is initially located in the upper quantum rail, *i.e.* state $|0\rangle$. In order to control θ (y-axis rotation), we bring in close proximity the two rails separated by a tunnel-coupled wire (TCW). A vertical potential cut in this beam-splitter region would be equivalent to the double-well confinement shown in Fig. 1.2a. Adjusting the barrier height between the two paths, the electron would experience coherent oscillations with a period determined by the coupling energy ΔE:

$$\Delta t = \frac{\pi\hbar}{\Delta E}. \tag{5}$$

Consequently, the additional angle $\Delta\theta$ would be determined by the interaction time $t_{\mathrm{C}} = L_{\mathrm{C}}/v$, where L_{C} is the tunnel-coupling length and v is the propagation speed. A superposition of states can then be achieved with a rotation $\Delta\theta = \pi/2$.

To induce a phase shift $\Delta\varphi$ in the flying electron, we exploit the Aharonov-Bohm (AB) effect. The pair of quantum rails can form an enclosed ring with surface area S as shown in Fig. 1.2c. In the presence of a perpendicular magnetic field B, *i.e.* a vector potential $\nabla\times A = B$, the electron would pick up an additional phase

$$\Delta\varphi = \int \vec{k}d\vec{l} - (e/\hbar)B\cdot S \tag{6}$$

owing to the AB effect. Here $\vec{k}$ is the wave vector and $\vec{l}$ is the path along the ring. By sweeping B, $\Delta\varphi$ would undergo oscillations with a periodicity h/eS. A similar phase shift can be realized using an electrostatic gate in one of the arms. An applied voltage V_{G} effectively changes the wave vector $\vec{k}$, and hence it induces a phase shift $\Delta\varphi$.

Having described the single-qubit rotations, let us now focus on the realization of a two-qubit gate. The idea is to use a *control* qubit to induce a phase shift $\Delta\varphi$ on a *target* qubit. Figure 1.3 shows a schematic of such controlled-phase gate for flying electrons. A pair of qubits (A and B) co-propagates in close proximity in a coupling region. Owing to the long-range Coulomb interaction, qubit B would change the wave vector $\vec{k}$ of qubit A, and *vice versa*. In this Coulomb-Coupler (CC) region, each electron would pick up a phase shift

$$\Delta\varphi = 2\cdot\Delta_{\mathrm{C}}\cdot t_{\mathrm{C}}, \tag{7}$$

determined by the capacitive coupling strength Δ_{C} and the interaction time t_{C}. The operation outputs are thus expected to be

$$|00\rangle \to |00\rangle \tag{8}$$
$$|01\rangle \to |01\rangle \tag{9}$$
$$|10\rangle \to \mathrm{e}^{-i\Delta\varphi}\,|10\rangle \tag{10}$$
$$|11\rangle \to |11\rangle\,. \tag{11}$$

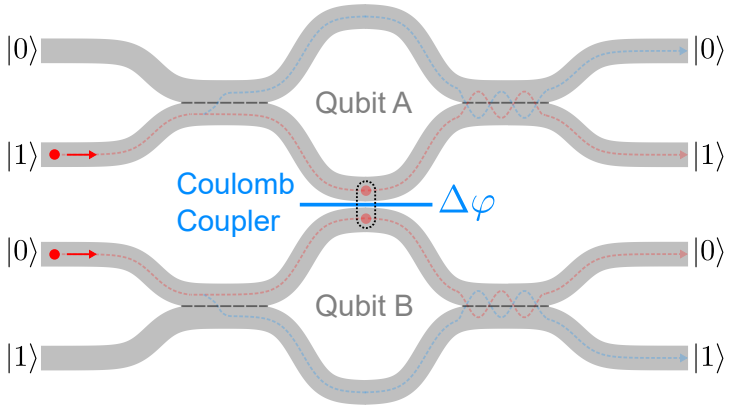

Figure 1.3: Two-qubit quantum gate. Architecture of a controlled phase gate with two flying qubits. The Coulomb-coupling region enables the entanglement of a pair of synchronized electrons. Owing to the long-range Coulomb interaction, an additional phase shift $\Delta\varphi$ is acquired by each flying qubit.

This two-qubit scheme can also be used to achieve in-flight quantum entanglement. For this purpose, we start with qubit A and B in the state $|10\rangle_{\mathrm{AB}}$. With the four beam splitters in a 50:50 position ($\Delta\theta = \pi/2$) and the CC adjusted to induce a phase shift $\Delta\varphi = \pi$, the pair of flying electrons would end up in a maximally entangled Bell state [Bäu18].

Finally, the system can be scaled up by placing quantum rails in parallel as in linear quantum optics [San18]. Combining with the described single- and two-qubit gates, this flying-electron architecture is compatible for the implementation of a universal quantum computer.

1.2 Experimental implementations

Having presented the basic concepts, next we focus on experimental realizations of an electron flying qubit in semiconductor GaAs/AlGaAs heterostructures. To implement such an architecture, it is required the following building blocks:

- highly-efficient single-electron source and detector,
- adiabatic transport,
- coherent beam splitter,
- and controlled phase shifter.

Since one of the essential components is the transport mechanism, let us classify the platforms in three categories: quantum Hall edge channels, non-chiral ballistic transport and surface acoustic waves.

Edge channels in the quantum Hall regime is an excellent testbed for electron-quantum-optics experiments. It has been shown for example electron-electron anti-correlations in a Hanbury-Brown-Twiss setup [Hen99; Ubb14], AB oscillations in a MZ interferometer [Ji03], electron antibunching with a Hou-Ou-Mandel scheme [Ned07; Boc13], and fractional anyonic statistics [Bar20; Nak20].

Efficient single-electron sources in the quantum-Hall regime are also available. In particular, mesoscopic capacitors allow coherent emissions [Fève07] while a single-electron pump generates high-energy wavepackets [Blu07]. To trap these propagating electrons, it has been demonstrated recently that a metallic island can be used as a single-electron detector [Fre20]. Despite these outstanding demonstrations, the quantum-Hall platform is actually not straightforwardly compatible with the flying qubit architecture because the chirality of the edge channels restricts the co-propagation of the electrons.

Let us now switch to ballistic transport in non-chiral systems. The simplest scenario is the flow of electrons in the two-dimensional electron gas (2DEG) across Ohmic contacts in absent of magnetic field. Thanks to the technological advance of GaAs/AlGaAs heterostructures, these electrons can propagate over µm-long distances prior scattering. An effective one-dimensional transport channel can be created on one hand by shaping the 2DEG region via direct etching. Coupling a pair of such electron waveguides for instance led to the observation of wavefunction hybridization [Fis06].

A more flexible method to define a 1D transport channel is to use parallel surface metallic gates. The applied negative voltage controls the density of electrons along the path with high accuracy. This enables to realize non-chiral electron interferometers such as an AB ring for investigations on transmission phase across a quantum dot [Yac95; Sch97; Tak14; Edl17]. For flying qubit applications, a remarkable experiment with a MZ-type interferometer showed that a stream of ballistic electrons can be coherently manipulated [Yam12].

For quantum information processing, it is however necessary to achieve such a ballistic transport at the single-particle level. A promising candidate is the so-called leviton [LLL96]. A leviton is an electrical excitation that propagates very close to the Fermi sea. Due to its characteristic Lorentzian shape, this quasiparticle is a pure quantum excitation that can carry a single electron charge. Pioneering work by Dubois *et al.* [Dub13] showed on-demand generation of levitons and fermionic statistics from collision experiments. Owing to its coherent nature, levitons can be also used as a probing tool via quantum state tomography [Jul14].

The next step for a leviton-based flying qubit is to perform single-shot measurements. Currently, the major limiting factor is the lack of a single-electron detector. There are however interesting proposals that are even compatible with

quantum non-demolition measurements [Gla20].

The last candidate for flying qubit implementations are electron transported by a surface acoustic wave [Ber00; BSR00; For17; Bäu18]. The pioneering experiment by Wixforth *et al.* [WKW86] showed that the potential modulation associated to the SAW can interact with the 2DEG in a GaAs/AlGaAs heterostructure. Later on, Shilton *et al.* [Shi96] reported that SAW can trap and transport these electrons even across a potential barrier. Figure 1.4a shows schematically the top view of a similar setup. Applying a negative voltage on two opposing surface electrodes, an effective 1D channel is formed. The presence of SAW generates moving quantum dots (circles) that can confine electrons. Even if there is a potential barrier along the channel, SAW can bring electrons from one side to the other (see the cross-section view in Fig. 1.4b). Figure 1.4c shows the induced current across the narrow constriction in presence of a continuous SAW [Ast08]. As the input power increases, the pinch-off value shifts towards more negative voltages. This is a signature of electron transport driven by SAW. Furthermore, quantized plateaus appear in the acousto-electric current. At the first plateau for instance, there is an average of one electron per SAW minimum. Such effect has been carefully investigated for example as a potential high precision electron pump [JH00].

The continuously SAW-driven electron transport has been also employed to study quantum phenomena. It has been shown that electrons coupled to a reser-

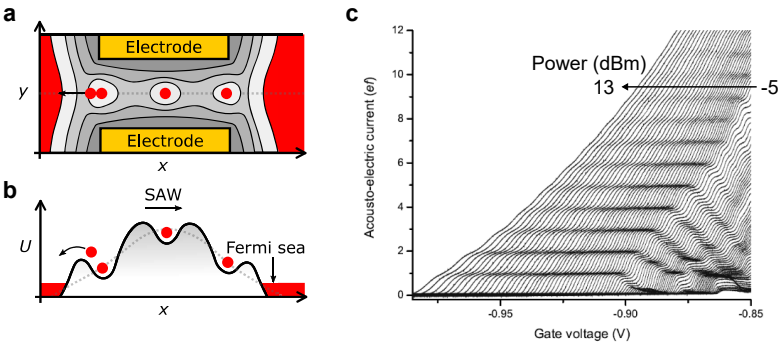

Figure 1.4: Quantized acousto-electric current. (a) Schematic of the potential landscape (grey scale) with SAW modulation. Two surface-electrodes define the quasi-one-dimensional transport channel. The electron density is indicated by the red color with circles as single electrons. **(b)** Potential U along the transport channel with (black) and without (dotted) SAW modulation. Electrons are confined in the moving quantum dots and shuttled from left to right. Reprinted figure with permission from Hermann Edlbauer [Edl19]. **(c)** Experimental acousto-electric current across a narrow constriction for different applied RF power on the transducer. Plateaus at quantized values of ef where e is the elementary charge and f is the resonant frequency. Reprinted figure with permission from Michael Astley [Ast08].

voir manifest picosecond tunnel-oscillations [Kat09]. More interestingly, a quantized acousto-electric current also exhibits coherent oscillations in a setup with coupled transport paths [Ito21]. These observations validate the potential of SAW-driven circuits for flying-qubit implementations.

Let us now focus on the progress of SAW-driven transport at the single-particle level. Using a lateral quantum dot (QD), an initially prepared electron can be loaded into the SAW train, and propagates along a surface-gate defined transport channel. Placing another QD at the end of the rail, the flying electron can be efficiently trapped and detected by a nearby electrometer. Since the first experimental demonstration about a decade ago [Her11; McN11], also the spin degree of freedom was successfully transported [Ber16]. In a recent experiment where a pair of electron spin was sent sequentially, it was shown that SAW can preserve the quantum state, allowing the observation of long-range remote entanglement [Jad21].

The effect of SAW confinement has also been recently studied in our research group in collaboration with AIST (Japan) [Edl21]. Performing single-shot time-of-flight measurements, the electron distribution within the SAW train can be mapped. In particular, a certain SAW amplitude threshold is necessary to ensure that the electron is unambiguously confined during the flight.

To implement the flying-qubit architecture, our group has further investigated a circuit of coupled quantum rails [Tak19]. Even along a 22-µm transport paths, the SAW-assisted transport showed competitive transfer efficiency beyond 99 %. By controlling the potential detuning in the coupled region, on-demand electron partitioning has been also realized. Implementing a delay-controlled sending technique, multiple single-electron sources can be efficiently synchronized. These demonstrated building blocks are essential for the first demonstration of a SAW-driven electron flying qubit.

This state-of-the-art circuit had however a major limitation. Due to the abrupt potential change at the entrance of the coupling region, the transported electron was excited during the flight. The experienced non-adiabatic transition made the quantum state ambiguous, hence hindering the observation of quantum coherence.

1.3 Conclusions

Thanks to rapid advances in the field of electron quantum optics, a single electron is a promising candidate to serve as a flying qubit. Many building blocks have been demonstrated for various transport platforms. In the case of levitons, the realization of a single-electron detector would bring a step closer to the first demonstration of quantum logic implementations. On the other hand, all building blocks for single-shot measurements are already available for SAW-assisted

electron transport. The observation of quantum phenomena is however currently limited by non-adiabatic processes during transport.

In this work, we aim to overcome this limitation by combining two strategies. First, we optimize the surface-gate geometry in order to minimize the abrupt potential changes along the transport paths. We achieve this by developing a quantitative electrostatic model for our nanodevices – see the next chapter. To realize coherent in-flight manipulations on the other hand, we use tailored voltage pulses to control the tunnel-barrier height in real time. By designing the pulse waveform, this approach will allow us, for example, to compensate any remaining potential inhomogeneity, and to turn on or off the coupling on demand.

CHAPTER 2

Quantitative electrostatic modeling

The field of quantum nanoelectronics has advanced significantly during the last decades. Semiconductor devices based on GaAs heterostructure are becoming more complex and thus more difficult to predict their performance. Therefore, a quantitative modeling tool is required to speed up the sample design process as well as to understand the underlying physics. So far however, such simulations rely on a handful of fitting parameters that is often only applicable to a *single* device.

Quantum devices made from GaAs heterostructures can be easily engineered by proper designs of the surface-gate geometry. To ensure the best performance of such devices – that is to find the optimum geometry – it is crucial to know the exact electrostatic potential landscape generated by the metallic electrodes. The traditional optimization workflow for a given heterostructure is based on an iterative process between device fabrication in clean room facilities and low-temperature characterizations. This is *immensely* time consuming and resource demanding. The ideal workflow is schematically represented in Fig. 2.1. Here, the iterative process takes place mainly at the modeling stage, *before* the device fabrication.

The challenge to have a predictive model for semiconductor nanodevices is to consider the different length scales. While the quantum effects are mostly governed by sub-micrometer distances, they are also sensitive to the charge distribution in the microscopic environment. In quantum transport simulations for instance, the electric potential is often approximated, and hence ignoring such multi-scale modeling.

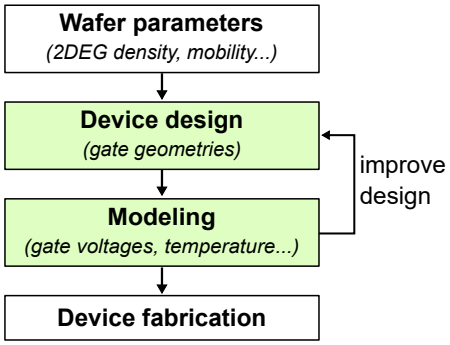

Figure 2.1: Ideal design workflow. Schematic showing typical stages in a sample design process. Examples of parameters to be taken into account are in parenthesis. Highlighted in green are the ideal steps to iterate over for optimal time and resource management.

Furthermore, we need to pay attention to technical challenges. In order to accurately model the heterostructure, it is necessary to take into account the exact growth stack as well as the material properties. Considering the surface-gate geometry, the problem becomes three-dimensional, and hence requiring significant computational cost. Therefore, it is necessary to have an *efficient* multidimensional numerical solver.

In the following, we present a quantitative electrostatic model for nanoelectronic circuits based on GaAs/AlGaAs heterostructures. To account for wafer characteristics, we perform one-dimensional simulations for an initial calibration. In order to benchmark the model, we measure a large set of quantum point contacts (QPCs) with wide-ranging designs. Finally, we extract from the comparison the simulation accuracy.

The results presented in this chapter [Cha22] stemmed from fruitful collaborations with PHELIQS (CEA, Grenoble) and nextnano GmbH (Munich). The nanofabrication, cryogenic characterizations and the preliminary modeling were realized in Néel Institute (CNRS, Grenoble). Stefan Birner, Maria Cecilia da Silva Figueira, Alex Trellaxis, and Thomas Grange (nextnano) provided useful technical support for the numerical solver. The novel calibration method for the simulations and exhaustive benchmarking with experimental data are performed by Eleni Chatzikyriakou and Xavier Waintal (PHELIQS).

2.1 GaAs heterostructure

The starting point for a predictive model is to understand the band diagram of a GaAs heterostructure (see Fig. 2.2). A typical structure consists of a layer of epitaxially grown $Al_xGa_{1-x}As$ on top of a GaAs substrate. At the interface, the bending of the conduction band forms a narrow triangular-like confine-

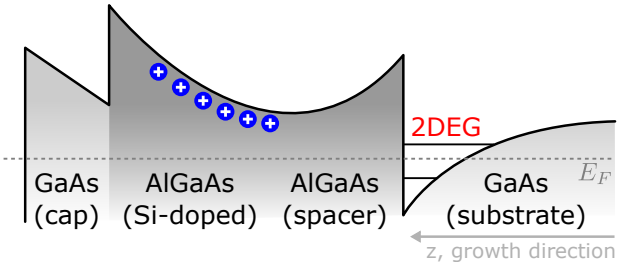

Figure 2.2: Band diagram of a GaAs heterostructure. Schematic of the heterostructure conduction band with indications of the material and the role of each layer. The quantized energy levels that lay below the Fermi level E_F allow the accumulation of electrons at the GaAs/AlGaAs interface. Si-dopants (blue circles) provide the free electrons that form the 2DEG. A GaAs-cap layer at the surface avoids the oxidation of the heterostructure.

ment potential with quantized energy levels. Doping $Al_xGa_{1-x}As$ with Si atoms during growth, free charges accumulate at the interface forming the so-called two-dimensional electron gas (2DEG). While these electrons are confined in the growth direction z, they exhibit high in-plane mobility.

To model quantitatively the heterostructure, one needs to solve the electrostatic and the quantum problem. Moreover, it is necessary to consider the following parameters related to:

- **materials**: dielectric constant, electron effective mass, band gap, crystal orientation, etc;
- **heterostructure growth**: layer thickness and composition, doping profile, etc;
- **2DEG characteristics**: electron density and mobility, and distance to the surface gates;
- **metallic gates**: geometries and typically applied voltages in experiments;
- **other effects**: surface charges, ionization of DX-centers and Fermi-level pinning [SN06].

For this purpose, we employ the commercial software nextnano [Bir07] to profit from its extensive material database and its efficient self-consistent 3D solver.

2.2 The commercial solver: nextnano

The electrostatic environment is modeled via the self-consistent Poisson equation

$$\vec{\nabla} \cdot \left[\varepsilon(\vec{r}) \vec{\nabla} U(\vec{r}) \right] = \rho(\vec{r}) \tag{12}$$

where ε is the material-dependent dielectric constant, U is the electrostatic potential and the total charge density ρ can be expressed as

$$\rho(\vec{r}) = e \left[p(\vec{r}) - n(\vec{r}) + N_{\mathrm{d}}^{+}(\vec{r}) - N_{\mathrm{SC}}^{-}(\vec{r}) \right]. \tag{13}$$

Here, e is the elementary charge, p and n correspond respectively to the free holes and electrons, N_{d}^{+} is the ionized dopant concentration and N_{SC}^{-} is the surface charge density.

The nextnano solver uses the classical Thomas-Fermi approximation to calculate the free carriers p and n. In regions where quantum effects are taken into account, the charge densities are obtained via the multiband $\vec{k} \cdot \vec{p}$ envelope function method. Details can be found in Ref. [Bir07; And09] and in Appendix B. Figure 2.3 shows the execution process of the nextnano solver. The software initializes the device geometry from input parameters. Its extensive database

provides the corresponding material properties. The solver starts with an initial guess of the band structure to evaluate the non-linear Poisson equation with classical approximations. The simulated electrostatic potential is then used in the Schrödinger equation to obtain the eigenvectors, eigenvalues and quantum charge densities. Using a self-consistent approach, the solver iterates to minimize the error until convergence. The results are finally post-processed and saved.

Since the electrostatic potential is strongly dependent on the gate geometry, we need to import the exact design used for nanofabrication. For this purpose, I have developed a Python script that translates a standard CAD format (GDSII file) into nextnano input geometries. Such automatic conversion avoids human error and enables fast iterations in the sample design.

From a general perspective, the design process requires to investigate input parameters that optimize a given figure of merit. The main advantage of using the nextnano software is to avoid the technical details of numerical simulations. In this context, the user can focus on the physics rather than developing its own solver. We found however that the software does not allow automatic feedback loops with custom-made post-processing methods. To overcome this limitation, I developed `nextnanopy`: a user-friendly Python module to interface the nextnano

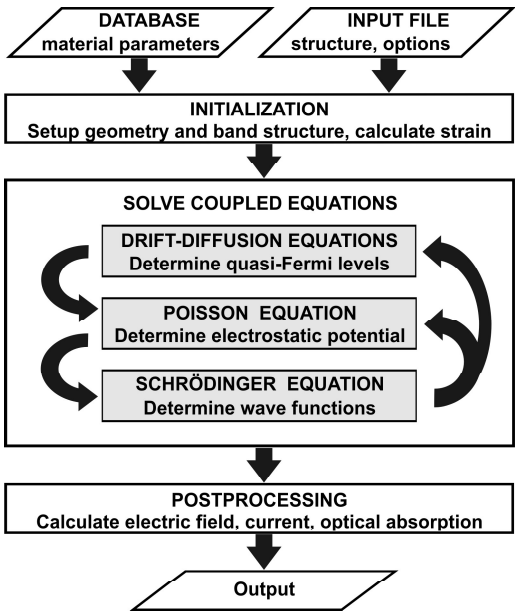

Figure 2.3: Flow scheme of nextnano. Schematic of the execution protocol based on an initialization, a self-consistent iteration and a final post-processing. The arrow indicates the direction of the flow. Reprinted figure with permission from Till Andlauer [And09].

software[1].This public repository is currently maintained by the company with positive feedback from customers around the world.

2.3 Modeling of the investigated devices

After the growth of a GaAs heterostructure, the 2DEG density and the mobility is typically characterized via Hall measurements at 4K. There are however two main unknowns: the concentration of ionized dopants and the surface charge density. For preliminary modeling, we calibrate these values with 1D simulations along the growth direction z based on two steps [Hou18]. First, we set the surface boundary condition as a Schottky barrier with no applied voltage. We use the experimentally reported barrier height $\phi = 0.75$ eV in our simulations [CS65]. Note that, in the case of GaAs, this value is almost independent on the metal workfunction [CS65; SN06]. We then assume fully ionized donors and adjust the concentration in the AlGaAs layer until we match the measured 2DEG bulk density. Next, we remove the Schottky boundary condition to mimic a free surface. Adjusting the surface charges, we recover the reported 2DEG density. Note that this calibration method assumes that the electron density is uniform everywhere.

Let us now apply this model to the investigated devices. Our samples are fabricated on a Si-modulation-doped GaAs/$Al_{0.34}Ga_{0.66}As$ heterostructure grown by molecular beam epitaxy (MBE). This high-quality wafer (#14104) was provided by our collaborators Prof. A. D. Wieck and A. Ludwig from the Ruhr-University Bochum in Germany. The high-mobility 2DEG lies at the GaAs/AlGaAs interface, located 110 nm below the surface. Performing Hall measurements at 4.2 K under dark conditions, we find a bulk 2DEG density of $n_{\text{bulk}} \approx 2.79 \times 10^{15}$ m^{-2} and a mobility of $\mu \approx 9.1 \times 10^5$ cm^2 V^{-1} s^{-1}. The surface electrodes for the nanostructures are made out of a metal stack of 4 nm Ti and 13 nm Au, deposited by successive thin-film evaporation.

Figure 2.4a shows the simulated band diagram of the studied heterostructure using the nextnano software. Surface charges (orange) and the doping density (blue) are obtained from the above-mentioned calibration method. We observe an electron density distribution at the GaAs/AlGaAs interface as expected. The zoom-in of this region (see Fig. 2.4b) shows triangular-like potential wells with quantized energy levels. In particular, we find that two levels are below the Fermi energy $E_{\text{F}} = E = 0$ contributing to the 2DEG density.

Let us now investigate the influence of the surface-gate voltage. Figure 2.5 shows the evolution of the potential U at the 2DEG (black) and the corresponding electron density n_{2DEG} (red) as a function of the applied voltage V_{G}. For a

[1]For more information, see `https://github.com/nextnanopy/nextnanopy`

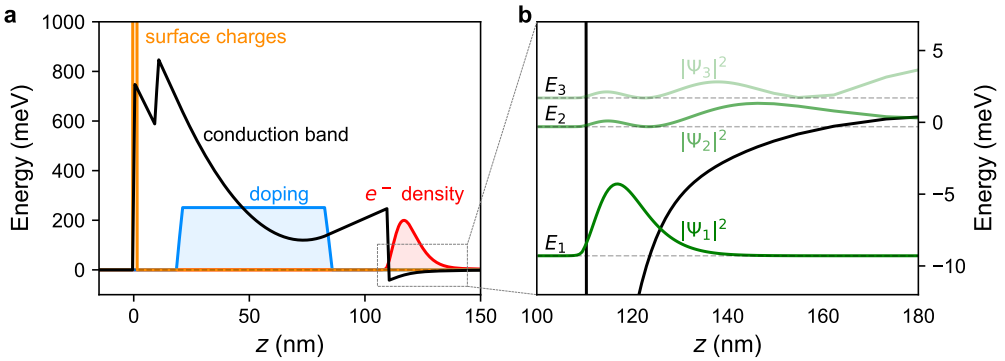

Figure 2.4: Band diagram simulation. **(a)** One-dimensional simulation of the conduction band of the investigated GaAs heterostructure along the growth direction z. The energy at the surface is fixed at $\phi = 0.75$ eV. Negative surface charges (orange; 13.3×10^{11} cm^{-2}) and positive doping (blue; 16.2×10^{11} cm^{-2}) are input parameters extracted after applying the described calibration protocol. The 2DEG electron density (red; 2.7×10^{11} cm^{-2}) appears at the GaAs/AlGaAs interface. **(b)** Zoom in on the interface region. Three quantized energy levels of the triangular confinement potential are shown with the respective probability density $|\Psi_i|^2$ (green; arb. units) where $i = 1, 2, 3$. The Fermi level E_F is at $E = 0$ as reference.

certain negative voltage, the 2DEG underneath the gate is completely depleted ($n_\mathrm{2DEG} = 0$). We find that this 2D pinch-off voltage ≈ -0.49 V is in good agreement with the experimentally measured value[2] $\approx -0.46 \pm 0.01$ V.

We observe moreover a distinct variation in the course of U around the 2D pinch-off region. The slope of the linear data represents the voltage-energy conversion factor. Before and after 2DEG depletion, we find that such gate-alpha factors are $\alpha_\mathrm{s} = 0.03$ eV/V and $\alpha_\mathrm{d} = 1$ eV/V. This result indicates that the surface-gate voltage is screened significantly by the presence of electrons in the 2DEG.

In experiments, we have extracted the gate-alpha factor α_s for the non-depleted situation. Using Coulomb-diamond measurements (see Section 4.4), we found $\alpha_\mathrm{exp} = 0.05 \pm 0.01$ eV/V that is similar to the simulated value. This good agreement indicates that the nextnano software properly takes into account the screening effect without any fitting parameter.

Next we present a realistic simulation example for the lateral quantum dot (QD) employed in our time-of-flight experiments [Edl21]. Figure 2.6a shows the potential landscape U at the 2DEG position with indications of the surface-gate

[2]This value is the average from dozens of devices on the same wafer [Cha22]. An example of the experimental pinch-off curve is shown in Fig. 2.9a where V_1 is equivalent to the 2D pinch-off voltage.

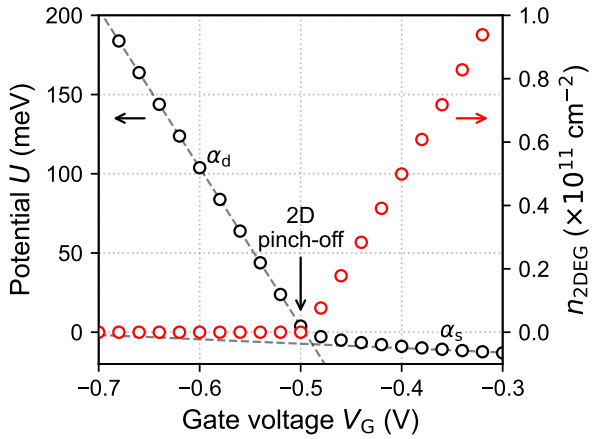

Figure 2.5: Gate-alpha factor. Simulated potential U at the 2DEG (black; left y-axis) and the electron density n_{2DEG} (red; right y-axis) as a function of the applied voltage V_G on the surface gate. The condition at which all electrons are depleted ($n_{2DEG} = 0$) is denoted as 2D pinch-off. Linear fits of U (dashed lines) result in gate-alpha factors $\alpha_d = 1$ eV/V and $\alpha_s = 0.03$ eV/V. The reference energy is set at the Fermi level $E_F = 0$.

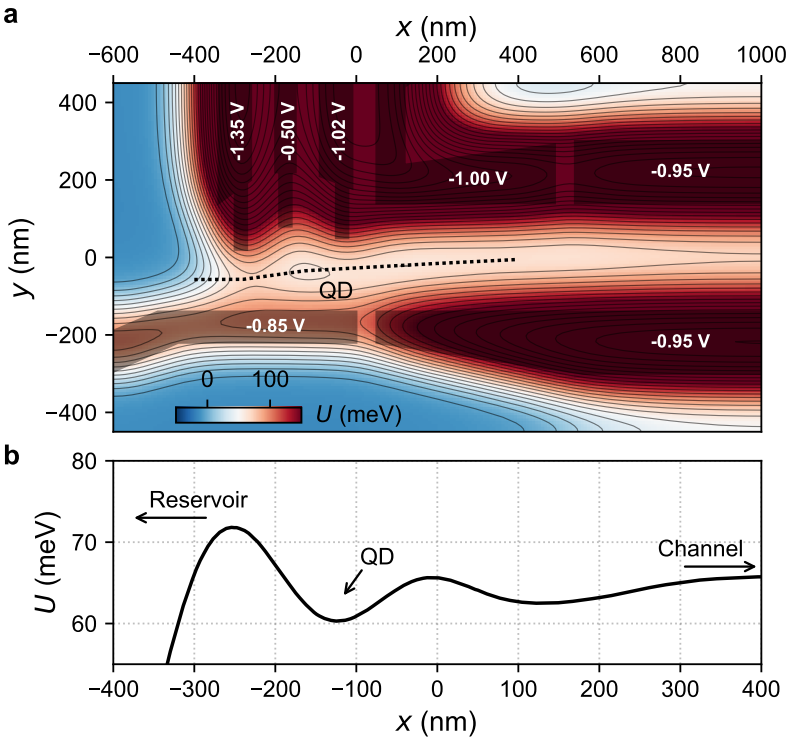

Figure 2.6: Potential landscape of a lateral quantum dot. (a) Potential U from three-dimensional simulations with realistic gate geometries (grey polygons) and voltages. The equipotential lines (solid) show a circular confinement region near $x = -130$ nm and $y = -35$ nm that corresponds to the QD. **(b)** Potential cut across the QD (dotted line in (a)) with indications of the reservoir and the channel.

geometry (grey polygons). The employed voltages correspond to the experimentally applied values for isolating a single electron in the QD. Following the equipotential lines (solid), the data shows a circular confinement region (near $x = -130$ nm, $y = -35$ nm) which represents the QD. The potential cut across the QD is depicted in Fig. 2.6b. The high barrier at the left side avoids the electron to tunnel out from the parabolic confinement well to the reservoir. In contrast, the smooth potential variation to the channel allows an adiabatic SAW-assisted transport.

The presented model reproduces many features of the investigated samples. For this reason, we employ this method to simulate the devices presented along this thesis. However, a quantitative benchmarking is so far still missing. In the following, we present our strategy to develop a predictive model for nanoelectronic devices.

2.4 Towards a predictive modeling of nanoelectronic devices

A quantum point contact (QPC) is a well-studied device that consists of a pair of surface gates facing each other. Applying a negative gate voltage, a narrow constriction is formed that exhibits quantized conductance plateaus at cryogenic temperatures [KDP80; Wee88]. In such devices, the transport properties are determined by the gate geometry. For this reason, a QPC is an excellent testbed to benchmark our simulations.

A predictive modeling tool must be applicable to large amount of samples without the need of custom fitting. Our strategy thus is to measure an extensive set of 110 QPCs with 48 unique designs. Owing to the wide-ranging gate geometry, we are able to calibrate the model and to quantify its predictive power.

To study the geometrical influence of QPCs, we investigate three kinds of shapes: Rectangular (A), Round (B) and Smooth (C) (see Fig. 2.7). Rectangular (A) design corresponds to a wire of length L defined by two parallel gates separated by a width W. Round (B) consists on two semi-circular gates with radius

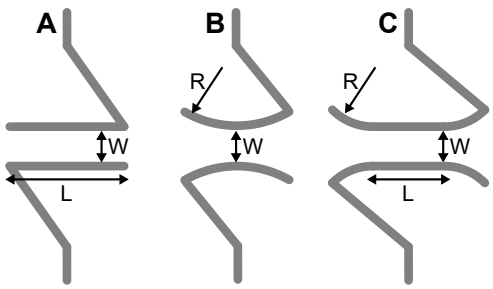

Figure 2.7: Quantum point contact designs. Schematic of QPC shapes: Rectangular (A), Round (B) and Smooth (C). Characteristic geometrical parameters L (length), W (width) and R (radius) are indicated by arrows.

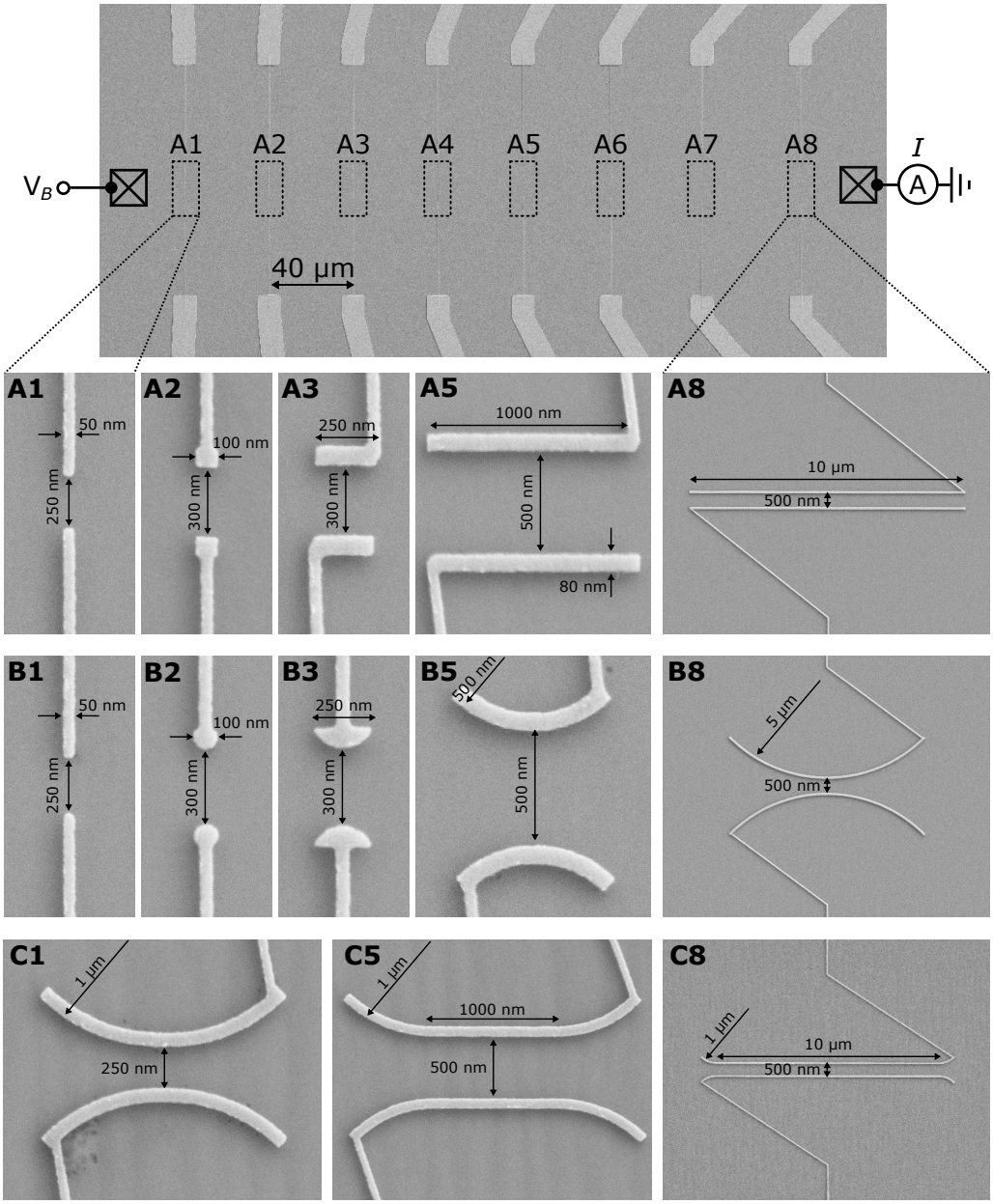

Figure 2.8: SEM images of QPCs. (Top) Overview of the experimental setup with a set of 8 QPCs in series sharing a pair of Ohmic contacts. (Bottom) Examples of investigated shapes (A, B, C) with indications of the geometrical parameters.

R that defines the point contact. At last, Smooth (C) belongs to an intermediate design between A and B, combining the linear constriction with adiabatic entrances. For each design (A,B,C), 16 different combinations of geometrical parameters L, R and W are investigated, from the smallest (A1, B1, C1) to the largest (A16, B16, C16) sizes – see examples of fabricated devices in Fig. 2.8.

To account for statistical variability, devices with the exact same design are repeated across the chip. We label them with an additional Latin letter. For example, A2a and A2b are different QPCs with identical nominal characteristics.

In order to maximize the number of measured devices in a same cooldown, a set of 8 QPCs is placed in series sharing a common pair of Ohmic contacts (see top panel in Fig. 2.8). With a separation more than 40 µm, we ensure that no crosstalk occurs between the neighboring QPCs. In total, we fabricated and measured a total of 110 QPCs with 48 unique designs that are distributed in 16 sets on a chip of 10 mm × 8 mm.

The conductance characterization was performed at two temperatures T ≈ 4.2 K and ≈ 30 mK. We first apply a bias voltage V_B on the Ohmic contact to induce a current I. To characterize the transport properties, we measure the current I as a function of surface-gate voltage V_G for each device. The full data set of these transport measurements can be found in Ref. [Cha22].

Figure 2.9a shows the characteristic $I-V_\mathrm{G}$ trace for the Rectangular A1 QPC at ≈ 30 mK. We observe three distinct current drops at V_1, V_2 and V_3. Voltage V_1 corresponds to the depletion of the electrons underneath the macroscopic contacts that are far away from the constriction. This is equivalent to the 2D pinch-off discussed previously. As the voltage becomes more negative, the thinnest part of the gate (≈ 50 nm) is also depleted, resulting into the second drop V_2. Below this gate voltage, the transport properties are fully dominated by the narrow constriction formed between the gates. The current shows quantized plateaus until the pinch-off value V_3.

To evaluate the conductance at the constriction, G_QPC, we subtract the resistance due to the Ohmic contacts and the experimental setup. Those can be obtained through the current I_0 measured at $V_g = 0$ V. Accordingly, we find that

$$G_\mathrm{QPC} = \frac{I}{V_B(1 - I/I_0)} \tag{14}$$

Figure 2.9b shows the course of G_QPC with plateaus at quantized values of the conductance quantum $G_0 = 2e^2/h$. The regular steps indicate a well-defined QPC.

This characteristic $I-V_\mathrm{G}$ curve contains several features for benchmarking the model. For a first quantitative comparison, we focus only on the voltage drops V_1, V_2 and V_3. We anticipate however to combine our electrostatic simulations

with the open-source software Kwant [Gro14] to reproduce the full conductance trace in the near future.

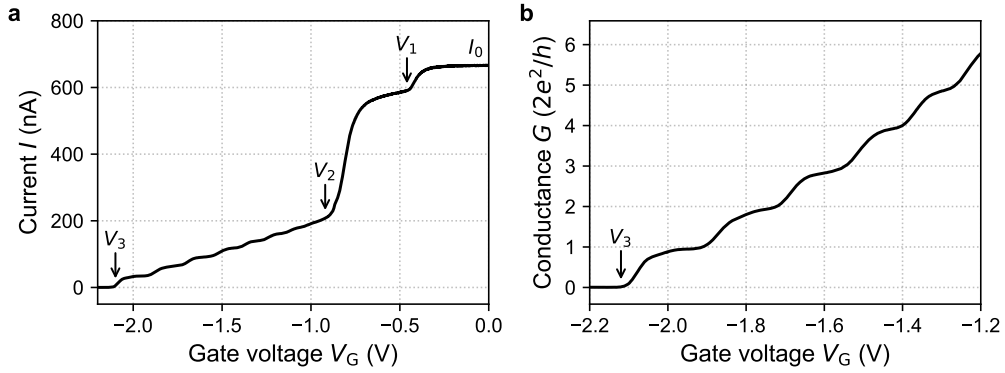

Figure 2.9: QPC pinch-off curve. (a) Measurement of the current I through the Rectangular A1 QPC ($L = 50$ nm, $W = 250$ nm, $R = 0$ nm) as a function of the applied surface-gate voltage V_G. The Ohmic contacts are biased with a voltage $V_\mathrm{B} = 500$ µV. I_0 is the measured current with unpolarized gates ($V_\mathrm{G} = 0$). Distinct current-drops (arrows) are denoted as V_1 (2D pinch-off), V_2 (narrow-gate pinch) and V_3 (QPC pinch-off). This dataset is measured at ≈ 30 mK. **(b)** Zoom in on the pinch-off region. Conductance G extracted using equation 14 with a system resistance $R_0 \approx 900\ \Omega$.

2.5 Calibration protocol

Having explained the experimental approach, next we introduce our updated model. Let us first clarify the employed notations. Figure 2.10 shows schematically the top view of a QPC device. We consider 4 simulation regions:

1. **ungated**: free surface without a Schottky gate;
2. **gated**: region on the large section of the metallic gate. Here we consider both the gate width W_G and length L_G to be infinite;
3. **narrow-gate**: in this region, we consider $W_\mathrm{G} \approx 50$ nm and an infinite L_G.
4. **QPC**: the actual split-gate design that forms the constriction.

Similar to the previous calibration protocol (see Section 2.3), we use 1D simulations of the gated and ungated regions to adjust the doping concentration and the surface charges (see Fig. 2.11). Here however, we allow the 2DEG electron density underneath the metallic gate n_G and the free surface n_S to be different. The protocol starts with the gated region. We find the dopant concentration in the AlGaAs layer that reproduces the experimental 2D pinch-off voltage V_1. Owing to the macroscopic gate size ($W_\mathrm{G} \gg 1$ µm), we find that $V_1 \approx -0.46$ V

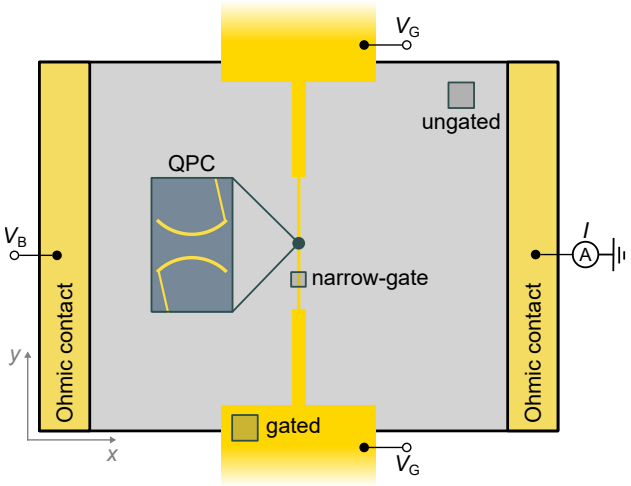

Figure 2.10: Modeling schematic. Simplified top view of a device with indications of the Ohmic contacts (source and drain) and the Schottky gates (yellow). The 4 simulation regions are defined as ungated, gated, narrow-gate and QPC.

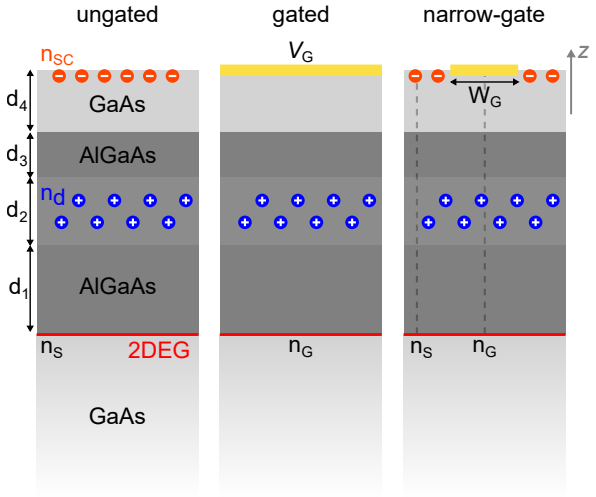

Figure 2.11: Model calibration protocol. Side view along the growth direction z showing the heterostructure stack with layer widths d_i for $i = 1, 2, 3, 4$. AlGaAs is doped with positive charges with density n_d while the GaAs-cap layer has a density of surface charges n_SC. The ungated (gated) scenario corresponds to 1D model without (with) a Schottky gate at the surface. For the narrow-gate region, a 2D-model is used with a metallic gate of width W_G. The 2DEG electron density below the free surface (Schottky gate) is denoted as n_S (n_G). For the investigated heterostructure, the parameters are $d_1 = 25$ nm, $d_2 = 65$ nm, $d_3 = 10$ nm, $d_4 = 10$ nm and $W_\mathrm{G} = 50$ nm.

fluctuates less than 2 % across the 110 devices. Therefore, the calibrated dopant concentration can be applied to a large set of samples. Next, we adjust the surface charges in the ungated region to satisfy $n_S = n_{2DEG}$. Using this method, we find that the presence of an unpolarized surface gate reduces the 2DEG electron density by ≈ 10 %.

2.6 Validation with a large experimental dataset

Having calibrated the model, we simulate the pinch-off voltage V_3 for each QPC design using 3D simulations with the exact gate geometry. As an example, Figure 2.12a shows the simulated n_{2DEG} for the Round QPC B6 with $V_G = -1.80$ V. The narrow constriction is formed in the middle of the gap. The density profile

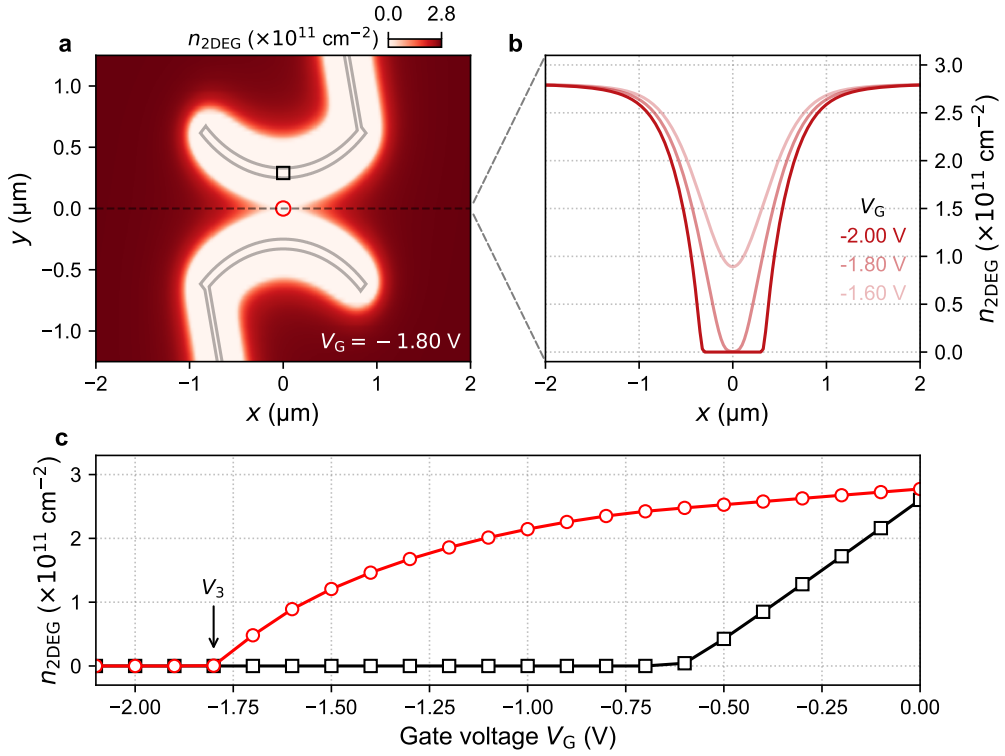

Figure 2.12: Pinch-off simulation. (a) Distribution of the electron density n_{2DEG} for QPC B6 ($L = 0$ nm, $W = 500$ nm, $R = 1250$ nm) at voltage $V_G = -1.80$ V with indication on the gate geometry (grey polygons). **(b)** n_{2DEG} along the constriction ($y = 0$; dashed line in (a)) for three values of V_G. **(c)** Electron density at two different locations indicated in (a): below the surface gate (black square) and at the middle of the constriction (red circle). The QPC pinch-off occurs at V_3.

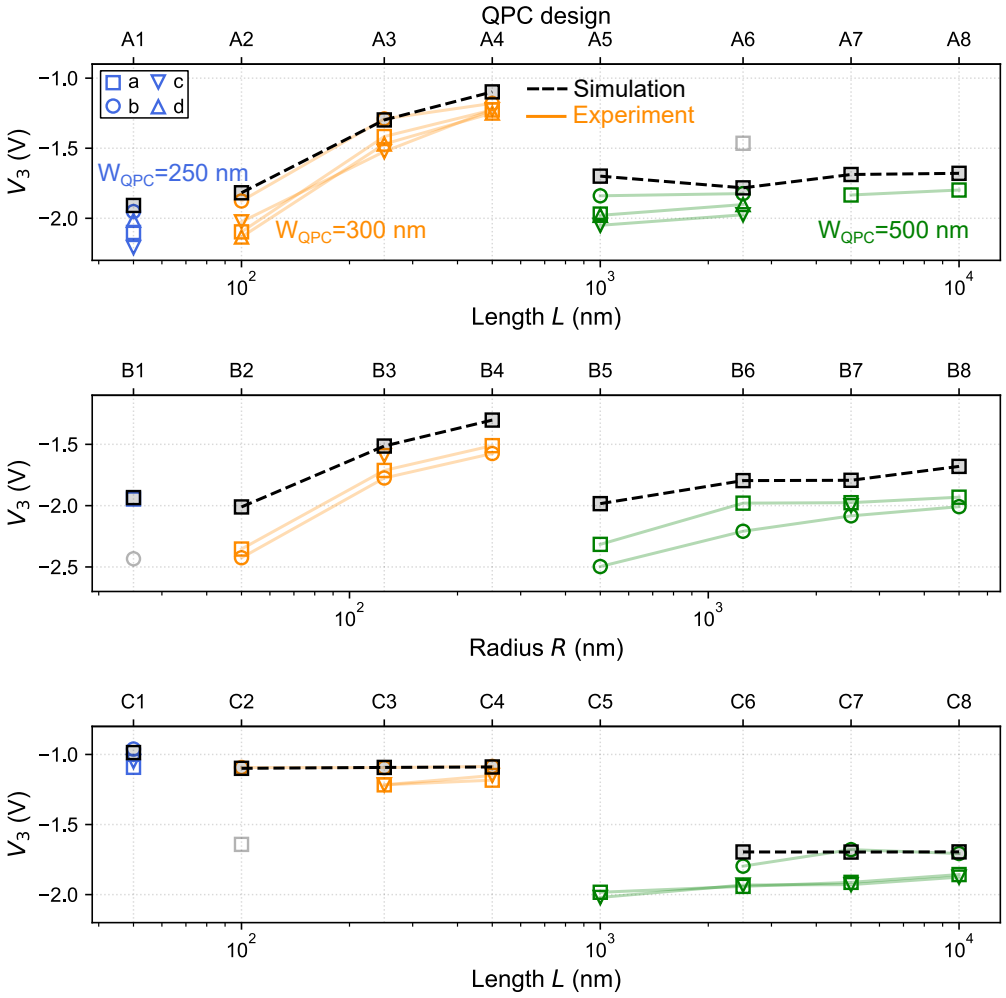

Figure 2.13: Model benchmarking. Comparison of pinch-off voltage V_3 between simulation (dashed black lines) and experiment (solid lines). The results are grouped according to the QPC design: A (top), B (middle) and C (bottom). Colors correspond to the QPC width $W = 250$ nm (blue), $W = 300$ nm (orange) and $W = 500$ nm (green). Sets of QPCs with the same design are indicated with different symbols and Latin letters. Grey symbols show faulty devices that still exhibit quantized features in their pinch-off traces. Missing data points such as C2c correspond to QPCs damaged during fabrication.

at $y = 0$ for various V_G is shown in Fig. 2.12b. For more negative applied voltage, the electron density decreases until the QPC is pinched. To extract the pinch-off voltage, we evaluate n_{2DEG} as a function of V_G at the center ($x = 0$, $y = 0$) as shown in Fig. 2.12c. V_3 is then simply the voltage at which $n_{2DEG} = 0$.

Let us now evaluate the predictive power of our model using the pinch-off voltage V_3 as a reference. Figure 2.13 shows a comparison of V_3 between simulations (black) and experimental data (colors) for different QPC designs (A, B and C). Several devices with same geometries are also measured (Latin letter) to account for statistical variations. The simulations show a systematic agreement with a deviation < 10 %.

With our extensive dataset, we further investigate the origin of the deviation between simulations and experiments. We see that, in a given QPC set such as A2a/A3a/A4a (orange squares), the difference in V_3 is constant for all devices. However, in a different set with same design like A2b/A3b/A4b (orange circles), V_3 has similar course, but with no offset. This indicates that the 2DEG is not uniform across the wafer.

To account for the disorder in the system, a particular model based on the idea of percolation has been developed [Cha22]. By dividing the system into discrete cells with different electron densities, the model evaluates the deviation between the pinch-off values V_1, V_2 and V_3. Although we do not present here the details of the analysis, this approach predicts a deviation of 6 % that is similar to the observed variation. These results indicate that our electrostatic simulations are in excellent agreement with the experimental data.

2.7 Conclusion

In conclusion, we have developed a predictive electrostatic model for nanoelectronic devices on GaAs heterostructures. Using QPCs as testbed, we fabricated and measured a total of 110 devices with 48 unique designs. Applying a calibration protocol, we found numerically the effective doping concentration and surface charge density. Employing the pinch-off value as reference, our simulations showed an excellent accuracy above 90 %. The presented model paves the way for quantitative electrostatic simulations in semiconductor nanocircuits.

Having introduced the modeling approach for our single-electron devices, the focus of the next chapter is on another essential component: surface acoustic waves.

CHAPTER 3

Surface acoustic wave optimization

Surface acoustic waves (SAW) are present in a myriad of technologies such as bandpass filters, radars and pressure sensors [Mor07]. Owing to the recent progress in nanofabrication techniques, SAW devices are finding more and more applications in quantum technologies [Del19]. These acoustic phonons can for example modulate a photonic nanocavity [Fuh11] or drive electron cycloid motions [Son21]. The associated SAW piezoelectric field can interact with charge carriers in 2D materials such as graphene [HMLS18] or semiconductor MoS_2 flakes [Rez16]. In an undoped GaAs heterostructure, SAW can drive the recombination of carriers from a 2D electron-gas and 2D hole-gas for single-photon emission [Hsi20].

For quantum-information-processing applications, these acoustic phonons are able to encode a quantum state that can be coherently manipulated on demand [Sat18]. Interacting with superconducting qubits for instance, SAW can transmit quantum information and mediate remote entanglement [Bie19; Bie20]. SAW can also be used as a link between quantum nodes in a quantum computer, either transferring the charge [Her11; McN11; Tak19] or the spin [Ber16; Jad21] degree of freedom.

Here we use a surface acoustic wave to transport single electrons across a circuit of coupled quantum rails. Since a strong SAW confinement potential is necessary for unambiguous electron transport [Edl21], we aim to maximize the SAW amplitude.

In this chapter, we first present the basic concepts for SAW generation and describe the employed characterization and modeling methods. In particular, we measure the frequency response to check the quality of the fabricated devices. In order to characterize the SAW profile from single-shot emissions, we perform time-resolved measurements with a SAW detector. Finally, we discuss the optimization strategy adopted for maximizing the transduction efficiency.

3.1 Basic concepts

A surface acoustic wave is a mechanical wave which travels across the free surface of an elastic solid at the speed of sound characteristic of the material. The mathematical description was first reported by Lord Rayleigh in 1885 [Ray85],

thus it is also known as Rayleigh wave. Since then, this model has been widely applied to study macroscopic phenomena such as earthquakes.

SAWs can also be present in microscopic devices caused by the collective motion of surface atoms (see schematic in Fig. 3.1). The elliptical orbit normal to the surface described by each atom generates a microscopic deformation. For a counterclockwise motion for instance, this acoustic wave propagates from left to right. Furthermore, the wave amplitude decays exponentially towards the interior of the substrate with the characteristic penetration depth of one SAW wavelength λ. For this reason, this is called a *surface* acoustic wave.

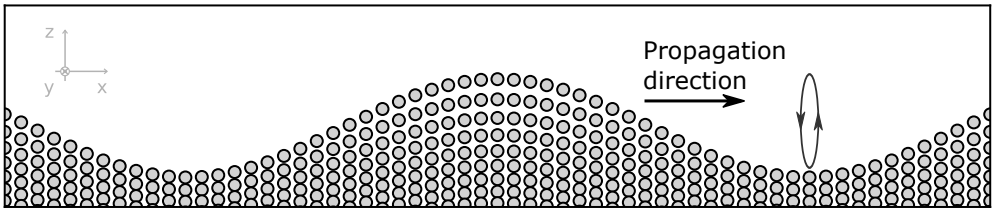

Figure 3.1: Schematic of a surface acoustic wave. Artistic representation of the deformation produced by a surface acoustic wave. The atoms collectively move in a vertical elliptic orbit, giving rise to a traveling wave with a propagation direction indicated by the arrow. The amplitude of the wave decays away from the surface ($-z$ direction).

The invention of the Interdigital Transducer (IDT) by White and Volmer in 1965 [WV65] enabled on-demand SAW generation with electrical signals. Since then, commercial applications with SAW technology experienced an exponential increase. In particular, the IDT opened up the gateway to a new and most versatile approach to the design of analog electrical filters operating at selected frequencies, including the gigahertz (GHz) range [Mor07].

An IDT consists of two sets of metallic electrodes arranged in a comb structure as depicted in Fig. 3.2. The device is deposited on a piezoelectric substrate to allow the conversion of an electrical signal to a mechanical deformation. On-demand SAW emission is thus achieved by applying an input voltage to the surface electrodes.

The electrode design of the IDT determines the characteristics of the emitted SAW [Mor07]. The simplest transducer is composed by a periodic and uniform repetition of electrode pairs. Figure 3.2a shows schematically such a regular IDT with a finger overlap A and a cell periodicity λ. Driving the transducer with an oscillating signal, each finger pair would emit elementary SAWs. When the input signal is at the resonant frequency $f = v_{\mathrm{SAW}}/\lambda$, where v_{SAW} is the SAW velocity, the elementary SAWs would superpose constructively, leading to a plane wave with wavelength λ. Note that owing to the symmetric electrode design, SAWs are actually emitted at both ends of the IDT.

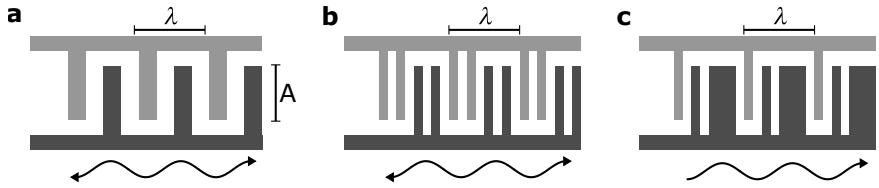

Figure 3.2: Examples of interdigital transducers. Schematic representation of the surface electrodes of interdigital transducers (IDTs) with an aperture A and a cell periodicity λ. A regular IDT is shown in **(a)** with a single-finger and **(b)** a double-finger design. Here, surface acoustic waves (SAWs) are emitted in both directions (arrows) in contrast to **(c)** a unidirectional (DART) IDT.

To maximize the transduction efficiency with the electrode design, it is important to consider internal reflections in the IDT. Each electrode acts not only as a SAW emitter, but also as a reflecting mirror. The design with two electrodes per period (single-finger IDT) exhibits intrinsically a cavity effect where SAW is trapped in the transducer for a certain time before leaving the structure. This has a detrimental effect on the transduction efficiency. One solution is to split each finger into two to prevent the formation of standing waves inside the transducer. Figure 3.2b shows the design of such a double-finger IDT with an electrode separation of $\lambda/4$. The drawback of this design is a more challenging fabrication for a given frequency, but it allows for more efficient SAW emission.

Another method to enhance the transduction efficiency is to profit from the reflections at the electrodes. A regular IDT is a bidirectional transducer because SAWs are emitted at both sides of the device, resulting in an inherent loss of 3 dB. Employing asymmetric unit cells as in Distributed Acoustic Reflection Transducers (DART) IDT [Dum19] (see Fig. 3.2c), the scattering of waves propagating in one direction is strongly enhanced. The constructive interference with non-reflected waves then leads to unidirectional SAW emission.

3.2 Characterization setup

Having introduced the basic concepts of SAW generation, let us now present our characterization methods for an IDT. We are interested specifically in two aspects: the frequency response of an IDT and the SAW profile from single-shot emissions. For this purpose, we employ an experimental setup that is schematically shown in Fig. 3.3a which allows us to investigate both the transmission spectrum as well as the time-resolved SAW profile *in situ*.

The frequency response of the IDT can be simply accessed via transmission measurements with a vector network analyzer (VNA) between two identical IDTs. On the other hand, to characterize the shape of the acoustic wave, we fabri-

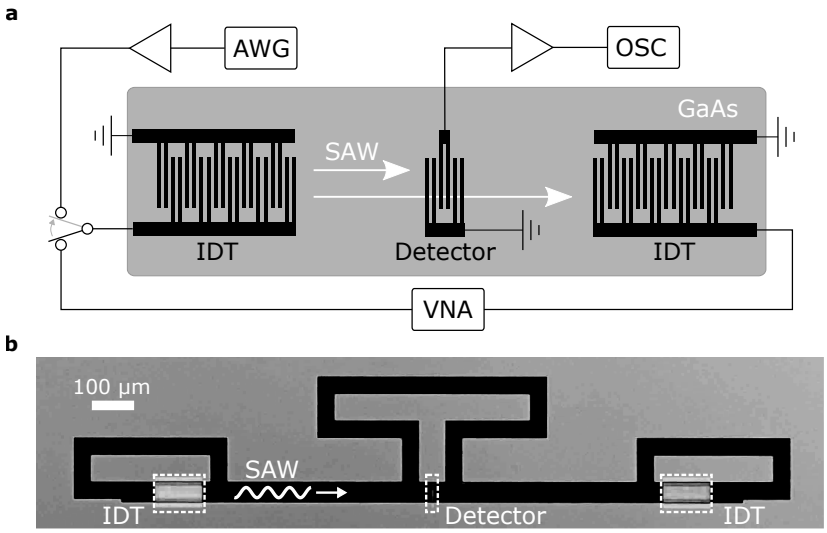

Figure 3.3: Characterization setup for SAW generation. **(a)** Schematic of the setup to measure the frequency response (long arrow) and the time-resolved SAW profile (short arrow). **(b)** Optical microscopy image of the experimental setup. The transducers are deposited on top of GaAs (black) with Au contacts (grey).

cate in addition a narrow double-finger broadband detector (for details, see Appendix E.1). We first apply a tailored input signal on the investigated IDT with an arbitrary waveform generator (AWG) to trigger the SAW formation. As the SAW train passes the detector IDT, it introduces an electrical signal through piezoelectric coupling that is projected on a fast sampling oscilloscope (OSC). In order to enhance the signal-to-noise ratio, both input and output signals are amplified with a broadband amplifier (SHF S126A).

Figure 3.3b shows an optical microscopy image of this setup. The investigated IDTs are deposited on GaAs substrate with gold (Au) metallic contacts. The IDT and the SAW detector is typically separated by ≈ 550 µm which is equivalent to a SAW traveling time of ≈ 195 ns. This delay is chosen to prevent the overlap between the SAW signal and the electromagnetic crosstalk.

3.3 Regular IDT for single-electron transport

Let us now use the described setup for the characterization of a regular IDT that is employed for most of the electron-shuttling experiments carried out in this thesis.

The transducer consists of aluminium (Al) surface electrodes fabricated using standard electron-beam lithography. A precise nanofabrication recipe is provided in Appendix A.1. They are deposited on either GaAs substrate or GaAs/AlGaAs

heterostructure with the SAW propagation direction along $[1\bar{1}0]$.

Figure 3.4 shows an scanning electron microscopy (SEM) image of the regular IDT. This transducer has a double-finger design with cell periodicity $\lambda = 1$ µm, aperture 30 µm and metal-gap ratio around 50:50. It is composed by $N = 111$ unit cells which is equivalent to a SAW traveling time $t_{\mathrm{IDT}} \approx 40$ ns. The homogeneity of the metallic electrodes over more than 100 µm reflects the well-controlled nanofabrication process.

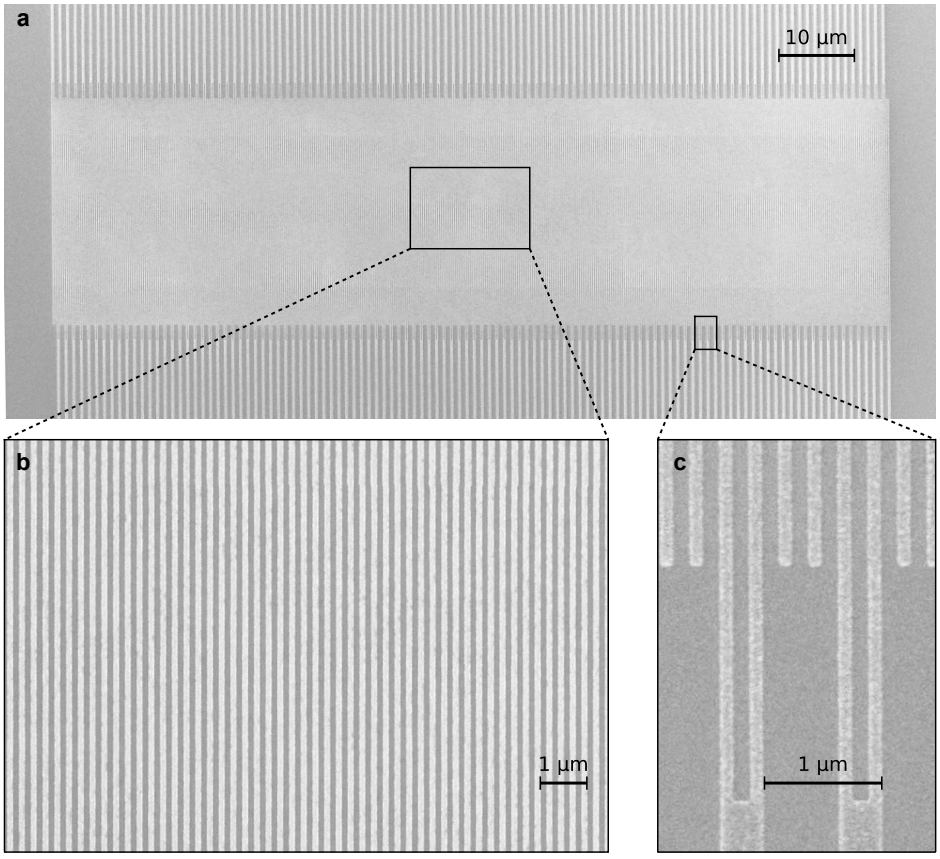

Figure 3.4: SEM image of a regular IDT. **(a)** Overview of the whole double-finger IDT with a cell periodicity 1 µm, an aperture 30 µm and a total of $N = 111$ unit cells. **(b)** Zoom into the center of the transducer showing the homogeneity of the metallic electrodes. The ratio between the gap and the electrode width is around 50:50. **(c)** Close-up SEM image at the boundary of the overlapping region. Pairs of electrodes which share the same polarity define the double-finger design.

3.3.1 Frequency response

We first characterize the frequency response of the IDT at ambient temperature. The transmission S_{21} between two identical regular IDTs is shown in Fig. 3.5a. We observe a single resonance frequency $f_0 \approx 2.83$ GHz. Taking into account the wavelength $\lambda = 1$ µm, we deduce a SAW velocity $v_{\mathrm{SAW}} \approx 2.83$ µm/ns which is in good agreement with reported values [PSK19].

Let us now investigate why the transmission data has a non-uniform background. For this purpose, we perform a Fourier transform on the frequency spectrum to obtain the equivalent data in the time domain (see Fig. 3.5b). The

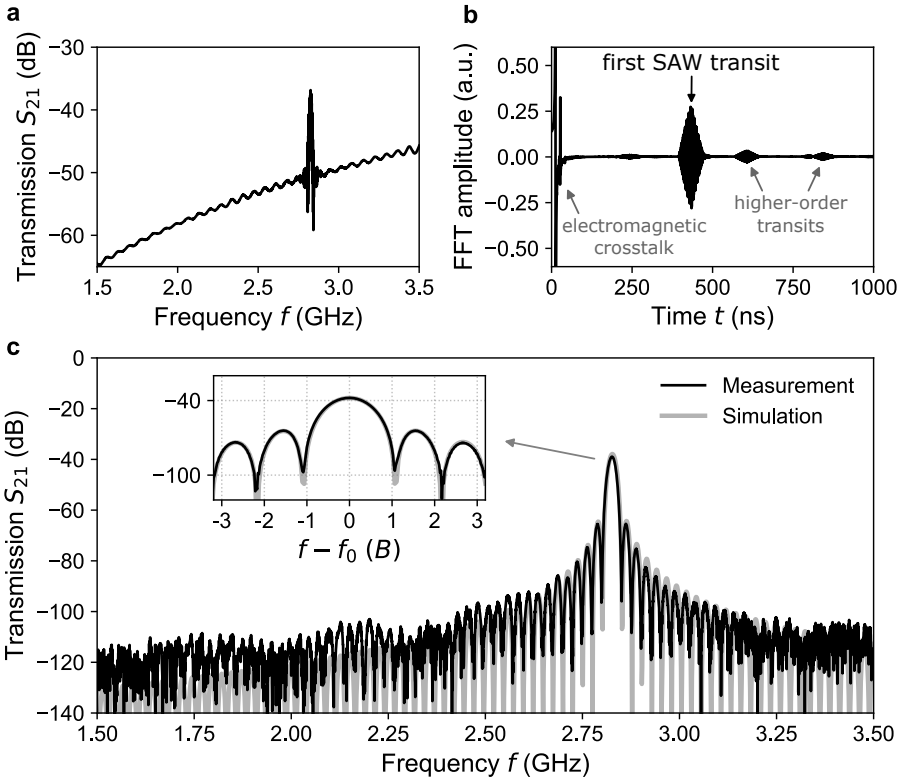

Figure 3.5: Frequency response characterization. **(a)** Raw transmission spectrum between identical regular IDTs separated by ≈ 1100 µm. **(b)** Time-domain signal obtained by applying Fourier transform (FFT) to the data presented in (a) with indications of the first SAW transit ($t \approx 390$ ns) and second-order effects. **(c)** Filtered frequency spectrum after removing the signals outside the range between 350 to 500 ns in the data shown in (b). The grey line shows the expected signal from the numerical simulation from delta-function model (see Section 3.3.2). The inset shows a zoom on the resonance with its characteristic side interference fringes. The data indicates a resonance frequency $f_0 \approx 2.83$ GHz and a bandwidth $B \approx 23.5$ MHz.

transformed data shows discrete signals at various timings. First, there is an instantaneous increase at $t \approx 0$ ns. Since electromagnetic (EM) waves travel $\approx 10^5$ times faster than the sound wave, we attribute this signal to the EM crosstalk from the direct airborne capacitive coupling between the IDTs. The first transit of the SAW appears at the expected arrival time $t \approx 390$ ns. We then deduce that the subsequent weaker signals correspond to higher-order SAW transits from reflections between IDTs.

In order to isolate the IDT response, we filter out these second-order effects by removing all signals outside the first-transit time-window (between $t \approx 350$ ns to 500 ns) and transforming it back to the frequency domain (see Fig. 3.5c). The filtered transmission shows a flat background and clear resonant fringes. Zoom into the resonance peak (inset), the lobes are separated by the expected characteristic bandwidth $B = f_0/N \approx 23.5$ MHz [Mor07]. We note that B is equivalent to the full width at half maximum of the main peak.

To further verify that the IDT is working as designed, we need to model the expected frequency spectrum. The simplest model to describe the performance of a bidirectional IDT is the so-called delta-function model [TH71]. It can predict the frequency response given the spatial position of the electrodes. The major limitation is however the lack of information about the absolute insertion loss. Despite this drawback, the delta-function model can be an excellent starting point for modeling the frequency response of an IDT in preliminary designs. In the next section, we describe in detail this model and apply it for the regular-IDT design.

3.3.2 Delta-function model

The simplest way of modeling the IDT response is to approximate the output as a superposition of elementary waves that are emitted with delay times t_n at discrete point sources located at the finger positions x_n. In this picture, the response function for a certain IDT geometry can be written in the time domain as a sum of Dirac delta functions located at each finger location:

$$h(t) = \sum_{n=0}^{N} P_n \cdot \delta(t - t_n) \tag{15}$$

where $P_n \in \pm 1$ is the polarity of the n^{th} finger that indicates connection to the input electrode or to ground. In general, the SAW response $y(t)$ can be mathematically expressed as a convolution of an input signal $V(t)$ with the IDT geometry $h(t)$ acting as a filter:

$$y(t) = (V * h)(t) \tag{16}$$

The IDT response in the frequency domain can then be calculated by the Fourier transform of $y(t)$ via application of the convolution theorem as:

$$\hat{y}(\omega) = \hat{V}(\omega) \cdot \hat{h}(\omega) \tag{17}$$

where $\hat{V}$ and $\hat{h}$ indicate respectively the Fourier transform of V and h. Considering a continuous input signal, $V(t) \propto e^{i\,\omega_0 \cdot t}$, we obtain:

$$\hat{V}(\omega) = \int_{-\infty}^{\infty} e^{i\,(\omega_0 - \omega)\cdot t}\,\mathrm{d}t \propto \delta(\omega_0 - \omega) \tag{18}$$

What brings us to:

$$\hat{y}(\omega) \propto \hat{h}(\omega) \tag{19}$$

To obtain the frequency response of a certain IDT geometry within the delta-function model, we thus can directly evaluate the Fourier transform of equation 15:

$$\hat{y}(\omega) \propto \sum_{n=0}^{N} P_n \int_{-\infty}^{\infty} \delta(t - t_n) \cdot e^{i\,\omega \cdot t}\,\mathrm{d}t = \sum_{n=0}^{N} P_n \cdot e^{i\,\omega \cdot t_n} \tag{20}$$

where $t_n = x_n / v_{\mathrm{SAW}}$ is determined by the SAW velocity v_{SAW} and the IDT's finger positions x_n.

We remind that this model does not take into account absolute insertion losses. Therefore, it is only capable for reproducing the shape of the frequency response. There are alternative approaches that can better quantify the transduction efficiency such as the Crossed-Field model [Smi69a; Smi69b]. This approach takes into account contributions such as the conversion ratio between electrical and acoustic power, the capacitance of electrode finger pairs, the circuit impedance and the matching network. Although it can quantitatively predict the frequency spectrum, it is often complex to evaluate all these parameters experimentally.

The internal reflections inside the transducer are also ignored in the delta-function model. This effect is essential to simulate transducers such as unidirectional DART IDT [Eks17; Dum19] or multi-harmonic Split52 IDT [Sch15b]. In a more complex model known as Reflective Array Method (RAM) [Mor07], the reflections are included as a set of transmission and reflection coefficients arranged in a scattering matrix. Even though this method allows precise response analysis of the majority of IDTs, its implementation is often non-trivial.

Let us now apply the delta-function model to simulate the frequency response of the characterized regular IDT. To consider the double-finger design, we set finger positions at $x_n = n \cdot \lambda/4 = n \cdot 250$ nm where $n = 0, 1, ..., 4N$ and $N = 111$. Using $v_{\mathrm{SAW}} = 2.83$ µm/ns and the amplitude at the resonance frequency as a fitting parameter, we simulate the frequency response (see semi-transparent

line in Fig. 3.5c and inset). The expected course from the delta-function model reproduces the main peak as well as off resonances of the experimental data. This excellent agreement validates the high quality of the fabricated IDT.

3.3.3 Time-resolved measurements

Having verified the frequency response of the regular IDT, in the following we investigate the SAW profile from single-shot emissions. For this purpose, we perform time-resolved measurements employing a detector transducer with same periodicity than the regular IDT ($\lambda = 1$ µm). Having only 6 electrodes ($N = 1.5$), the IDT has the maximum detection bandwidth $B \approx 1.9$ GHz around its resonance frequency (see Appendix E.1).

We first excite the IDT with a resonant oscillating signal at f_0 with a duration $t_{\mathrm{Sig.}}$. When the SAW train arrives at the detector, it induces an electric signal due to piezoelectric coupling that is measured by a fast oscilloscope. Figure 3.6a shows the time-resolved voltage trace after applying an input signal for a duration $t_{\mathrm{Sig.}} = 40$ ns. The data shows an initial signal ($t \approx 0$) with a length matching $t_{\mathrm{Sig.}}$. Due to its instantaneous arrival, we attribute this to the electromagnetic crosstalk. A second signal appears later at the delay around $t_{\mathrm{Det.}}$. The zoom-in profile shows a sinusoidal pattern with period $T_{\mathrm{SAW}} \approx 350$ ps (see Fig. 3.6b).

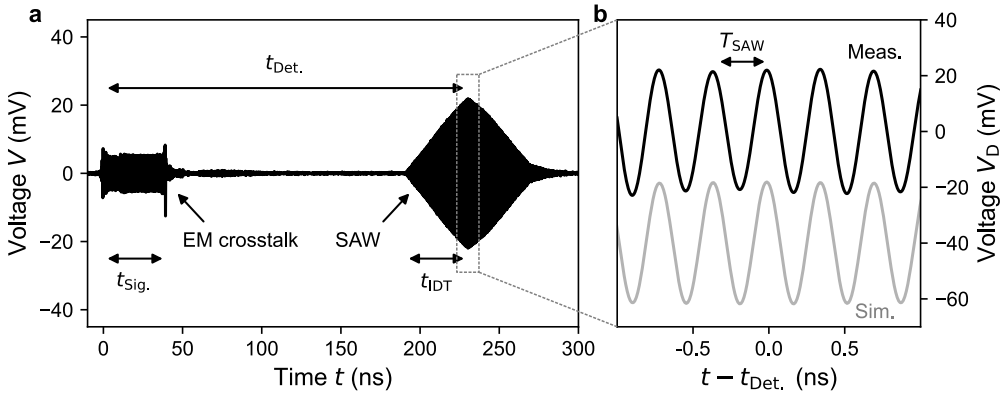

Figure 3.6: Time-resolved measurement. **(a)** Trace of the detector response for a resonant input signal of a duration $t_{\mathrm{Sig.}} = 40$ ns applied on the regular IDT. As for the transmission spectrum, the data is post-processed with a Fourier filter in the range of 0.4 to 3.5 GHz in order to suppress parasitic contributions from internal higher harmonics of the AWG, the amplifier responses and standing waves in the radio-frequency lines. The SAW arrives with expected delay $t_{\mathrm{Det.}}$ after initial electromagnetic crosstalk ($t \approx 0$). **(b)** Zoom into the region around $t_{\mathrm{Det.}}$ showing the SAW profile with a period $T_{\mathrm{SAW}} \approx 350$ ps. The grey line shows the course expected from the impulse-response model (see Section 3.3.4).

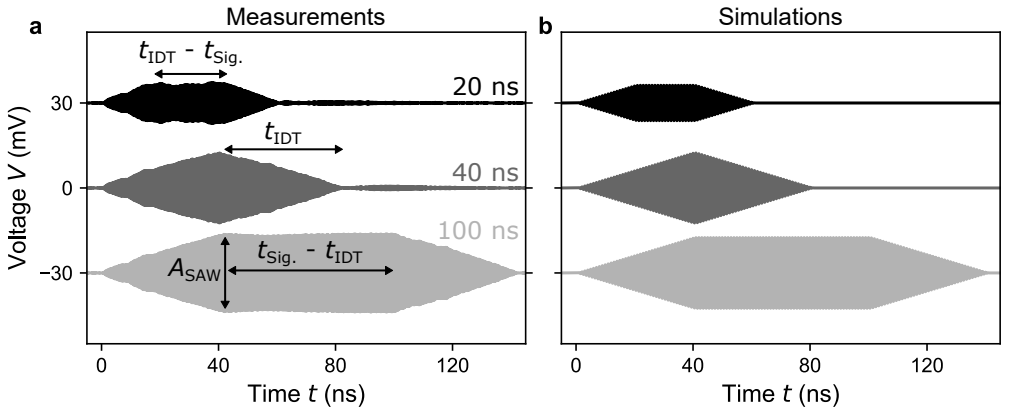

Figure 3.7: Input signal duration. **(a)** Time-resolved SAW profile by applying a resonant input signal of duration $t_{\text{Sig.}} \in \{20, 40, 100\}$ ns on the regular IDT. The experimental traces are shifted vertically by 30 mV. **(b)** Expected profiles from the impulse-response model (see Section 3.3.4).

This feature confirms that the signal corresponds to the SAW profile.

Let us now comment on the envelope of the SAW profile. We observe a diamond shape with a rising and falling duration matching $t_{\text{IDT}} \approx 40$ ns. These features are related to the traveling time t_{IDT} for the leftmost elementary wave to superpose with the rightmost one. For this reason, in order to achieve the maximum SAW amplitude A_{SAW}, it is necessary to apply an input signal for a duration $t_{\text{Sig.}} \geq t_{\text{IDT}}$.

In order to verify this idea, we investigate the effect of the input signal duration $t_{\text{Sig.}}$ wtih time-resolved measurements. Figure 3.7a shows the measured SAW profile for various $t_{\text{Sig.}}$. For a long pulse duration ($t_{\text{Sig.}} = 100$ ns $> t_{\text{IDT}}$), we observe that the amplitude saturates at A_{SAW} extending over a length $t_{\text{Sig.}} - t_{\text{IDT}} \approx 60$ ns. We highlight that, for the single-electron shuttling experiments, we typically load the electron in the middle of such plateau where the SAW confinement potential is the strongest.

Similar to the frequency characterizations, we aim to contrast the time-resolved SAW profile with simulations. A minimal tool for modeling the SAW profile is the impulse-response model developed by Hartmann, Bell and Rosenfeld [HBR73]. Given an IDT design, it can predict the shape of the emitted SAW for an *arbitrary* input signal. Similar to the delta-function model, it assumes non-reflective electrodes and ignores insertion losses. It is however a powerful tool at the early design stages of SAW engineering. In the next section, we describe the details of this model and compare the simulated SAW profiles with time-resolved experimental data.

3.3.4 Impulse-response model

A more accurate description of the IDT geometry can be achieved by the so-called impulse-response model [HBR73]. This model is particularly important when describing the time response of irregular transducer geometries such as the chirp IDT discussed in Chapter 7. In contrast to the delta-function model, the time response of an IDT, $h(t)$, is defined by a continuous frequency-modulated function:

$$h(t) \propto \sin\left(2\pi \int_0^t f(\tau) d\tau\right) \tag{21}$$

To construct $h(t)$ via the instantaneous frequency response $f(t)$, one-half cycle of a sine wave is placed between two electrodes with the opposite polarity (half period). This construction rule is schematically shown in Fig. 3.8 via the examples of a regular and a chirp IDT. For a regular design, each period is the same giving a constant frequency response $f(t) = f_0$. In the case of a non-uniform IDT geometry, $f(t)$ changes depending on the finger positions.

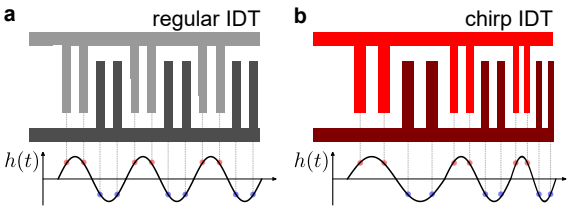

Figure 3.8: Construction of the impulse response of IDTs. Examples of the response function $h(t)$ (vertical axis) in comparison to the finger positions for **(a)** a regular IDT and **(b)** a chirp IDT.

In order to calculate the surface displacement by a SAW, $y(t)$, resulting from a certain input signal $V(t)$, one can now simply calculate the convolution with the IDT response $h(t)$ – compare equation 16.

The impulse-response model further allows to predict the output from multiple consecutive transductions. In time-resolved measurements in particular (see Section 3.3.3), the broadband IDT converts the surface displacement back into an electrical signal. The experimental data thus contains also information of the detector IDT response, $h_{\mathrm{Det.}}(t)$. To compare the time-resolved data to a simulation from the impulse-response model, it is necessary to convolve $y(t)$ also with the detection filter $h_{\mathrm{Det.}}(t)$:

$$V_{\mathrm{Det.}}(t) \propto (y * h_{\mathrm{Det.}})(t) = (V * h * h_{\mathrm{Det.}})(t) \tag{22}$$

Let us now apply this model to reproduce the experimental SAW profiles. We consider the regular IDT response $h(t) \propto \sin(2\pi f_0 t)$ with $f_0 = 2.83$ GHz. Similarly, the broadband detector response $h_{\mathrm{Det.}}(t)$ is a sinusoidal waveform with 1.5 periods. Since the impulse-response model does not take into account the insertion losses, we use the saturation amplitude A_{SAW} as a fitting parameter.

Figure 3.6b shows the simulated SAW profile with a resonant input signal with duration $t_{\mathrm{Sig.}} = 40$ ns. We observe a good agreement with the experimental data.

Next, we check if the model can also predict the influence of the input signal on the SAW profile. Figure 3.7b shows SAW envelopes simulated with a resonant input signal with a duration $t_{\mathrm{Sig.}}$. We observe that this model reproduces the characteristic diamond shape, including the rising, falling and plateau regions. We highlight that using only A_{SAW} as a fitting parameter, it also predicts the relative amplitude for the case of a short pulse $t_{\mathrm{Sig.}} = 20$ ns. Owing to the excellent agreement, we will use this model in Chapter 7 to design the non-uniform chirp IDT for SAW engineering.

3.4 Optimization of transduction efficiency

In this section, we briefly review the design evolution of the regular IDT used for single-electron transport and describe our strategy to improve the SAW emission efficiency.

The transducer employed in the pioneering experiment by Hermelin *et al.* [Her11] was a single-finger, regular IDT made of Au. Despite their remarkable achievement, the transfer probability of 92 % had still room for improvements. Only recently, we have demonstrated a transfer efficiency beyond 99 % [Tak19], owing primarily to the increase in SAW amplitude by upgrading to a double-finger IDT with more unit cells. This realization places the SAW-assisted technique as a promising platform for electron-quantum-optics experiments and quantum computing applications.

We observed however signatures that the electron was still not unambiguously trapped during transport, even for the strongest achievable SAW confinement at that time. To overcome this limitation, numerical simulations suggested that a larger SAW amplitude of at least three times would avoid electron tunneling to neighboring minima [Tak19]. Therefore, we need to further optimize the transduction efficiency.

One approach is to use a different substrate under the IDT which has a larger piezoelectric constant such as $LiNbO_3$ or ZnO. This is however not trivial to implement since it requires to develop a novel nanofabrication process.

An easier alternative is to change the metal stack of the electrodes. The weight of the metallic fingers for instance introduces a damping effect known as mass loading [Mor07]. For this purpose, we replace the previously-employed Au electrodes with a lighter material such as Al. Figure 3.9a shows the frequency response from transmission measurements for three IDTs: double-finger Au (orange), double-finger Al (black) and single-finger Al (blue). We observe that, by changing Au to Al, there is a significant increase of 16.4 dB at the resonant peak.

This improvement brings us a step closer to the desired strong SAW confinement regime.

Let us now compare this response with the single-finger design. The data shows a reduction of 2.6 dB at the resonance peak compared to the double-finger IDT. To further understand this effect, we convert the spectrum to the time domain via the Fourier transform (see Fig. 3.9b). We observe that the single-finger transducer has an extended transit signal in contrast to the discrete ones from the double-finger design. This is actually a signature of the delayed SAW emission caused by internal reflections. These results confirm that splitting the electrodes is beneficial for the SAW generation process.

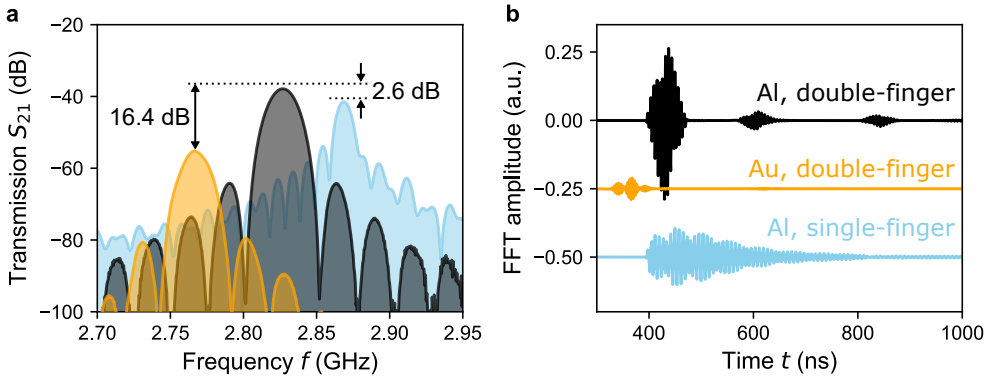

Figure 3.9: Efficiency of SAW generation. **(a)** Transmission spectra from double-finger Al (black), double-finger Au (yellow) and single-finger Al (blue) IDTs with indications of the differences between resonance amplitudes. **(b)** Time-domain trace from applying the Fourier transform of the frequency data. Double-finger Al IDT shows discrete transit signals, in contrast to the broaden SAW emission from the single-finger design.

3.5 Conclusion

In this chapter, we have described the foundations of surface acoustic waves and its generation with interdigital transducers. Using a regular IDT as a reference, we showed our characterization setup for investigating the IDT frequency response and the SAW profile from time-resolved measurements. To contrast the respective experimental data, we employed the delta-function model and the impulse-response model. The excellent agreement confirmed that the fabricated IDT had the expected designed performance. Finally, we improved the transduction efficiency with respect to the previous generation by using a lighter electrode metal: Al.

Having introduced the modeling of semiconductor nanodevices and the characterization methods for IDTs, we focus in the next chapter on the design and

the calibration process of a novel single-electron circuit with optimized transport paths.

CHAPTER 4

Single-electron circuit of coupled quantum rails

A surface acoustic wave can transport a single electron between distant quantum dots. The proof-of-concept experiments carried out by Hermelin *et al.* [Her11] and McNeil *et al.* [McN11] opened up a novel approach to perform electron-quantum-optics experiments at the single-particle level. Since then, not only the charge degree of freedom has been studied, but also the spin information of the elementary particle [Ber16]. For instance, Jadot *et al.* [Jad21] has recently demonstrated that SAW can transport coherently the singlet-triplet state encoded in a pair of electrons. These results represent a promising application of SAW-driven transport as a link between quantum nodes in a quantum computer.

By exploiting the charge degree of freedom, it has been proposed [BSR00; Bäu18] that electrons trapped by SAW can be used as flying qubits for quantum logic implementations. Recently, Takada *et al.* [Tak19] has employed a circuit of coupled transport paths to demonstrate on-demand partitioning of a single electron during its flight. This remarkable milestone paves the way for the realization of the flying-electron-qubit architecture. The next step for such a quantum circuit is to couple a pair of synchronously transported electrons. The experimental realization of this central building block is still however missing.

In this chapter, we show the progress towards the demonstration of such a coupling scheme. We first present an optimized sample design of the single-electron circuit after gaining insights from experimental iterations. To achieve highly efficient SAW-assisted transport, we show our protocol to prepare and to shuttle single electrons along the coupled quantum rails. Implementing a delay-controlled sending technique, we demonstrate our ability to synchronize two independent electron sources. Finally, we verify the on-demand partitioning of the elementary charge to prepare for experiments with a pair of flying electrons.

4.1 Sample design

The state of the art of SAW-assisted transport is a single-electron circuit with coupled quantum rails [Tak19] as shown in the SEM image in Fig. 4.1a. This design is the electronic equivalence to the optical beam splitter. Conveying two transport paths into a narrow coupling region, the distribution of the flying electron can be tuned on demand. By analyzing the partitioning data, we find that the electron

is excited into higher orbital states during the flight, and thus detrimental for quantum logic implementations. Using numerical simulations, we attribute this excitation to the abrupt change in the potential landscape near the entrance to the tunnel-coupled wire (TCW).

One strategy to avoid such non-adiabatic transitions is to optimize the surface-gate geometry at the injection region near the TCW. In order to find a design criteria, we estimate the ratio between a change in energy ΔE over a timescale Δt. The typical charging energy of a lateral quantum dot is ≈ 1 meV which leads to dynamics in the order of ≈ 5 ps. Assuming a transition of 1 µm and taking into account a SAW speed $v_{\mathrm{SAW}} \approx 2.86$ µm/ns, we find a flight time of $\Delta t \approx 350$ ps. In this scenario, a $\Delta E \approx 1$ meV $\cdot$ 350 ps/5 ps $= 70$ meV sets the upper limit for the energy change in the transition. Using a charge qubit defined in a static double-QD as reference, the energy scale is however ≈ 50 µeV [Pet10]. We find that in order to achieve an adiabatic transition in the 1-µm-long entrance, ΔE should be less than ≈ 4.5 meV. We note that even though these are rough estimations, they give us insights about the energy scale in our system.

In order to optimize the surface gates at the entrance of the coupling region, we simulate the electrostatic environment using the commercial software nextnano (for details, see Section 2.3). The potential landscape is benchmarked with modeling results from the state-of-the-art device [Tak19]. The final design is then nanofabricated in clean room facilities followed by characterizations at cryogenic temperatures.

Figure 4.1b shows a SEM image of the first generation of such an optimization process. In this linear-structure design, the QDs are directly facing the coupling region in order to avoid abrupt potential changes during electron transport. This device geometry revealed however several weaknesses owing to the close distance between the surface gates. First, we found a reduced readout fidelity due to crosstalks between electrometers. Second, the barrier gate had effectively multiple roles: it affects the potential landscape of the QDs, the QPCs and the TCW. This lack in flexibility limited the tuning of the sample.

In the next iteration, the quantum-dot design was upgraded while maintaining the linear injection structure (see Fig. 4.1c). Owing to the separation between the QPCs, no detrimental crosstalks were observed. Moreover, the QDs were better screened from the barrier via a pair of surface gates. We found however that the direct connection to the channel was a bottleneck for the implementation of our synchronized sending technique. This method requires first to set the source QD in a metastable position that holds the electron when the SAW passes. Only when a picosecond voltage pulse is applied on a surface gate of the QD, the potential is temporary lifted, and hence it triggers the electron transport. The strong coupling between the source dot and the channel in a linear structure limited the finding of such a metastable sending position.

Despite the fact that both investigated designs had their characteristic limitations, possible solutions were considered. Nevertheless, we decided to change our strategy to focus on an alternative approach. The idea is to first let the electron relax during its flight time in the coupling region. In order to manipulate the quantum state of the flying electron, we send a tailored voltage pulse to the barrier gate of the TCW to turn on the coupling between the two quantum rails. Such an in-flight control would allow us to investigate the dynamics of the electron inside the TCW.

To guarantee that the electron is relaxed to the ground state, we use as reference the relaxation time T_1 for a charge qubit [Pet10]. Assuming $T_1 \approx 10$ ns, the length of the TCW needs to be at least 30 µm. Figure 4.2 shows an SEM image of the sample for the implementation of such a dynamical control during the electron flight. To ensure the efficiency of the basic building blocks, we use

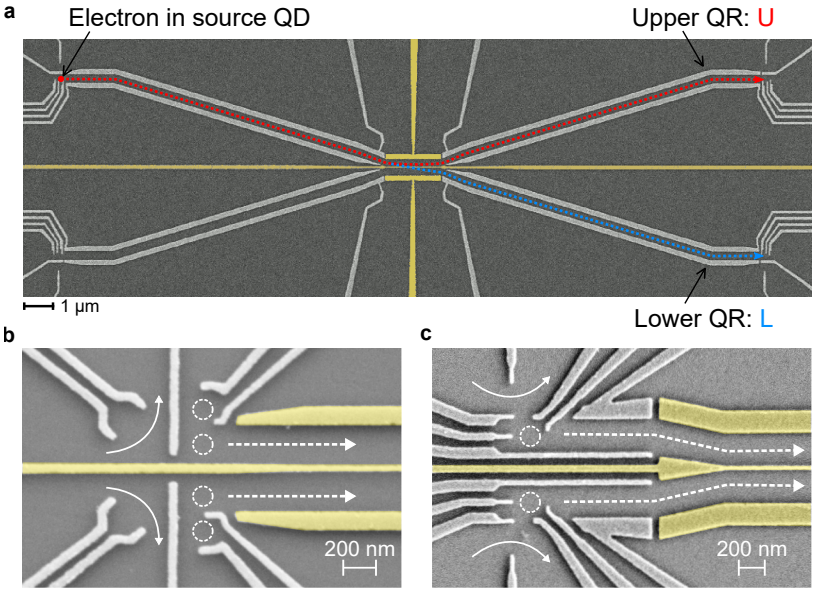

Figure 4.1: Devices with a coupled quantum rails. Investigated sample designs of a single-electron circuit with a pair of transport paths that merges into a coupling region. **(a)** State-of-the-art design reported by Takada *et al.* [Tak19]. The transport path for the injection of an electron into the TCW has an angle with respect to the SAW propagation direction. The possible trajectories of the electron are indicated by the red and blue arrows. The yellow surface-gates define the TCW. **(b)** Design based on a double-QD (circles) configuration as electron source with a direct connection to the coupling region. The current through a nearby QPC (solid arrow) is sensitive to the electron occupancy in the dot. The trajectory of the electron during transport is indicated by a dashed arrow. **(c)** Design with more control gates over the single-electron source while maintaining the linear injection structure.

a similar design to the state-of-the-art device with improved gate geometries. A pair of QDs are placed at each end of the rails, serving as single-electron sources and detectors. The TCW – that is 20 times longer than in previous work [Tak19] – extends over 40 µm where the two quantum rails are only separated by a narrow barrier that is defined via a 30-nm-wide surface gate. The transported electron then would experience a flight time of ≈ 14 ns inside the TCW. The experimental results presented in the course of this chapter are from measurements using this device.

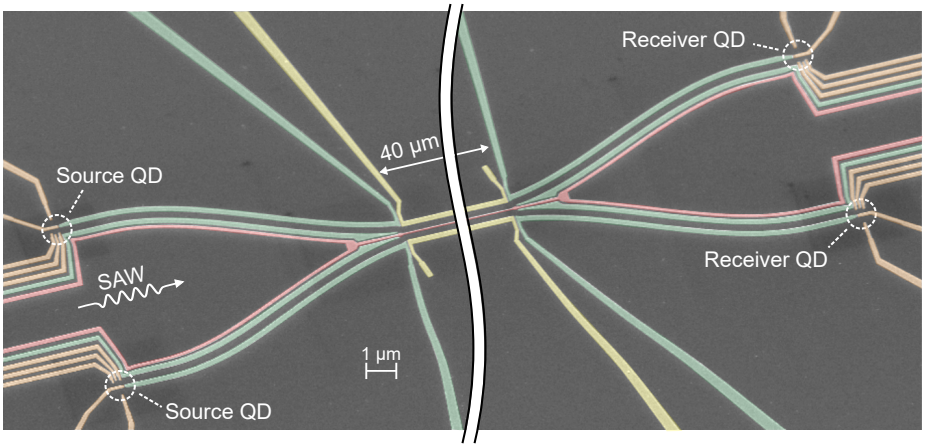

Figure 4.2: Sample for in-flight dynamical control. False-color SEM image showing the aerial view of the sound-driven circuit of coupled quantum rails. The entrance and exit paths are defined by the green surface-gates. The side gates (yellow) and the tunnel barrier (red) form the coupling region that extends over 40 µm. The QDs are indicated with circles.

4.2 Experimental setup

The investigated device was fabricated on a Si-modulation-doped GaAs/AlGaAs heterostructure grown by molecular beam epitaxy (MBE). The two-dimensional electron gas (2DEG) is located 110 nm below the surface with an electron density $n \approx 2.79 \times 10^{15}$ m^{-2} and a mobility $\mu \approx 9.1 \times 10^5$ cm^2 V^{-1} s^{-1}. This high-quality wafer is identical to the one employed previously for QPC devices – see Chapter 2.

The sample fabrication was carried out in the clean room facility of Néel Institute (CNRS). The surface gates defining the nanostructure as well as the transducer were realized with electron beam lithography. The most challenging pattern was the 30-nm wide barrier gate extending over 40 µm (aspect ratio $>$ 1000). The precise nanofabrication recipe is provided in Appendix A.2. We high-

light that during the fabrication process, critical technical problems were found – see details in Appendix A.3. By developing tailored solutions, I successfully increased the nanofabrication yield well above 90 %.

All experiments presented in this chapter were performed at a temperature of about 20 mK in a ^{3}He/^{4}He wet dilution refrigerator. The sample was connected electrically via 38 low- (DC) and 4 high-frequency (RF) lines. A DC line is made of either Constantan wires or Thermocoax which has low-pass-filter properties. For a RF line, we employ silver-plated stainless steel coax from 300 K to 4 K, and Nb coax for the low temperature stages (4 K to 20 mK). We employed thermal anchors and attenuators at different stages of the cryostat to thermalize respectively the DC and the RF lines.

The large amount of nanometric surface gates makes our samples very susceptible to electrical discharges. For this purpose, we always kept all connections grounded to a common mass during physical manipulations. We found however that a bad electrical line connection can induce abrupt voltage changes that damages permanently the nanodevices when it disconnects during cool down (see Appendix C.1). By methodically characterizing and repairing these lines, we were able to have a highly reliable experimental setup.

To manipulate the charge and the potential landscape in the nanodevice, we apply negative voltages on the surface gates. Typical safety values for GaAs devices are in the range of -2.2 to +0.35 V. In order to provide low-noise static voltages, we employ Digital-to-Analog Converters (DACs)[1] that are controlled by a Field-Programmable Gate Array (FPGA). Each DAC has a minimum setting time of 16 µs and a resolution of 153 µV.

Voltage signals above GHz frequencies are needed for fast manipulations. To drive the SAW formation, we use in most of the presented experiments a signal generator (Rohde Schwarz SMB 100A) that can provide up to 24 dBm. A high-power amplifier (ZHL-4W-422+) allows us to increase the input power up to 34 dBm. The sub-nanosecond voltage pulses for fast manipulations are generated by Arbitrary Waveform Generators (AWGs). To perform preliminary calibrations, we use Tektronix AWG7122b which has two channels with a sampling rate of 12 GS/s. For experiments with better time resolution, we employ two units of Keysight M8195A synchronized via the synchronization module M8197A. This setup allows us to have four channels (two per AWG) with sampling rates up to[2] 64 GS/s. The experimental setup of the RF connections are shown in Appendix C.2.

To count the number of electrons in a quantum dot, we measure the cur-

[1] DACs are custom-made by technicians in the Néel Institute with a noise level $\approx 25\ \mathrm{nV}/\sqrt{\mathrm{Hz}}$

[2] We have 64 GS/s if only one channel of each AWG is used. When four channels are active, each output can reach up to 32 GS/s.

rent through a QPC via an Ohmic contact. An operational amplifier at ambient temperature enhances the signal prior digitization with an Analog-to-Digital converter (ADC). The employed National Instrument ADC card allows real-time acquisition of multiple channels with a sampling rate up to 250 kS/s.

In order to perform single-shot experiments, we program the transport sequence into the FPGA. At first, we trigger the ADC to start the real-time acquisition that is followed by the voltage sequence for each DAC. Using the trigger outputs from the FPGA, we synchronize this execution with the high-frequency instruments. Characterizing with a real-time oscilloscope, we find that the maximum jitter in our setup is 5 ps.

The homemade software to control all the instruments is based on LabVIEW and Python. A safety layer is set on top of hardware limits providing the necessary extra protection. Due to the complexity of the measurements, automation scripts are routinely developed.

Let us now focus on the investigated sample. The nanodevice has 31 Schottky gates and 16 Ohmic contacts. The presence of more than 42 contacts represents the upper limit for the currently employed cryostat. Owing to this limitation, several Ohmics contacts are micro-bonded together, and thus share a common electrical line. On the other hand, a grounded metallic shield (not shown) covers the sample prior the cool down to avoid the propagation of evanescent electromagnetic (EM) waves from the IDT. A distance of ≈ 500 µm between the sample and the shield sets the maximum height for the micro-bonds. These limitations result into a tightly-packed bonding scheme as depicted in Fig. 4.3a. We note that, in order to scale up these devices, the setup needs to be upgraded to overcome these complexities.

Figure 4.3b shows an optical micrograph (OM) of the sample after nanofabrication. An IDT surrounded by metallic ground planes is placed at ≈ 1.5 mm away from the single-electron circuit at the center. Figure 4.3c zooms in on the regular Al transducer with double-finger design. This IDT with $\lambda = 1$ µm and $N = 111$ unit cells has the same nominal properties as the device characterized in Section 3.3. When a resonant input signal is applied, the emitted SAW propagates towards the single-electron circuit (see Fig. 4.3d). The nanostructure with 40-µm-long tunnel-coupled wire has a different color contrast due to the reduced metal thickness (4 nm Ti and 13 nm Au). Even though the optical microscope cannot resolve the details of the nanostructure, it allows us to perform a fast quality check of the device.

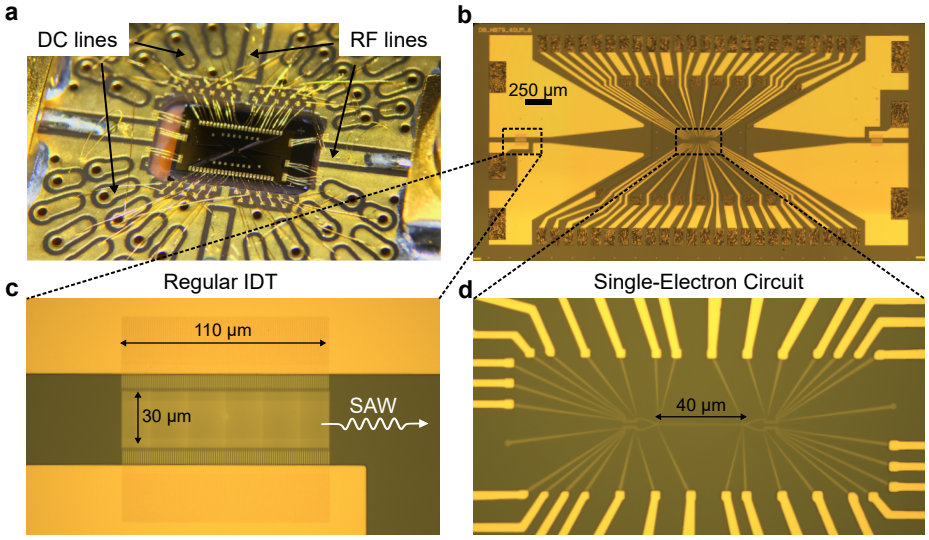

Figure 4.3: Device of coupled quantum rails. (a) Photograph of the sample on the printed circuit board (PCB) with Au micro-bonding wires. **(b)** Optical-microscope (OM) image of the investigated sample consisting of a single-electron circuit sandwiched between two regular IDTs. The metallic gates (yellow) serve as ground plane for the transducers and make the connection between the bonding pads (brown) and the nanodevice. **(c)** Zoom into the regular IDT with indication of the SAW propagation direction. **(d)** OM image of the single-electron circuit realized by electron-beam lithography. As a design redundancy, the barrier gate that forms the TCW can be connected via four contacts. Here, the two missing connections correspond to the unused contacts.

4.3 Single-electron control in a lateral quantum dot

The ability to initiate and to manipulate a single electron is a key requirement for SAW-assisted transfer. For this purpose, we use surface electrodes to define a lateral QD as shown in Fig. 4.4a. At cryogenic temperatures, we apply negative gate voltages to deplete the 2DEG underneath. With the gates labeled R (reservoir), P (plunger) and C (channel), we then create a confinement region – that is the QD – which can isolate down to one elementary charge. The electron occupancy in the dot is measured by a nearby QPC, serving as a non-invasive charge sensor [Fie93]. Figure 4.4b depicts schematically the potential U from the reservoir to the channel. To load an electron, the potential controlled by V_{R} and V_{C} is lowered to bring the QD below the Fermi level. Afterwards, this barrier is raised in order to isolate the charge from the reservoir.

Let us now describe the experimental protocol to tune the QD in the few-electrons regime. To calibrate the QPC as an electrometer, we set the current I_{QPC} in between the pinch-off and the first conductance plateau (see Fig. 4.5a). At this position, a change in the surrounding electric field induces a shift in the

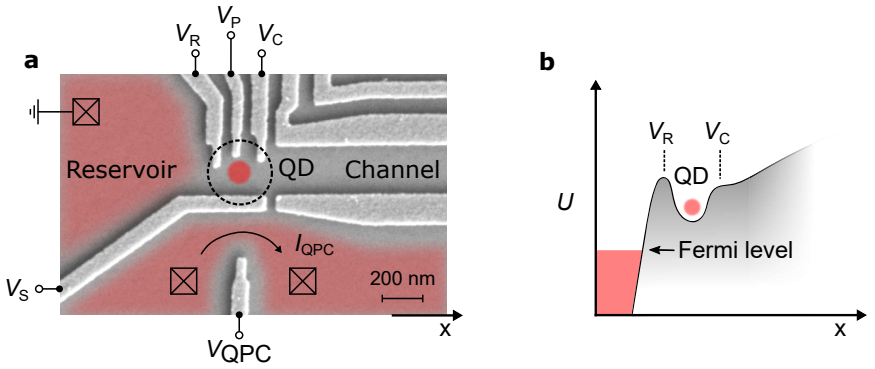

Figure 4.4: Lateral quantum dot. **(a)** SEM image of the surface gates defining the quantum dot with a nearby QPC as a sensitive electrometer. The false color indicates schematically the 2DEG around the structure when negative voltages are applied on the surface gates. A QD is formed between the channel and the reservoir that can isolate a controlled number of electrons. **(b)** Schematic potential landscape from the reservoir to the channel in a condition where the QD is isolated from the reservoir.

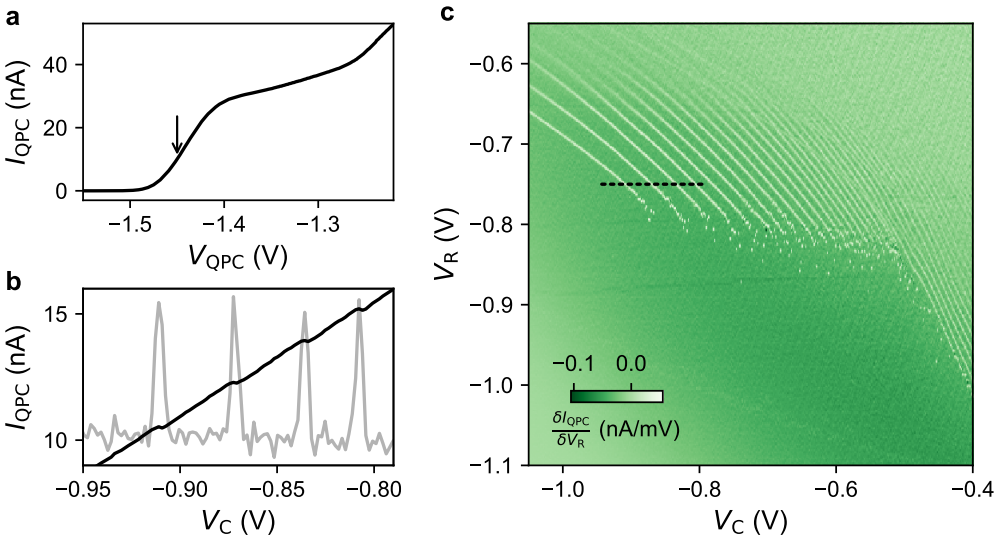

Figure 4.5: Charge stability diagram of a quantum dot. **(a)** Current I_{QPC} through the QPC near the pinch-off. The working point for charge sensing is indicated by the arrow. **(b)** I_{QPC} (black) and its derivative (grey; arbitrary units) as a function of V_{C}. This data is a slice (dashed line) from **(c)** a two-dimensional scan of the derivative of I_{QPC} with respect to V_{R}.

QPC conductance. Figure 4.5b shows I_{QPC} as a function of the channel gate V_{C}. Despite the linear baseline due to electric crosstalk, jumps in the current are visible. The contrast of these jumps is enhanced in the derivative of the signal (grey). Each peak, also known as Coulomb peak, is the result from a change of one electron in the QD.

In order to have a full picture of the QD occupancy, we perform a two-dimensional (2D) scan with respect to V_{R} and V_{C}. This so-called charge stability diagram is shown in Fig. 4.5c. Each line corresponds to the loading of one electron in the dot. For negative enough V_{C}, the absence of Coulomb peaks indicates that no electrons are left in the QD. A remarkable feature is the fading of the lines at $V_{\mathrm{R}} \approx -0.80$ V. When the barrier to the reservoir is raised (more negative voltages), the process of tunneling out of the dot becomes infinitely slow, hence the electrons are trapped in the QD. We later exploit such an isolated regime to prepare and to catch single electrons.

For electron-quantum-optics experiments with SAW, we aim to perform single-shot measurements. For this purpose, each measurement consists of a sequence of voltage pulses on the surface gates. A standard loading sequence is depicted on top of the stability diagram shown in Fig. 4.6a. The default position of the QD is set in the isolated regime (M) where the QPC is tuned for the highest charge sensitivity. We first empty the QD with zero electrons by moving to the initialization position (I). Returning to M, we measure the QPC current as reference. Subsequently, the QD is brought to the loading position (L) for typically 100 µs, and move back to M for the current readout. Figure 4.6b shows an example of I_{QPC} measured in real time for the loading of one electron. Current fluctuations at sequence steps I and L (grey) are caused by gate crosstalks, hence they can be ignored. A visible current jump ΔI that appears after exploring L indicates a change in the QD occupancy.

To prepare an exact number of electrons, we explore a wide range of loading positions via V_{R} and V_{C} at sequence step L. Figure 4.6c shows ΔI of such a loading map. Discrete regions correspond to positions where a controlled number of electrons is loaded and isolated in the QD. The quality of the QPC sensor is reflected in the ΔI histogram shown in Fig. 4.6d. Owing to the well-separated peaks, we are able to readout the electron number with a fidelity beyond 99 %. In order to characterize the loading efficiency, we perform 1000 single-shot measurements at different V_{C} (see Fig. 4.6e). Plateaus with nearly unity probability indicate the positions to prepare few electrons with extremely high fidelity.

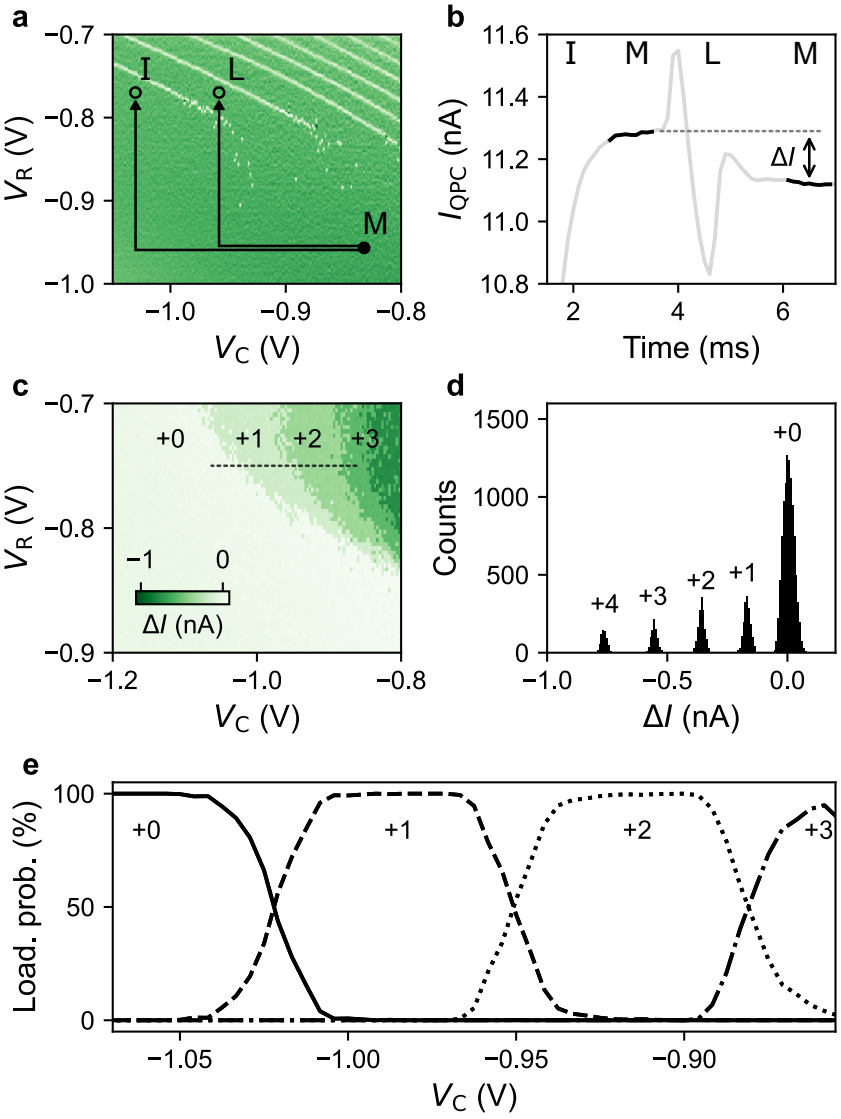

Figure 4.6: Loading of electrons. **(a)** Charge stability diagram with indications of sequential voltage positions for QPC measurement (M), QD initialization (I) and single-electron loading (L). **(b)** Example of I_{QPC} measured in real time of the loading sequence for one electron. The signals at the measurement position M are highlighted in black. The variation in the QD occupation is reflected in the current difference ΔI. **(c)** Two-dimensional scan of loading positions. The discrete colors indicates the electron occupancy in the QD. **(d)** Histogram of the data from (c) showing distinct peaks of QPC current jumps ΔI. **(e)** Loading probability from single-shot measurements along the dashed line indicated in (c).

4.4 SAW formation at cryogenic conditions

To prepare the system for SAW-assisted transport, we first characterize the resonance frequency of the IDT at cryogenic temperatures. For this purpose, we use the surface gates at the coupling region to create a narrow constriction near the pinch-off. When the SAW amplitude is sufficiently strong, such a propagating potential can shuttle electrons across the barrier [Shi96]. Figure 4.7 shows the SAW-induced current as a function of the frequency of the input signal on the IDT. We find a resonance frequency ≈ 2.86 GHz with side peaks in good agreement with VNA measurements at room temperature (see Fig. 3.5c in Section 3.3.1). Note that this value slightly deviates from characterizations at ambient conditions (2.83 GHz) due to the temperature dependence of SAW velocity [PSK19].

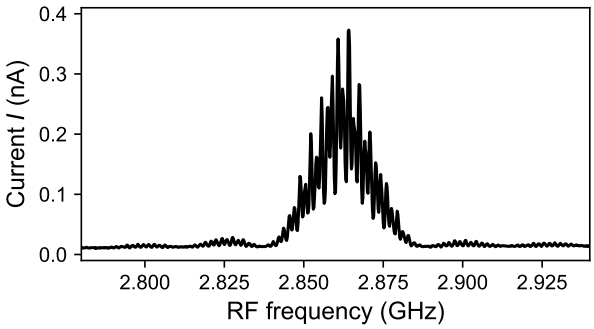

Figure 4.7: Acousto-electric current. Current I through a narrow constriction defined by the channel gates (see yellow gates in Fig. 4.2) in the presence of SAW. The measurements were performed at base temperature ≈ 20 mK. The input signal has 50 % duty cycle, 10 µs period and 0 dBm input power. The resonance frequency f_0 is ≈ 2.86 GHz.

The SAW amplitude determines the confinement efficiency along the propagating direction of a flying electron [Edl21]. In order to investigate how the input power P relates to the amplitude of the SAW, we measure the SAW-induced modulation of Coulomb-blockade resonances of a quantum dot. We apply a DC bias voltage V_{SD} between Ohmic contacts on each side of the QD and measure the signal with a current-voltage converter. Figure 4.8a shows the conductance across one of the source QD as a function of V_{SD} and the plunger gate voltage V_{P}. From the characteristic Coulomb diamonds, we can extract the quantum dot's charging energy E_{C} and the voltage spacing V_{C} between Coulomb-blockade peaks. The voltage-to-energy conversion factor is thus $\eta = E_{\mathrm{C}}/V_{\mathrm{C}} \approx 0.05 \pm 0.01$ eV/V. Knowing η, we can now deduce the peak-to-peak amplitude A of the SAW from a given input power P via the relation:

$$A\ [\mathrm{eV}] = 2 \cdot \eta \cdot 10^{\frac{P\ [\mathrm{dBm}] - P_0}{20}}, \tag{23}$$

where P_0 is a fit parameter accounting for power losses. P_0 is determined by comparison with equation 23 to the SAW-induced broadening of the Coulomb-blockade resonances.

Figure 4.8b shows a conductance measurement as function of V_P and P for $V_{SD} \approx 20$ µV. The data shows Coulomb-blockade peaks that broaden according to equation 23 if $P_0 \approx 36.8 \pm 0.3$ dBm as indicated by the solid lines – the dotted lines represent the error margin. Extrapolating A to the maximum employed input power of $P \approx 28$ dBm, we can estimate $A \approx 42 \pm 13$ meV (see Fig. 4.8c). This amplitude lies beyond the value $A \approx 17 \pm 8$ meV reported from the state-of-the-art device of coupled quantum rails [Tak19] (lower horizontal line) which indicates that we have successfully improved the SAW confinement. To estimate if the transported electron would stay within a SAW minimum, we compare A with the 95 % confinement threshold of $A \approx 24$ meV that was deduced from time-of-flight measurements along a straight quantum rail [Edl21] (upper horizontal line). Our results indicate that the employed SAW power should be strong enough to ensure in-flight confinement.

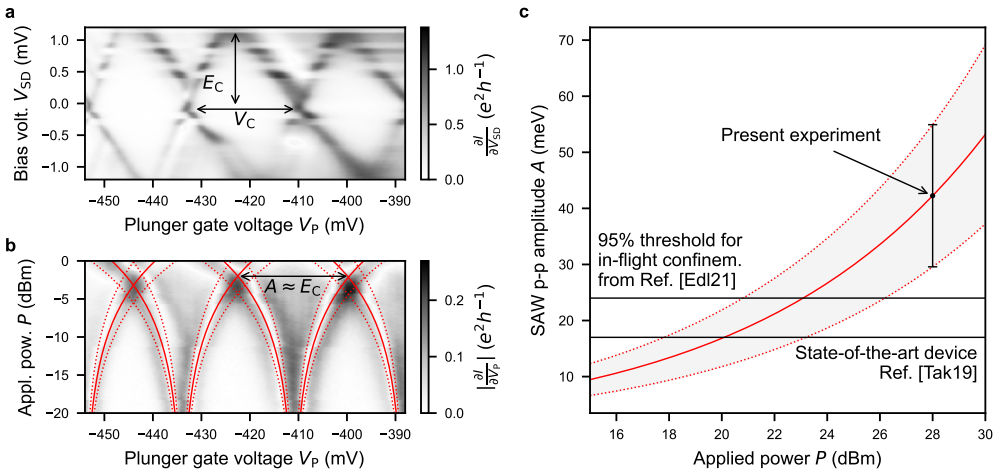

Figure 4.8: Extrapolation of SAW amplitude from quantum-dot modulation. (a) Coulomb diamonds from one of the source QDs. The data shows a transconductance measurement as function of the bias voltage V_{SD} and the voltage V_P applied on the plunger gate. The arrows indicate the charging energy E_C and the gate-voltage period, V_C, of the resonances. **(b)** Broadening of the Coulomb peaks as function of P. The double-headed arrow indicates the value of P where the peak-to-peak amplitude A of the SAW matches E_C. **(c)** Extrapolation of A for P up to 30 dBm. The errorbar indicates the estimation of A for the present experiment.

4.5 SAW-assisted transport

Having verified the IDT characteristics at cryogenic conditions, let us now describe the tuning protocol for single-electron transport. The loading positions are first calibrated for each QD. We then investigate the sending (holding) positions in the source (receiver) QD in the presence of SAW. To ensure unambiguous transport, we mitigate the SAW-driven injection of unwanted electrons in the circuit as well as optimize the initialization process. Setting a large barrier in the coupling region, we define two independent paths. To verify that the electron sent from the source is the same that arrives at the receiver, we analyze the complementary changes from the respective electrometers. Finally, we optimize the potential along the quantum rails to improve the transport efficiency.

The challenge to optimize such a circuit with coupled quantum rails is the mutual influence between the surface gates. A typical example is the injection path before the TCW. Voltages applied to the entrance gates affect the sending efficiency in the source QD as well as the potential profile near the coupling region. Therefore, the optimization of SAW-assisted transport is an iterative process.

Let us start with investigations on the sending positions in one of the source QDs. For this purpose, we employ a voltage sequence similar to the loading protocol. We first move the QD to a loading position L and go back to the measurement position M to readout the current. To explore possible sending positions S, we apply gate voltages V_{R} and V_{C}. Before returning to M, we can trigger the SAW emission for electron transport. By comparing the current jump ΔI as in the loading sequence, we deduce the change in electron number.

Figure 4.9a shows the change in the QD occupancy for such an experimental sequence without SAW emission. In this example, two electrons are previously loaded in the source QD. Discrete regions appear as the consequence of reducing the number of electrons in the QD. When the channel potential is higher, *i.e.* more negative V_{C}, the electrons are lost to the reservoir. There is however a metastable region where the two electrons remain in the dot after the gate voltage movements (dark green area).

Having identified the positions to hold the prepared electrons, we trigger for SAW emission. Figure 4.9b shows the QD-occupancy map after driving the IDT for 50 ns at the resonance frequency. The presence of SAW results in a new region (dotted area) where 2 electrons are lost. Note that more electrons disappear when the reservoir gate V_{R} is more negative. Considering this feature and the SAW propagation direction, we conclude that the electrons are sent into the channel.

To ensure highly efficient transport, we verify if SAW injects extra electrons through the source. For this purpose, we perform the same measurement with an initially emptied QD (see Fig. 4.9c). At low gate voltages where the dot is

coupled to the reservoir, SAW loads extra electrons. At the possible sending positions however, no injection of electrons occurs.

Applying this protocol to one of the receiver QDs, we investigate for catching positions. Similar to the sending sequence, the receiver dot is first initialized at a loading position. Then, we explore for possible catching positions with voltages applied to its reservoir V_R and channel V_C gates. After coming back to the measurement position, we measure the current jump ΔI to evaluate the change

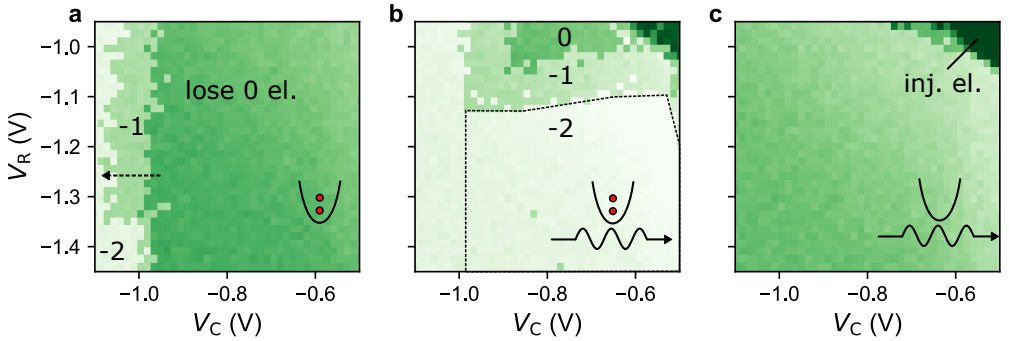

Figure 4.9: Example of sending maps. (a) Two-dimensional scan for sending positions controlled by V_R and V_C of a source QD loaded previously with 2 electrons. The reduction in electron occupancy is reflected in the discrete QPC current jumps (color). The arrow indicates the losing of electrons to the reservoir. **(b)** Same measurement as in (a), but with a SAW burst from an input signal of 50 ns and 24 dBm at the sending position. The dotted area highlights the losing region due to SAW. **(c)** Reference measurement with no electron loaded prior applying SAW with indications of injected electrons.

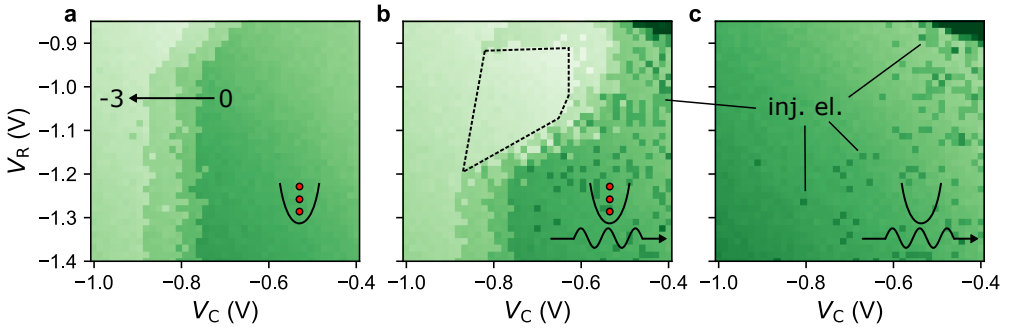

Figure 4.10: Example of holding maps. (a) Electron-occupancy map for holding positions at a receiver QD loaded previously with 3 electrons. **(b)** Same measurement as in (a), but with a SAW burst from an input signal of 50 ns and 24 dBm at the holding position. The dotted area highlights the losing region due to SAW. **(c)** Reference measurement with an empty receiver dot in the presence of SAW with indications of the injected electrons.

in QD occupancy. To ensure that no electrons are injected from the source side, we isolate the source QDs as well as the coupling region with negative voltages.

Aiming to catch up to 2 electrons, we prepare 3 electrons as a reference. Figure 4.10a shows the change in QD occupancy after exploring a holding position via V_R and V_C without SAW emission. As for the source QD, we identify the regions where the electrons are lost to the reservoir due to gate movements. When SAW is present, a new losing region appears (see dotted area in Fig. 4.10b). In contrast to the source QD, there is a large region at negative V_R where all electrons are kept. We thus identify in such a holding map the possible catching positions.

There are however signatures of extra electrons in the holding region. To study the origin of these particles, we perform a reference measurement with loading no electrons in the QD prior to SAW emission (see Fig. 4.10c). The similarity of the signals confirms that SAW loads extra electrons to the dot. This particular example shows our protocol to identify SAW-injected electrons. By quantifying these unwanted electrons as a function of the surrounding gate voltages, we are able to mitigate this effect.

Having calibrated independently the QDs, we proceed to perform single-electron transfer along the quantum rail. With an optimized catching position, we load two electrons in the source QD and trigger the SAW emission. Figure 4.11 shows the simultaneously-measured occupancy map for the source and receiver QDs at different sending positions V_R and V_C. In such transfer maps, the complementary regions demonstrate that the electron sent is the one that is caught.

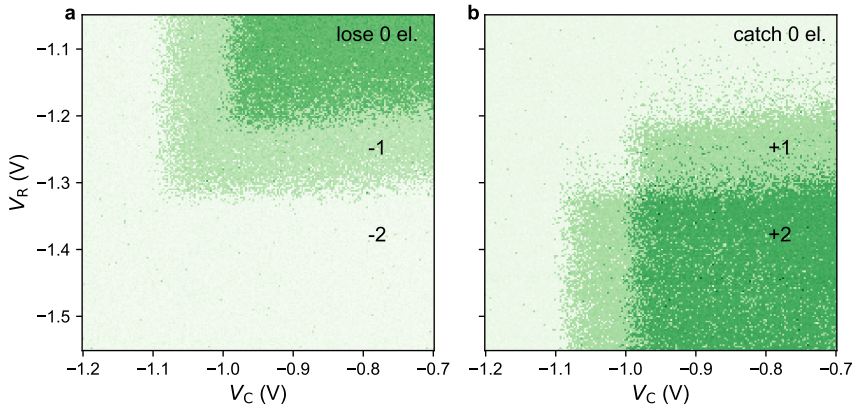

Figure 4.11: Example of transfer maps. Complementary electron-occupancy maps as a function of sending positions V_R and V_C after the SAW burst passes **(a)** the source QD and **(b)** the receiver QD. 2 electrons are previously loaded before triggering for SAW formation.

Another source of error is related to the initialization of the system. For each transfer sequence, the single-electron circuit is completely depleted prior loading of electrons in the source QDs. It can happen however that the transported electron is stuck in a quantum rail. In this scenario, this electron is usually recovered in the next measurement sequence. In order to properly initialize the system, we generate few SAW bursts at the beginning of each run as cleaning sequence. The source QDs are set at the sending position to allow any remaining electron to cross the circuit. In contrary, the detector QDs are positioned at the zero-electron regime where they are strongly coupled to the reservoir. When the SAW train propagates, it picks up the 'stuck' electrons and unloads them at the receivers. Optimizing the cleaning positions, we achieve highly efficient and unambiguous SAW-assisted transfer beyond 99 %.

4.6 Delay-controlled sending process

Electron-quantum-optics experiments with several single-electron sources requires synchronization. The presence of typically hundreds of potential minima within the SAW train makes the location of the electron during the flight ambiguous. To overcome this limitation, we employ a delay-controlled sending process on each source QD [Tak19]. The idea is to set the potential of the dot in a metastable position where the electron cannot be picked up by the propagating SAW. When a fast voltage pulse is applied to the plunger gate P (see Fig. 4.12a), the potential is temporary lifted, and thus it triggers the electron transport. By controlling the pulse delay t_{P} with respect to the SAW emission (see Fig. 4.12b), we are able to address a particular minimum within the SAW train.

Let us now describe our protocol to optimize such a synchronization technique. The contrast between the sending and holding efficiency at the metastable position determines the accuracy of the triggered transport. To find the optimum condition, we first investigate the influence of the DC voltage bias on P. For this purpose, we add in the sending sequence V_{P} before the SAW emission. Figure 4.12c shows a single-electron sending map as a function of V_{R} and V_{P} in the presence of SAW. The sharp transition (tens of mV) from holding to losing the electron indicates that a negative voltage pulse on P would allow to transit from a well protected position to a sending configuration.

The next step is to characterize the SAW arrival time at the source QD. For this purpose, we fix $V_{\mathrm{P}} = 0$ V and apply a negative square pulse of duration $\Delta t_{\mathrm{P}} = 1$ ns via the RF port of the bias tee on P. The envelope of the SAW profile emerges as we scan the trigger pulse delay t_{P} as shown in Fig. 4.12d. The characteristic plateau (see Section 3.3.3) of $t_{\mathrm{Sig.}} - t_{\mathrm{IDT}} \approx 10$ ns confirms that the signal corresponds to the SAW.

To address a particular SAW minimum, we then reduce the pulse duration

Δt_P to be shorter than the SAW period $T_{SAW} \approx 350$ ps. Figure 4.12e shows the delay-controlled sending map as a function of V_R and t_P with $\Delta t_P \approx 90$ ps. The periodic fringes reveal the locations of the SAW minima. In order to characterize the transfer efficiency at the optimum metastable position ($V_R = -1.05$ V), we perform 1000 single-shot measurements as a function of t_P (see Fig. 4.12f). For the on- and off-status of the triggered transport, we find a contrast in the transfer efficiency between (0.35 ± 0.24) % and (99.77 ± 0.25) %. This result demonstrates our ability to address a particular SAW minimum for the electron transport.

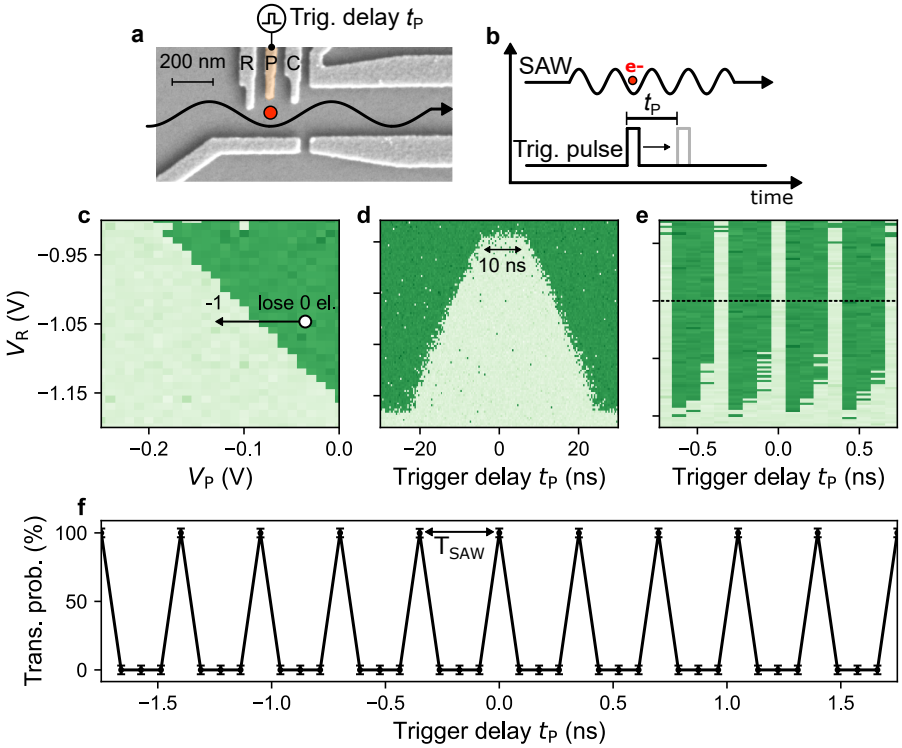

Figure 4.12: Delay-controlled sending process. (a) SEM image of the lower source QD. A bias tee is connected to the plunger gate P (orange) to trigger the sending process. **(b)** Schematic of the delay-controlled loading of an electron into the SAW. A voltage pulse is applied on P with a delay t_P and pulse duration Δt_P. **(c)** Sending map at the source QD with indication (arrow) of the effective transition if a negative trigger pulse is applied. **(d)** Delay-controlled sending measurement as a function of V_R and t_P. V_R range is from -0.93 to -1.13 V. V_P is fixed to 0 V. The trigger pulse is applied for a duration $\Delta t_P = 1$ ns. The envelope of the SAW profile has a plateau (double arrow) ≈ 10 ns. **(e)** Zoom into the SAW plateau around $t_P = 0$ with $\Delta t_P \approx 90$ ps. V_R range is from -0.98 to -1.16 V. **(f)** Transfer probability at a fixed sending position $V_R = -1.05$ V (see dashed line in (e)). The separation between the peaks matches $T_{SAW} \approx 350$ ps.

4.7 High-SAW-power limit

Having described the protocol to optimize the SAW-assisted electron transport, let us now investigate the maximum employable SAW amplitude. A strong SAW confinement is necessary to avoid electron excitation [Tak19] and electron tunneling to subsequent SAW minima [Edl21]. Increasing SAW power has however important drawbacks such as injection of unwanted electrons. Specifically, this implementation is detrimental for the delay-controlled sending process.

Figure 4.13a and b show the change in the sending region for two input powers on the IDT: 25 and 29 dBm. The optimum metastable position for triggered transport is at low V_R where the coupling to the channel is weaker. When the SAW amplitude is increased, this metastable region is significantly reduced. Figure 4.13c shows the sending map as a function of V_R and the input power on the IDT. The size of the metastable region is linearly decreasing with larger RF power. Owing to this limitation, the maximum power in the investigated sample is restricted to 28 dBm.

Is this SAW confinement sufficient for synchronized transport? From Coulomb-diamond measurements shown in Section 4.4, 28 dBm is equivalent to a SAW amplitude of $A \approx 42$ meV. Using the 95 % confinement threshold of 24 meV extracted from time-of-flight measurements [Edl21], this SAW power should be strong enough to ensure the electron to stay in the addressed SAW minimum.

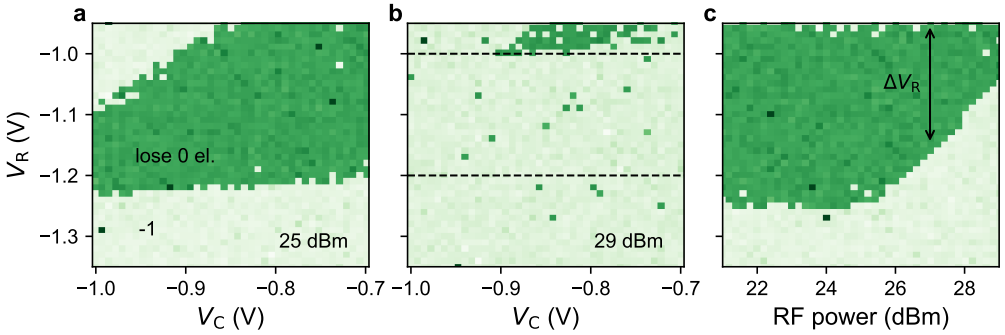

Figure 4.13: High SAW power. Sending maps at the source QD for an applied RF power for SAW formation of **(a)** 25 dBm **(b)** and 29 dBm. Electron-occupancy map at $V_C = -0.85$ V as a function of RF power. The size of the holding region is quantified via ΔV_R.

4.8 Partitioning of a flying electron

So far, the single electron is transported only along one quantum rail. Once all QDs are calibrated, we lower the barrier-gate voltage V_B that forms the TCW (see Fig. 4.14a) to allow the coupling between the transport paths. In this configuration, we proceed to realize another essential building block for electron-quantum-optics experiments: on-demand electron partitioning. The idea is to control the transmission probability of the flying electron from one rail to another. For this purpose, we use the upper (V_U) and the lower (V_L) channel gates to tilt the potential in the TCW. Figure 4.14b shows the transfer probability of an electron from the upper source QD to the lower (P_{10}) and to the upper (P_{01}) detector QD as a function of the voltage detuning $\Delta = V_U - V_L$. The gradual transition of the probability follows a Fermi function

$$P_{10}(\Delta) = \frac{1}{\exp\left(\frac{\Delta-\Delta_S}{\sigma}\right)+1} \tag{24}$$

with 50:50 transmission at a detuning Δ_S and a characteristic transition width σ. These results demonstrate our ability to partition a flying electron with controlled transmission probability.

The transition width σ is related to the energy of the electron [Tak19]. In order to extract the mean excited energy ε – that is equivalent to an effective temperature –, we employ a stationary model of the eigenstates in the tunnel-

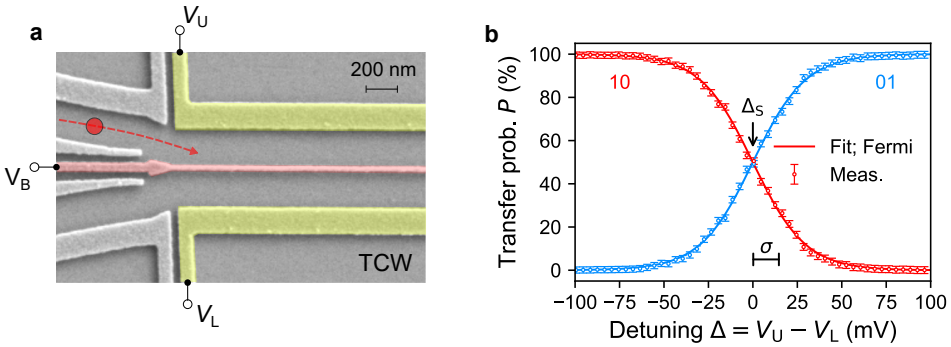

Figure 4.14: Partitioning of a single electron. (a) False-color SEM image of the entrance to the TCW with indications of an electron injected from the upper source QD. **(b)** Probability, P, to end up in the upper (01) or lower (10) quantum rail for different values of potential detuning Δ for triggered SAW-driven emission. The lines show a fit by a Fermi function (see equation 24) with offset Δ_S and width σ. Here, the barrier voltage is set to $V_B = -1.10$ V, and $V_U = V_L = -1.00$ V at Δ_S.

coupled region. In this model, we define an one-dimensional Schrödinger equation

$$\frac{\hbar^2}{2m_e}\frac{\delta^2\psi(y)}{\delta y^2} + U(y|V)\cdot\psi_i(y) = E_i\psi_i(y) \tag{25}$$

along the transverse direction y of the TCW. ψ_i and E_i are the eigenfunctions and eigenvectors, m_e is the effective electron mass in a GaAs crystal, and $U(y|V)$ is the electrostatic double-well potential defined by the surface-gate voltages V containing V_U, V_L and V_B. This potential is obtained by solving the corresponding Poisson equation.

In order to include excitation in the model, we associate an occupation p_i for each eigenstate ψ_i. The probability of finding the electron in the upper quantum rail is then defined as:

$$P_{01} = \sum_i p_i \int_{y>0\ \mathrm{nm}} \left|\psi_i(y, U(y|V))\right|^2 dy \tag{26}$$

We then assume that the occupation of the eigenstate E_i follows a Boltzmann distribution

$$p_i \propto \exp\left(-\frac{E_i - E_0}{\varepsilon}\right) \tag{27}$$

where E_0 is the energy of the ground state for a certain potential configuration. Here, ε is equivalent to an effective temperature. To illustrate this model, Figure 4.15a shows the occupation in a symmetric double-well potential for $\varepsilon > 0$.

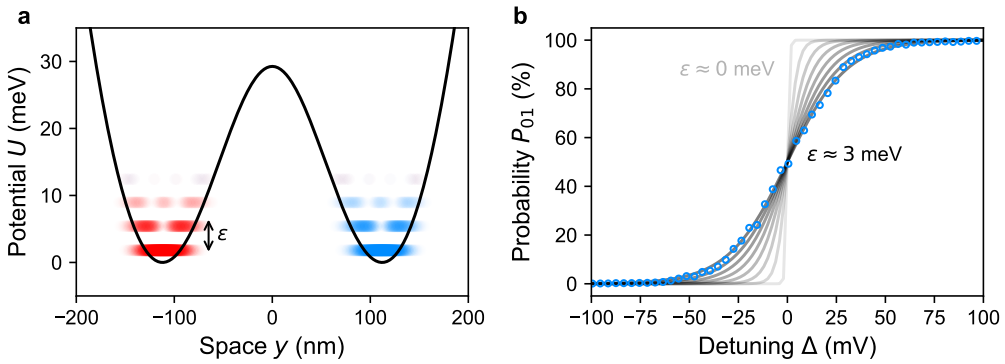

Figure 4.15: Simulation of electron partitioning with excitation. (a) Numerical simulation using nextnano of the potential profile in the transverse direction along the TCW with $V_\mathrm{B} = -1.10$ V, and $V_\mathrm{U} = V_\mathrm{L} = -1.00$ V. The energy levels in each quantum rail are occupied with a mean excitation ε following a Boltzmann distribution. **(b)** Simulated probability P_{01} (grey lines) to find the electron in the upper quantum rail as a function of the detuning Δ for increasing ε. The experimental data points (blue) are shown as reference.

For higher energy levels, the occupation probability decreases exponentially. Owing to the symmetry of this example, the electron has 50 % probability to be found on each side.

To reproduce the experimental partitioning data, we use ε as a fitting parameter. Figure 4.15b shows the evolution of P_{01} as a function of Δ for increasing ε. With a transition width $\sigma \approx 15$ mV, we find that the flying electron has a mean excited energy of $\varepsilon \approx 3$ meV. Compared to our previous design [Tak19], we observe a reduction of ε which we attribute to the increased SAW confinement and the improved surface-gate design at the transition region to the TCW.

A possible cause for the electron excitation is the trigger pulse employed for

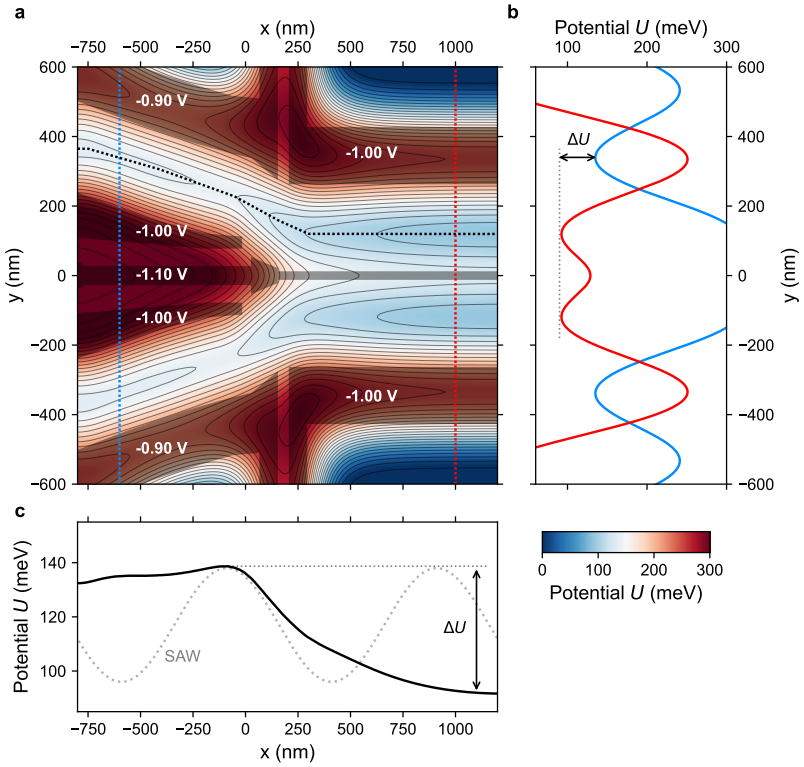

Figure 4.16: Potential landscape at the entrance of TCW. (a) Potential U from nextnano simulations with realistic gate geometries (black polygons) and input voltages. Solid traces indicate the equipotential lines. **(b)** Potential profiles in the transverse direction of the quantum rails before ($x = -600$ nm) and after ($x = 1000$ nm) the entrance to the TCW. The bottom of the confinement potentials have a difference $\Delta U \approx 40$ meV. **(c)** Potential profile that follows the minimum of the confinement potential along the upper quantum rail. This trajectory is depicted as a black dotted line in (a). A SAW modulation with amplitude $A = 42$ meV is plotted (dotted grey line) as reference.

the delay-controlled sending process. To verify this hypothesis, we perform the same partitioning experiment with the difference of sending the electron without the trigger pulse. We find that ε does not change, hence we conclude that the sending process has negligible effect on the excitation.

Let us now focus on the injection process of the single electron into the TCW. Figure 4.16a shows the potential landscape U from nextnano simulations near this region. The transported electron is initially at the upper rail which is narrower than the coupled region. Comparing the transverse potential profiles before and after the entrance (see Fig. 4.16b), we find that the electron experiences a transition from an effective one-dimensional channel to a double-well potential. We observe that the injection path has a significantly higher potential than the coupling region. This difference $\Delta U \approx 40$ meV is better seen in the potential profile of the electron trajectory shown in Figure 4.16c. Note that ΔU is comparable to the SAW peak-to-peak amplitude. Our simulations indicate that the most likely source of excitation in our system comes from the injection process of the electron into the coupling region.

A strategy to overcome this non-adiabatic transition is to control the barrier height in *real time*. To achieve this, we can apply sub-nanosecond voltage pulses with tailored waveforms via the RF port of the bias tee connected to the barrier gate. Details of such experiments will be discussed in Chapter 6

4.9 Conclusion

In conclusion, we have presented the calibration protocols for an optimized single-electron circuit with coupled quantum rails. We described the cryogenic setup and the instruments for electrical manipulations. Performing single-shot measurements, we showed our ability to load single electrons in the QDs with extremely high fidelity. We optimized the sending and catching positions to achieve unambiguous SAW-assisted transfer along the quantum rails. We implemented the delay-controlled sending technique that enables the synchronization of the single-electron sources. Finally, we realized the electronic version of a beam splitter via the partitioning of the flying electron. In the next chapter, we will combine these building blocks to investigate the interaction between a pair of flying electrons.

CHAPTER 5

Antibunching of flying electron pair

Quantum statistic governs the outcome of single-particle interference. Basic setups to explore quantum correlations incorporate a single beam splitter. A well-known example is the Michelson interferometer. The first implementation allowed Albert Michelson and Edward Morley to demonstrate the non-existence of the hypothetical medium called ether [MM87]. Since then, this setup has been employed in countless experiments such as for the recent observation of gravitational waves [Abb16].

In contrast to the phase correlation, interference effects based on the *intensity* are also governed by quantum statistic. Two important examples are the Hanbury-Brown and Twiss (HBT) [HBT56] and the Hong-Ou-Mandel (HOM) [HOM87] interferometers – the latter being the main focus of this chapter. Let us first briefly describe in the following the basic concepts of such interferometers before the implementation in our single-electron circuit.

Figure 5.1 depicts schematically the HBT interferometer where a stream of particles (bosons or fermions) is partitioned by a 50:50 beam splitter. In the original work by Hanbury Brown and Twiss [HBT56], they employed a beam of photons and counted the scattered particles with photodetectors. The normalized

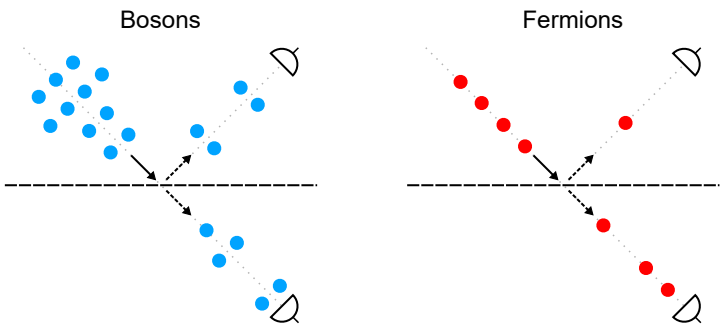

Figure 5.1: HBT interferometer. A beam of particles (bosons or fermions) arrives at a 50:50 beam splitter. After the scattering, the particles are measured by independent detectors at each output port.

second-order correlation function between the detectors can be expressed as

$$g^{(2)}(t) = \frac{\langle I(t)I(t+\tau)\rangle}{\langle I(t)\rangle^2} \tag{28}$$

where $\langle I(t)\rangle$ is the statistical averaged intensity at one detector, t is the time interval between photons and τ is the time delay between the two intensity readings. If the source emission process follows a Poisson distribution, *i.e.* independent events, we expect $g^{(2)}(\tau = 0) = 1$. This is the case for coherent and monochromatic light sources [BE11]. In a thermal light source however, $g^{(2)}(\tau = 0) = 2$ because bosons tend to cluster (bunching) owing to Bose-Einstein statistics [HBT56]. In the opposite end, a source which emits single photons would yield full anti-correlation $g^{(2)}(\tau = 0) = 0$ [Som16; Din16] since only one particle is detected at the time. Owing to these intensity correlations, HBT setup is widely used to determine the type of photon source.

In contrast to bosons, fermions tend to repel each other (antibunching) due to Pauli exclusion principle. Therefore, the second-order correlation for a degenerated beam of fermions is expected to be fully anti-correlated $g^{(2)}(\tau = 0) = 0$. Such fermionic antibunching has been observed in solid-state devices [Oli99; Hen99] and also with field-emitted electrons in vacuum [KRH02]. It is important to highlight that Coulomb repulsion would also yield to sub-Poissonian statistics [KOT11; Bel19]. For this reason, it is challenging to distinguish experimentally which mechanism dominates in quantum correlations with fermions: Pauli exclusion or Coulomb interaction.

In the investigated circuit of coupled quantum rails, the single-electron partitioning experiment is equivalent to the HBT setup (see Section 4.8). In each transport sequence, the flying electron is detected either in the upper or the lower QD. We use such anti-correlation to evaluate the efficiency of our SAW-assisted single-electron sources.

The second-order correlation is also at the heart of the HOM interferometer. In contrary to the HBT setup, here two particles with a delay τ are injected from each input port of the beam splitter as depicted in Fig. 5.2a. For synchronized arrival ($\tau = 0$), there is a maximal overlap between the incident wavefunctions. After scattering in a beam splitter at 50 % transmission, we can derive – see Appendix D.1 – the output states for:

$$\text{bosons} \rightarrow \frac{1}{2}\,|2,0\rangle + \frac{1}{2}\,|0,2\rangle \tag{29}$$

$$\text{fermions} \rightarrow |1,1\rangle \tag{30}$$

$$\text{classical} \rightarrow \frac{1}{4}\,|2,0\rangle + \frac{1}{2}\,|1,1\rangle + \frac{1}{4}\,|0,2\rangle\,. \tag{31}$$

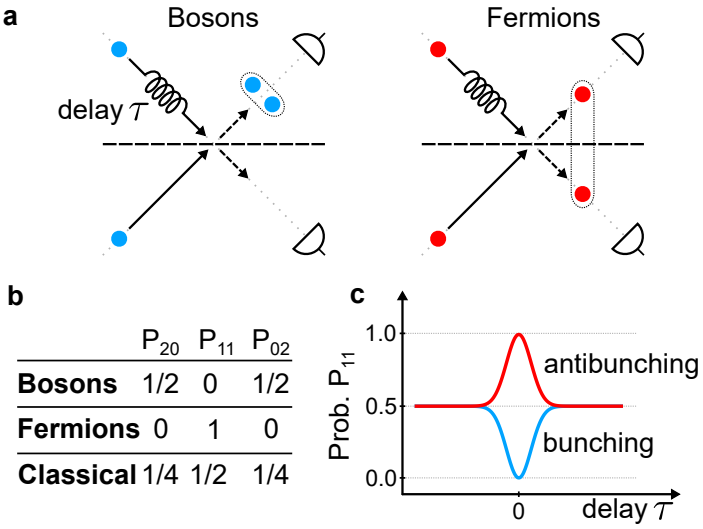

	P_{20}	P_{11}	P_{02}
Bosons	1/2	0	1/2
Fermions	0	1	0
Classical	1/4	1/2	1/4

Figure 5.2: HOM interferometer. (a) Schematic setup where two particles (bosons or fermions) with a given delay τ collide in a beam splitter at half transmission. Simultaneous particle counts are recorded by independent detectors at the output ports. **(b)** Table of expected probabilities P_{20} (two particles at the lower detector), P_{11} (one at each detector) and P_{02} (two at the upper detector) at synchronized arrival ($\tau = 0$) for bosons, fermions and non-interacting particles. **(c)** Expected course of P_{11} as a function of the delay τ for fermions (red) and bosons (blue).

In the case of boson bunching effect, the probability of coincidental counts P_{11}, *i.e.* one particle at each detector, would be 0. Antibunching between degenerated fermions in contrast always exhibits simultaneous counts $P_{11} = 1$. Figure 5.2b summarizes the output probabilities P_{20}, P_{11} and P_{02} at $\tau = 0$ for bosons, fermions and non-interacting particles (classical).

As we change the wavepackets' overlap via τ, P_{11} converges gradually to the Poissonian distribution as depicted in Fig. 5.2c. The width of the distinct peak results from the convolution of the wavefunctions. In the original work by Hong, Ou and Mandel [HOM87], the authors employed this feature to measure for the first time the width of a photon wavepacket with *picosecond* resolution. On the other hand, the height of the HOM peak allows to classify the quantum nature of the colliding particles as well as to quantify the degree of indistinguishability between the incident wavepackets. Owing to such correlations, HOM interference is commonly used to demonstrate identical coherent emissions of single photons [San02; Beu06].

The HOM interferometer has also been employed to study electron-electron interactions in solid-state devices. In the pioneering experiment, Liu *et al.* [Liu98] employed a thin surface-gate on a GaAs/AlGaAs heterostructure to define an

electronic beam splitter. By sending a continuous stream of electrons from two input ports, the authors observed a reduction in the current noise at the outputs. This signature of electron antibunching was attributed to the exchange interaction, *i.e.* Pauli exclusion. Later on, such an electron-electron repulsion has also been witnessed with two independent sources in the quantum-Hall regime, demonstrating quantum orbital entanglement [Ned07]. The development of the mesoscopic capacitor [Boc13] and the leviton source [Dub13] further enabled the observation of this fermionic antibunching effect at the single-particle level.

Since all these experiments were based on noise correlations, *i.e.* statistical measurements, the next step is to perform the electron-collision experiments with single-shot detection. Due to the present lack of single-electron detectors in these platforms, this implementation is however so far missing.

Another important discussion concerns the origin of the reported electron-electron antibunching. In all the aforementioned experiments, it was assumed a negligible Coulomb interaction attributed to screening effects. Therefore, Pauli exclusion was considered to be the dominant repulsion mechanism.

Here, we address this question by using our electronic circuit of coupled quantum rails as a HOM interferometer. Our highly-efficient single-electron sources and detectors allow us to perform the collision experiment with single-shot events. To witness the interplay of flying electrons, we first calibrate the coupling region such that it partitions equally a single electron sent from the upper or lower source. Employing a triggered-sending process, we control the synchronization between the electrons, allowing us to contrast the full-counting statistics from single-shot measurements with and without interaction. Comparing our experimental results to numerical simulations, we identify the major cause of in-flight interaction and assess its applicability for orbit entanglement.

The experiments presented in this chapter [Wan22a] are performed in Néel Institute (CNRS, Grenoble). The Coulomb-based model is proposed by Xavier Waintal from PHELIQS (CEA, Grenoble) whereas the SAW-confinement model is developed by Wanki Park and Prof. Heung-Sun Sim from Korea Advanced Institute of Science and Technology (KAIST, Daejeon).

5.1 HOM setup with SAW-driven nanocircuit

We aim at investigating the electron-electron interaction of a SAW-assisted flying electron pair. For this purpose, we prepare our circuit of coupled quantum rails as a HOM interferometer as shown in Fig. 5.3. A pair of electrons is synchronously transported from each source QD towards the tunnel-coupled wire. To realize the electronic version of the optical beam splitter, we control the potential profile in the coupling region via surface-gate voltages. Performing single-shot measure-

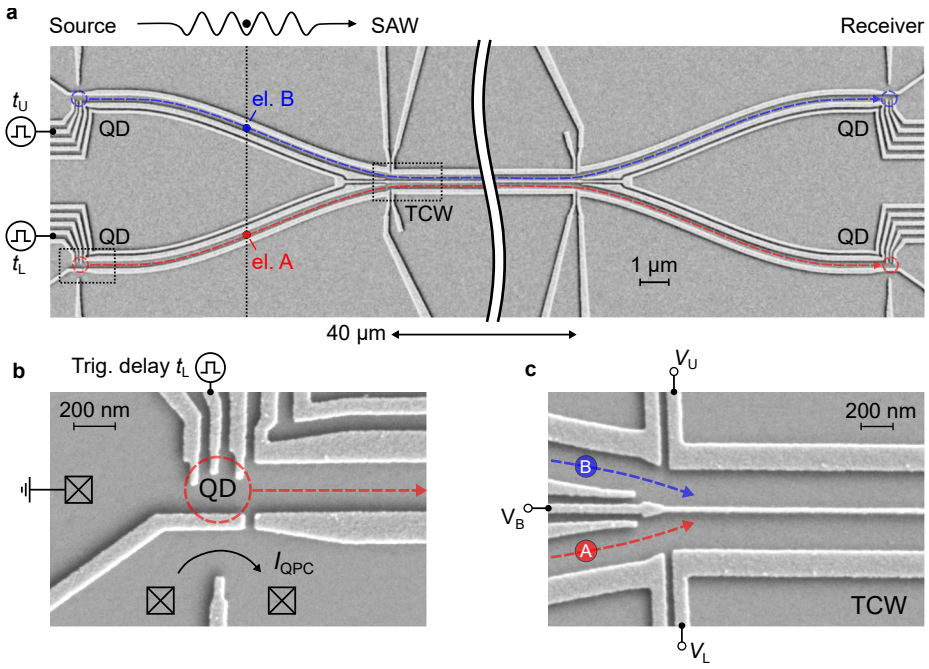

Figure 5.3: Experimental HOM setup. (a) SEM image of the sound-driven electronic circuit of coupled quantum rails. A pair of single electrons (points; A and B) is transferred via a SAW train between distant quantum dots (QDs) along two quantum rails (dashed lines). The sending process is triggered in the upper (lower) QD via a voltage pulse with time delay t_U (t_L). Along a length of 40 µm (center cropped), the two rails form a tunnel-coupled wire (TCW) where they are only separated by a narrow barrier gate. **(b)** Zoom-in of the lower source QD with indication of the electron trajectory (dashed arrow), the electrometer-current (back arrow) through the close-by quantum point contact (QPC) and the voltage-pulse trigger of the sending process (with time delay t_L). The crossed boxes indicate Ohmic contacts of the two-dimensional electron gas. **(c)** SEM image of the TCW entrance with schematic indications of the electron trajectories (dashed lines). The central control parameters are the voltages on the side gates (V_U and V_L) and the tunnel barrier (V_B).

ments with the two detector QDs, we then evaluate the probability of coincidental counts.

A key requirement to achieve such interaction of the electron pair is to synchronize the sending process at the two source QDs. For this purpose, we send a picosecond voltage pulse on the plunger gate of the respective source QD such that we trigger SAW-driven electron transport on demand [Tak19] (for details, see Section 4.6). In order to characterize the efficiency of this triggering approach, we tune the voltages on the surface gates such that the SAW transports an electron only along a single quantum rail. Sweeping the delay of the sending-trigger pulse with respect to the arrival time of the SAW, we observe distinct peaks in transfer

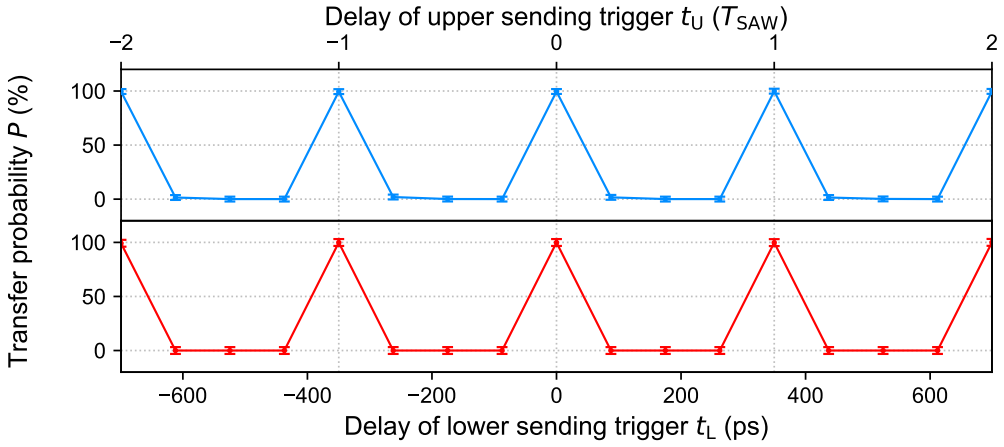

Figure 5.4: Delay-controlled sending process. Measurements of the probability, P, of single-electron transport along the upper (lower) quantum rail for different values of the sending-trigger delay t_U (t_L) at the respective source QD. The duration of the trigger pulse is $T_{SAW}/4 \approx 90$ ps. Here, the employed SAW input power is $P \approx 28$ dBm.

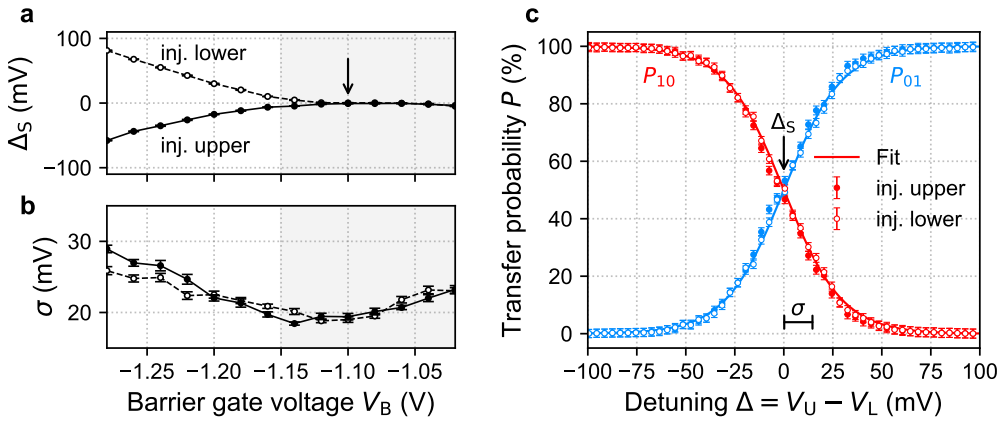

Figure 5.5: In-flight partitioning. Influence of the barrier gate voltage V_B on **(a)** the half-transmission detuning Δ_S and **(b)** the transition width σ of the in-flight-partitioning data of a single electron from the upper (point; solid line) and lower (circle; dashed line) source QD. **(c)** Probability, P, to end up in the upper (01) or lower (10) quantum rail for different values of potential detuning Δ for triggered SAW-driven emission from the upper (points) and lower (circles) source QD. The lines show a fit by a Fermi function (see equation 24) with indications on Δ_S and σ. Here, the barrier voltage is set to $V_B = -1.10$ V, and $V_U = V_L = -1.00$ V at Δ_S (see arrow in (a)).

probability as shown in Fig. 5.4. The spacing of the peaks coincides with the SAW period T_{SAW} what indicates that we are able to address a specific minimum of the SAW train to transport the electron. Owing to the large contrast in the triggered-transport efficiencies, both single-electron sources can be synchronized with a fidelity above 99 %.

Let us now lower the barrier potential of the tunnel-coupled wire (TCW) to allow the electron to transit into the opposite quantum rail. To maximize the visibility of interaction effects, the coupling region needs to be calibrated to partition equally an electron sent from the upper or lower source QD. For this purpose, we investigate the evolution of the half-transmission detuning Δ_{S} and the transition width σ extracted from single-electron partitioning data as a function of the barrier gate voltage V_{B} (see Fig. 5.5a,b). For a high barrier ($V_{\mathrm{B}} < -1.15$ V), an asymmetric polarization of the channel gates ($\Delta_{\mathrm{S}} \neq 0$) is required to achieve 50 % transmission. Comparing in-flight partitioning data from an individual electron injected from each source QD, we observe that Δ_{S} converges gradually to a matching value $\Delta_{\mathrm{S}} = 0$ when V_{B} becomes more positive. Both transition widths σ are similar and independent on the injection side. Since σ is related to the energy state of the partitioned electron, we find a minimal excitation for V_{B} between ≈ -1.15 V and -1.05 V.

An example of equal partitioning is shown in Fig. 5.5c. The transmission probabilities correspond to data at $V_{\mathrm{B}} = -1.10$ V for an electron sent from the upper and the lower source QD. The maximal overlap is reflected in the identical Δ_{S} and σ. At this barrier condition, the flying electrons experience symmetric transmission in the coupling region independent on the injection side.

To prepare the collision experiment, we keep the barrier potential such that the partitioning of each flying electron is 50 %. Employing the delays, t_{U} and t_{L}, of the sending triggers of the upper and lower source QDs, we control the timing of transport along the two quantum rails as sketched in Fig. 5.6a. For this purpose, we fix the delay of the upper electron ($t_{\mathrm{U}} = 0$) and step the delay for the lower electron in multiples of the SAW period ($t_{\mathrm{L}} = k \cdot T_{\mathrm{SAW}}$ where $k \in \mathbb{Z}$) in order to address different SAW minima for transport. If the electrons tunnel without experiencing the presence of the other, we expect 50 % probability (P_{11}) to find one electron in the upper and one electron in the lower detector. Figure 5.6b shows a corresponding measurement of the antibunching probability P_{11} as function of the trigger delay t_{L} of the electron sent from the lower source QD. We find $P_{11} \approx 50$ % as expected when the two electrons are transported in different SAW minima.

As the sending triggers are synchronized and the two electrons are sent within the same SAW minimum, we observe a significant increase of $P_{11} \approx 80$ %. We interpret this increment as consequence of the repulsive interaction of the electron pair. The distinct P_{11} peak underpins our expectation that the flying electrons

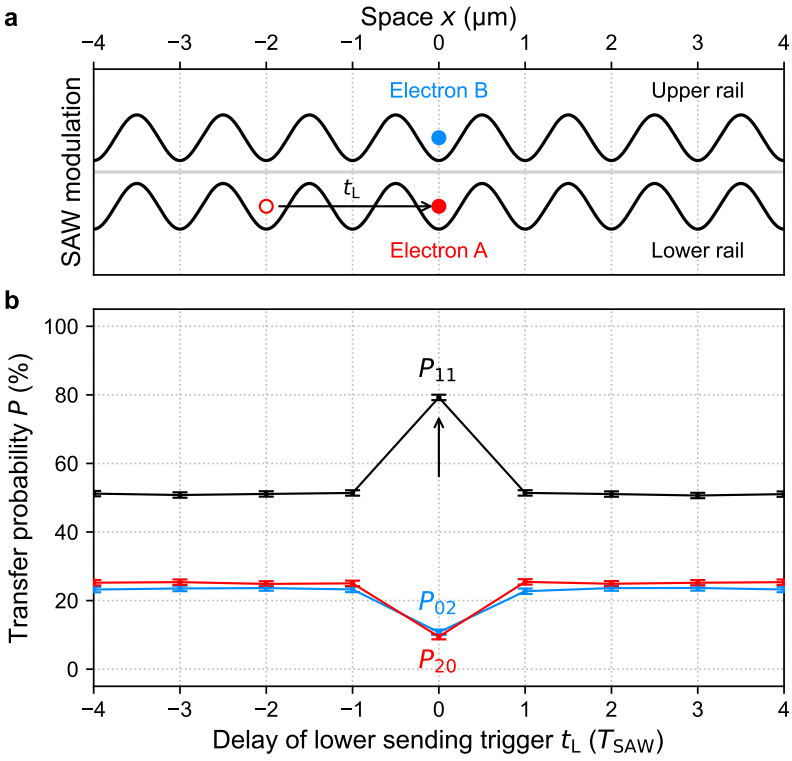

Figure 5.6: Antibunching at synchronized transport. (a) Schematic of the measurement. The delay $t_U = 0$ of the upper sending trigger (for electron B) is kept fixed while the delay t_L of the lower sending trigger (for electron A) is set to successive potential minima of the SAW-train. **(b)** Measurements of single-shot probabilities for P_{20} (both electrons at lower detector), P_{11} (one electron at upper and lower detector) and P_{02} (both electrons at upper detector) as function of the delay t_L of electron B. Here the voltage configuration of the TCW is $V_B = -1.15$ V and $V_U = V_L = -1.00$ V. The arrow indicates the synchronized condition.

remain within the initially addressed SAW minimum during transport. Furthermore, over a distance of one SAW period ($\approx$ 1 µm), the data indicates that – within the error range – the interaction of the electron pair gets negligible.

5.2 Partitioning of an electron pair

In order to investigate the nature of the repulsive effect – Coulomb interaction or Pauli exclusion –, we perform the collision experiment as we detune the potential landscape. As reference, let us first focus on the non-interacting case ($t_U - t_L = 5 \cdot T_{SAW}$) as shown in Fig. 5.7a by the semi-transparent data. This case is a direct consequence of the in-flight-partitioning distribution of the individual

electrons. Since the electrons do not interact, the scattering statistics follow a Poisson binomial distribution. Therefore, the probability to find both electrons in the lower channel is simply the product of the single-electron cases,

$$P_{20} = P_{10}^{\mathrm{A}} \cdot P_{10}^{\mathrm{B}}, \tag{32}$$

for injection from the lower (electron A) and upper (electron B) source QD. Accordingly, we obtain

$$P_{02} = P_{01}^{\mathrm{A}} \cdot P_{01}^{\mathrm{B}} \tag{33}$$

$$P_{11} = P_{10}^{\mathrm{A}} \cdot P_{01}^{\mathrm{B}} + P_{01}^{\mathrm{A}} \cdot P_{10}^{\mathrm{B}} = 1 - P_{20} - P_{02}. \tag{34}$$

Using now the single-electron partitioning data as shown in Fig. 5.5c, we evaluate the transfer probabilities expected from this non-interacting model (see semi-transparent lines in Fig. 5.7a). The simulated course shows good agreement with the experimental data when the two electrons are sent in different SAW minima.

As we send the two electrons synchronously with the same SAW minimum ($t_{\mathrm{U}} - t_{\mathrm{L}} = 0$; non-transparent data), we observe a change in the functional course of P_{20} and P_{02} leading to a significant increase and broadening of $P_{11}(\Delta)$ compared to the non-interacting case. This contrast suggests that the electron-electron interaction is still present for a wide range of potential detuning.

Which physical effect causes the observed in-flight partitioning of the two interacting electrons? To answer this question, let us focus on the Coulomb potential that is experienced by one electron due to the presence of the other. We perform three-dimensional potential simulations taking into account the geometry and electronic properties of the presently investigated nanoscale device (for details about the electrostatic model, see Section 2.3). In order to emulate the presence of an electron in one side of the rail, we introduce the density of one elementary charge in a volume of $\Delta x = 150$ nm, $\Delta y = 17$ nm and $\Delta z = 1$ nm, where x (y) is parallel (perpendicular) to the SAW propagation direction, and z is the growth direction of the heterostructure. Δx was chosen from the characterized SAW amplitude (see Fig. 4.8c in Section 4.4) while Δy was extracted from the simulated width of a wavepacket in the double-well potential (see Fig. 4.15 in Section 4.8).

For the sake of simplicity, we consider the symmetric configuration of the surface gates at $\Delta = 0$ ($V_{\mathrm{B}} = -1.15$ V and $V_{\mathrm{U}} = V_{\mathrm{L}} = -1.00$ V). Figure 5.7b shows the result of a potential simulation (dotted line) by adding the density of an electron-charge in the upper or lower rail. The simulation shows that electron A experiences a potential landscape that is effectively detuned due to the presence of electron B, and *vice versa*. We find a potential difference of $\Delta U \approx 3.7$ meV

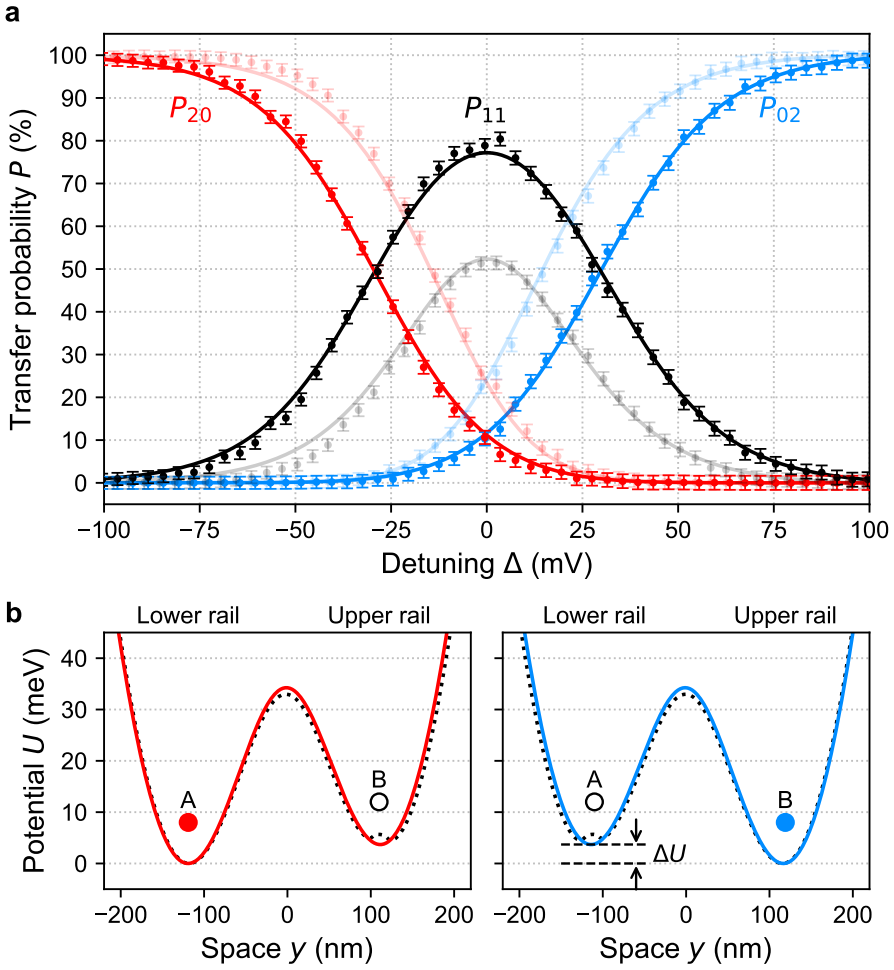

Figure 5.7: Coulomb induced detuning and electron-pair partitioning. (a) Measurements of single-shot probabilities for P_{20}, P_{11} and P_{02} for transfer of the electron pair in the same ($t_U - t_L = 0$; solid line) and different ($t_U - t_L = 5 \cdot T_{SAW}$; semi-transparent line) potential minima accompanying the SAW train. The solid lines show the results of models of electron in-flight partitioning with and without Coulomb interaction (see Section 5.3). At $\Delta = 0$, the TCW is defined by $V_B = -1.15$ V and $V_U = V_L = -1.00$ V. **(b)** Detuned potential landscapes observed by one electron (filled point) due to the presence of another electron (circle). The dashed line in the left (right) plot shows the result of a potential simulation of the symmetrically polarized TCW with an electron inserted in the upper (lower) coupled transport channel. The solid line shows an equivalent potential formed by an voltage detuning of $\delta = V_U - V_L \approx \mp 18.5$ mV, which results in a potential difference $\Delta U \approx 3.7$ meV.

between the bottom of the two channels that is equivalent to a voltage detuning on the surface gates by $\Delta \approx \delta = 18.5 \pm 0.4$ mV – as shown by the solid lines in Fig. 5.7b. These numerical results suggest that the presence of one electron is equivalent to an effective voltage detuning.

How does this potential detuning quantitatively affect the antibunching rate? In the next section, we express such a mutual influence in terms of conditional probabilities, and employ the Bayes theorem to evaluate the transmission probabilities in the two-electron partitioning process.

5.3 Bayesian model of in-flight partitioning

In the following we employ Bayesian probability calculus to derive the in-flight probabilities P_{20}, P_{11} and P_{02} from the single-electron-partitioning data P_{10} and P_{01}. We consider that the presence of one electron induces a potential change that is equivalent to an effective voltage detuning δ for another electron in the opposite quantum rail. To begin, let us clarify the used notations: we consider two quantum rails, L (lower) and U (upper) in which we synchronously send two electrons, A and B. In the case that only A is transferred, there is a probability $P(\mathrm{A_L}) = P_{10}^{\mathrm{A}}$ that electron A stays in L after transport due to in-flight partitioning in the tunnel-coupled region. Accordingly, the probability of A to end up in U is $P(\mathrm{A_U}) = P_{01}^{\mathrm{A}} = 1 - P_{10}^{\mathrm{A}}$.

In the case of sending two electrons, we can define the probability to find both electrons in L via the joined probability

$$P_{20} = P(\mathrm{A_L}|\mathrm{B_L}) \cdot P(\mathrm{B_L}) \tag{35}$$

where $P(\mathrm{A_L}|\mathrm{B_L})$ is the conditional probability to find A in L when B is present in L, and $P(\mathrm{B_L})$ is the probability to find B in L independent on the location of A.

Employing the Bayes' theorem

$$P(X|Y) = \frac{P(Y|X) \cdot P(X)}{P(Y)} \tag{36}$$

for $P(\mathrm{A_L}|\mathrm{B_L})$ and $P(\mathrm{A_L}|\mathrm{B_U})$, we derive $P(\mathrm{B_L})$ – knowing that $P(\mathrm{B_U}) = 1 - P(\mathrm{B_L})$ – as:

$$P(\mathrm{B_L}) = \frac{P(\mathrm{A_L}|\mathrm{B_U}) \cdot P(\mathrm{B_L}|\mathrm{A_L})}{P(\mathrm{A_L}|\mathrm{B_U}) \cdot P(\mathrm{B_L}|\mathrm{A_L}) + P(\mathrm{B_U}|\mathrm{A_L}) \cdot P(\mathrm{A_L}|\mathrm{B_L})} \tag{37}$$

Note that here $P(\mathrm{B_L})$ does not need to be equivalent to the single-electron case P_{10}^{B} due to the mutual influence between the electrons.

Let us first focus on the non-interacting case where the two electrons do not influence each other. For two independent events, the conditional probability

satisfies $P(X|Y) = P(X)$. Applying this relation to equation 35 and 37, we obtain

$$P_{20} = P_{10}^{\mathrm{A}} \cdot P_{10}^{\mathrm{B}} \tag{38}$$

that follows the Poisson binomial distribution.

In the interacting case, the presence of electron B influences A, and *vice versa*. For the presently studied experimental configuration, our potential simulations indicate that the Coulomb potential of B effectively detunes the potential landscape that is observed by A. The effect is equivalent to an effective voltage detuning δ on the surface gates. Including this Coulomb interaction, we find:

$$P(\mathrm{A_L}|\mathrm{B_U}) = 1 - P(\mathrm{A_U}|\mathrm{B_U}) = P_{10}^{\mathrm{A}}(\Delta - \delta) \tag{39}$$

$$P(\mathrm{A_L}|\mathrm{B_L}) = 1 - P(\mathrm{A_U}|\mathrm{B_L}) = P_{10}^{\mathrm{A}}(\Delta + \delta) \tag{40}$$

Similarly, the influence of A on B is defined as

$$P(\mathrm{B_L}|\mathrm{A_U}) = 1 - P(\mathrm{B_U}|\mathrm{A_U}) = P_{10}^{\mathrm{B}}(\Delta - \delta) \tag{41}$$

$$P(\mathrm{B_L}|\mathrm{A_L}) = 1 - P(\mathrm{B_U}|\mathrm{A_L}) = P_{10}^{\mathrm{B}}(\Delta + \delta) \tag{42}$$

Substituting these expressions in equation 35 and 37, we obtain the joined probability

$$P_{20}(\Delta) = \frac{P_{10}^{\mathrm{A}}(\Delta+\delta) \cdot P_{10}^{\mathrm{A}}(\Delta-\delta)}{\frac{P_{10}^{\mathrm{A}}(\Delta+\delta)}{P_{10}^{\mathrm{B}}(\Delta+\delta)} + P_{10}^{\mathrm{A}}(\Delta-\delta) - P_{10}^{\mathrm{A}}(\Delta+\delta)}. \tag{43}$$

Following the same procedure, we can construct P_{02} and P_{11} from

$$P_{02} = P(\mathrm{A_U}|\mathrm{B_U}) \cdot P(\mathrm{B_U}) \tag{44}$$

$$P_{11} = 1 - P_{20} - P_{02}. \tag{45}$$

Let us now apply this model to the partitioning data for a pair of synchronized flying electrons. The solid lines shown in Fig. 5.7a indicate the courses of P_{20}, P_{02} and P_{11} resulting from equations 43, 44 and 45 with $\delta = 18.5$ mV extracted from the 3D potential simulation. We note that no fitting parameter is used. The excellent agreement of the Bayesian model with the experimental data suggests Coulomb interaction of the flying electron pair as major source of the increased antibunching probability.

The agreement between the model and the partitioning data allows us to address the following question: what is the limiting factor to have 100 % antibunching probability? For this purpose, we present in the following a predictive investigation of the Coulomb-related antibunching rate by evaluating the Bayesian model assuming reduced excitation of the flying electrons. Figure 5.8a shows the maximum P_{11} as a function of the single-electron partitioning width

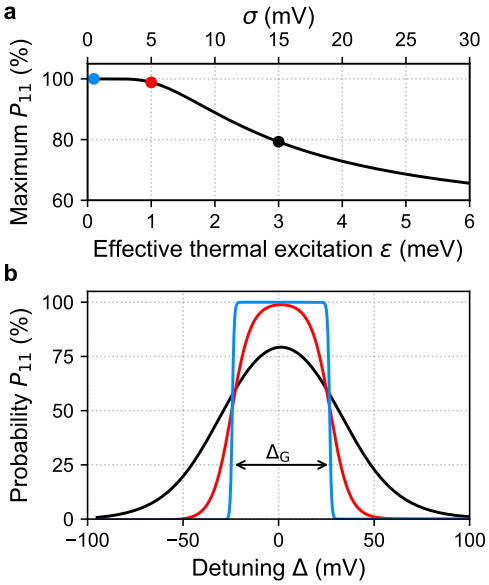

Figure 5.8: Role of the effective thermal excitation. (a) Simulations based on the Bayesian model of the maximum antibunching probability P_{11} as a function of the effective thermal excitation ε of both single electrons. Here, we employed the extracted induced detuning $\delta \approx 18.5$ mV for $V_B = -1.15$ V. For the current experimental condition ($\varepsilon = 3$ meV; black point), $P_{11} \approx 80$ %. The threshold of $P_{11} = 99$ % is reached at $\varepsilon = 1$ meV (red point). **(b)** Evolution of P_{11} as a function of Δ for different $\varepsilon \in [0.1, 1.0, 3.0]$ meV (blue, red and black, respectively). When the electron A and B are in the ground state, P_{11} has a detuning width $\Delta_G = 2\delta + |(\Delta_S^A - \Delta_S^B)|$ (double-headed arrow).

σ. We express σ as an effective thermal excitation $\varepsilon = \alpha \cdot \sigma$ where the gate-alpha factor $\alpha = 1/5$ is extracted from a fit by assuming an exponential distribution [Tak19][1]. We find that by reducing the current excitation ε by a factor of 3, the antibunching rate P_{11} would be beyond 99 %. These simulations suggest that, in our current experimental condition, the flying electrons still have some probability to overcome the Coulomb repulsion due to excitation. Comparing the simulated course of P_{11} – see Fig. 5.8b –, we expect a narrowing of the distribution for smaller excitation. The saturation to 100 % represents the condition where the Coulomb-mediated antibunching is robust against small variations in the gate detuning Δ.

5.4 Effect of barrier height on antibunching rate

Having identified the Coulomb interaction as the main cause of antibunching for a specific configuration, next we check whether this assertion also holds when the barrier potential is changed. For this purpose, we investigate the antibunching probability P_{11} at a symmetric detuning ($\Delta = 0$) as a function of the barrier-gate voltage V_B (see Fig. 5.9a). Let us first focus on the high barrier regime ($V_B < -1.15$ V). As the barrier height becomes larger for the non-interacting case (semi-transparent data; reference), the transmission of each electron to the opposite channel is reduced leading to a gradual increase of P_{11} up to 100 %.

[1]Note that this value is consistent with the ratio between the effective voltage detuning $\delta = 18.5$ mV and the induced potential difference 3.7 meV, which also results in $\alpha = 1/5$.

We observe a similar increase of P_{11} in this regime when the electron pair is transported synchronously (black data). The excess probability ΔP_{11} shown in Fig. 5.9b indicates that the electron-electron interaction is also present even when both rails are almost fully separated.

For lower barrier heights ($V_B \geq -1.15$ V; grey area), the antibunching probability P_{11} (with synchronization) changes while the reference data (without sync.) is saturated at ≈ 50 %. We observe that the antibunching rate expressed as ΔP_{11} decreases linearly as a function of V_B. Naively, one might expect that a reduced barrier brings the electrons closer, and hence the Coulomb-interaction increases. So why does the antibunching rate decrease as we lower the barrier height and not *vice versa*? A possible explanation is the weakening of the Coulomb blockade

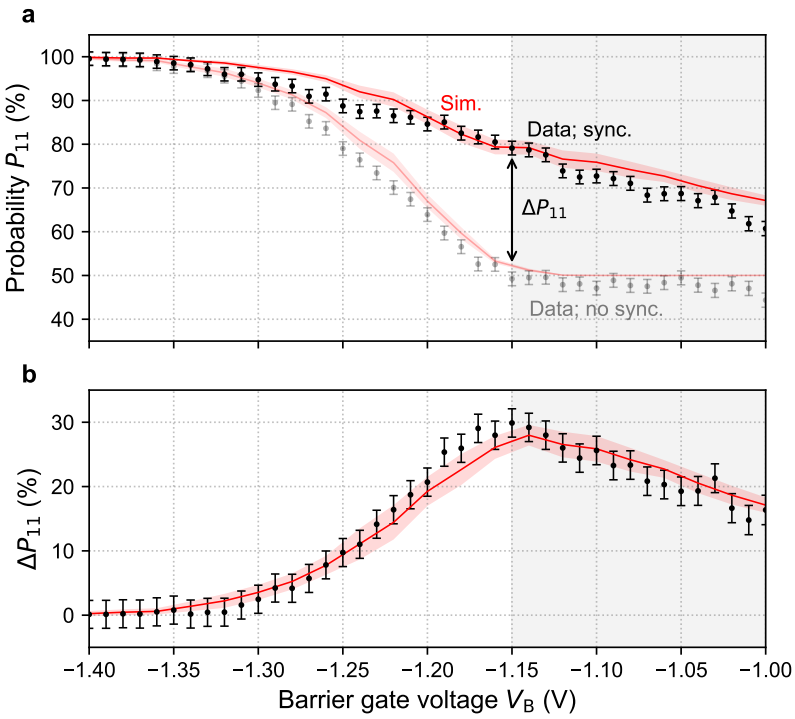

Figure 5.9: Barrier dependence of antibunching rate. Probability P_{11} as function of the voltage V_B applied on the barrier gate. The red line shows the course of the Bayesian model based on potential simulation for the respective barrier potentials. The error (semi-transparent area; standard deviation of 5σ) stems from the deduction of the Coulomb-equivalent detuning δ from experimental data. **(b)** Excess in antibunching rate due to Coulomb-repulsion, here expressed by ΔP_{11} that is the difference of P_{11} for transport in the same (synchronized) and different (no sync.) SAW minima. The shaded region highlights the regime where P_{11} of the non-interacting case is saturated at ≈ 50 %.

between the pair of moving QDs. The barrier affects slightly the charging energy of each propagating QD, but most importantly it controls the tunneling rate and thus the probability of hopping events between the quantum rails. If the charging energy E_C is lower than the excited energy ε of the electron, a reduced tunneling resistance would facilitate exchange overcoming Coulomb blockade.

Let us now apply the Coulomb-based Bayesian model for this dataset. To extract accurately the effective detuning δ, we employ the model to fit two-electron partitioning data for several gate voltages in the low barrier regime ($V_B \geq -1.15$ V). We find that – see Appendix D.2 – δ decreases linearly as V_B becomes more positive. Considering this linear course in the Bayesian model, we simulate the maximum antibunching probability P_{11} as a function of V_B (red line in Fig. 5.9). The excellent agreement between the model and the experimental data indicates that Coulomb interaction is also dominant for a wider range of barrier-gate voltages.

5.5 The role of SAW confinement

Having confirmed the influence of the barrier height on the Coulomb interaction, we now investigate the longitudinal confinement of a moving QD via the SAW amplitude. Figure 5.10a shows the excess in antibunching probability ΔP_{11} as a function of the applied RF power P on the transducer extracted from the two-electron partitioning data – see Appendix D.3. We observe two regimes distinguished by a change in the slope around $P \approx 24.5$ dBm. From the SAW amplitude calibration – see Fig. 4.8c in Section 4.4 –, we know that the SAW confinement is not strong enough to avoid electron tunneling to subsequent minima below this value. For the region above the 95 % threshold for in-flight confinement [Edl21], ΔP_{11} gradually increases with SAW power. A possible explanation is that, as P increases, the charging energy within each moving QD becomes larger, and thus overcoming the effective thermal excitation of the electrons.

To get a better understanding, we use the Bayesian model and extract the potential detuning δ as shown in Fig. 5.10b. We observe that the course of δ is similar to P_{11}. From previous investigations, we know that δ also depends on the barrier height via V_B. While V_B controls mainly the coupling between the quantum rails that could affect the inter-dot energy E_{inter}, P changes the confinement potential within each moving QD, *i.e.* intra-dot energy E_{intra}. These results suggest that δ is a balance between E_{inter} and E_{intra}.

To check whether this hypothesis is valid, let us assume that the effective detuning is

$$\delta = \frac{|E_{\text{intra}} - E_{\text{inter}}|}{\alpha} \tag{46}$$

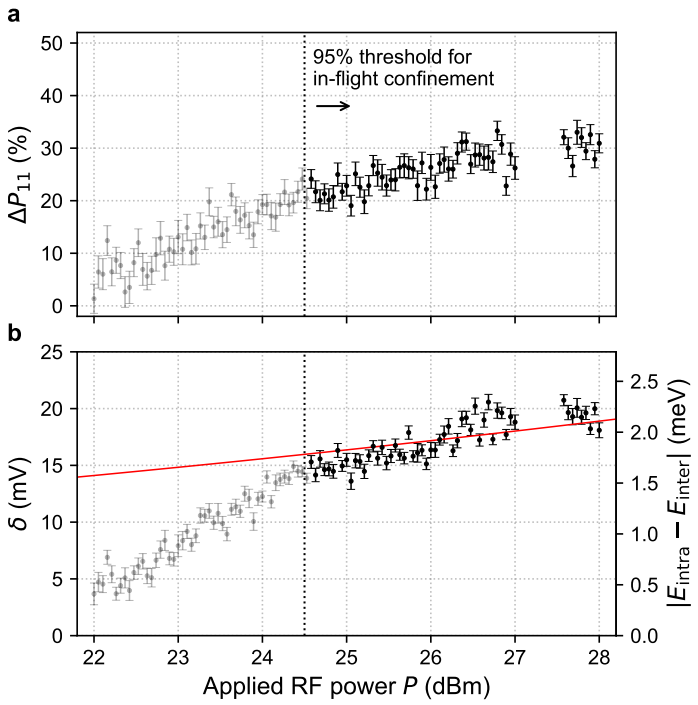

Figure 5.10: SAW confinement. **(a)** Antibunching rate ΔP_{11} subtracted from two-electron-partitioning data with and without synchronized sending. The missing data points around 27 dBm are due to technical problems during the measurements. **(b)** Extracted δ from a fit using the Bayesian model of two-electron-partitioning data at each applied power. The expected evolution (red line) above the 95 % confinement threshold is calculated by approximating the SAW potential to a parabolic QD. For details, see Appendix D.3.

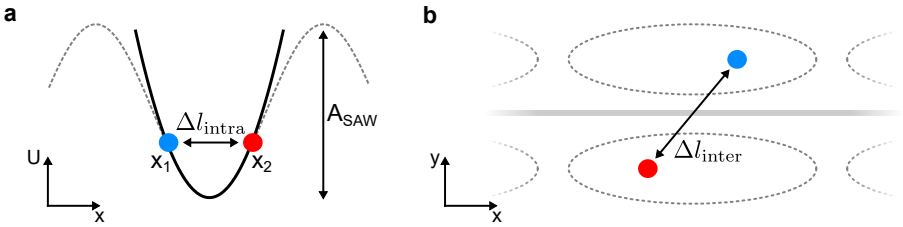

Figure 5.11: Schematic of electron-pair locations. **(a)** SAW confinement potential (dashed grey line) along the propagation direction x with peak-to-peak amplitude A_{SAW}. The parabolic approximation is depicted on top (black line). The electrons (blue and red) at positions x_1 and x_2 are separated by $\Delta l_{\mathrm{intra}} = |x_2 - x_1|$. **(b)** Schematic top view in the coupling region where the pair of electrons are located at different moving QDs (dashed circles). The inter-dot separation $\Delta l_{\mathrm{inter}}$ is indicated by the double-headed arrow.

with α as the conversion factor from V to eV. In order to estimate E_{intra}, we approximate the confinement along the SAW propagation direction x to a parabolic potential as depicted in Fig. 5.11a. The energy of the system can be defined as

$$E_{\text{intra}} = \frac{1}{2} m_e \omega_x^2 (x_1^2 + x_2^2) + E_{\text{C}} \tag{47}$$

where E_{C} corresponds to the unscreened Coulomb energy

$$E_{\text{C}} = \frac{\beta}{|x_1 - x_2|} \tag{48}$$

Here, $\beta = \frac{e^2}{4\pi\varepsilon_r\varepsilon_0} \approx 111.6$ meV/nm is the Coulomb repulsion constant, e is the elementary charge, ε_0 is the vacuum permitivity, $\varepsilon_r \approx 12.88$ is the dielectric constant of GaAs, $m_e \approx 0.067 \cdot m_0$ denotes for the electron effective mass in GaAs, ω_x is the parabolic confinement frequency and x_i is the position of the electron i. Expressing equation 47 in terms of the intra-dot separation $\Delta l_{\text{intra}} = |x_1 - x_2|$, we find via $\delta E_{\text{intra}}/\delta \Delta l_{\text{intra}} = 0$ that the lowest energy of the system is

$$E_{\text{intra}} = \frac{3}{2^{\frac{4}{3}}} \left(m_e \omega_x^2 \beta^2\right)^{\frac{1}{3}} \tag{49}$$

at the optimum distance of

$$\Delta l_{\text{intra}} = \left(\frac{2\beta}{m_e \omega_x^2}\right)^{\frac{1}{3}}. \tag{50}$$

If only few electrons are present, the ground state of the system found via this classical approach is equivalent to solving the quantum Hamiltonian [Cif09].

The confinement frequency ω_x is determined by the SAW amplitude. The periodic acoustic potential is defined as

$$U_{\text{SAW}} = \frac{A_{\text{SAW}}}{2} \sin\left(2\pi \frac{x - v_{\text{SAW}} t}{\lambda}\right) \tag{51}$$

where v_{SAW} is the SAW velocity in GaAs and λ is the wavelength determined by the transducer periodicity. Note that the SAW peak-to-peak amplitude A_{SAW} depends exponentially on the input power P according to equation 23. Using the parabolic potential $U_{\text{SAW}} = \frac{1}{2} m_e \omega_x^2 x^2$ and equation 51 at the local minimum $x = \lambda/\pi$, we find

$$\omega_x(P) = \left(\frac{\pi}{\lambda}\right) \left(\frac{2}{m_e}\right)^{\frac{1}{2}} \left(A_0 10^{\frac{P}{20}}\right)^{\frac{1}{2}} \tag{52}$$

where $A_0 \approx 1.7$ meV is the peak-to-peak amplitude at $P = 0$ dBm. Substituting the above expression in equation 47, we reach to the final relation

$$E_{\text{intra}}(P) = \frac{3}{2} \left(\frac{\pi\beta}{\lambda}\right)^{\frac{2}{3}} \left(A_0 10^{\frac{P}{20}}\right)^{\frac{1}{3}}. \tag{53}$$

For the maximum applied power $P = 28$ dBm, two electrons occupying the same moving QD would be separated by $\Delta l_{\text{intra}} \approx 65$ nm which results in $E_{\text{intra}} \approx 2.6$ meV. We find that this value is consistent with the typical charging energy ≈ 1 meV of a lateral QD in GaAs.

Let us now estimate E_{inter} via the inter-dot distance Δl_{inter} as depicted in Fig. 5.11b. In the limiting case of unscreened Coulomb repulsion, the energy is simply

$$E_{\text{inter}} = \frac{\beta}{\Delta l_{\text{inter}}}. \tag{54}$$

Since the co-propagating electrons have a separation $\Delta l_{\text{inter}} \approx 230$ nm, we estimate $E_{\text{inter}} \approx 0.5$ meV. Note that owing to $E_{\text{inter}} < E_{\text{intra}}$, the electron pair tends to occupy different moving QDs, and hence the observation of the Coulomb-induced antibunching effect.

Having expressed δ as a function of the input SAW power P, we employ the equations 46 and 53 to reproduce the experimental data shown in Fig. 5.10b where α is the only fitting parameter. Using $\alpha \approx 1/9$ eV/V, our estimation (red line) shows a good agreement with the extracted detuning δ. These results confirm our expectation that the SAW amplitude modifies the intra-dot energy.

5.6 An electron pair in a single SAW minimum

The HOM setup can quantify the degree of distinguishability of the colliding electrons. If Pauli exclusion is the main cause of antibunching, electrons with different energies would cause a reduction in the HOM peak. A convenient way to check this is to load two electrons in the same source dot and exploit the charging energy within the QD to prepare distinguishable particles. We then trigger the sending process to synchronize the electron pair as done in previous experiments.

Figure 5.12a shows the partitioning data for two synchronized electrons sent from the same (solid) and different (semi-transparent; reference) source QDs. The enhanced P_{11} underpins our expectation that the electron pair is confined together during transport. We observe a similar behavior in the course of P_{11} with a small reduction of 2.8 ± 0.8 % in the antibunching peak. From calibration measurements where no trigger pulse is applied, we find this reduction is caused by the electron-pair holding error ≈ 3 % in the upper source. To further verify that both cases are equivalent, we compare the dependency of the antibunching probability on the barrier gate voltage V_{B} as shown in Fig. 5.12b. As the barrier increases, two electrons sent from a common source tend to remain in the injected quantum rail as expected. For the low-barrier regime ($V_{\text{B}} > -1.20$ V), the data shows identical P_{11} for a wide range of V_{B}. Owing to these similarities, we observe

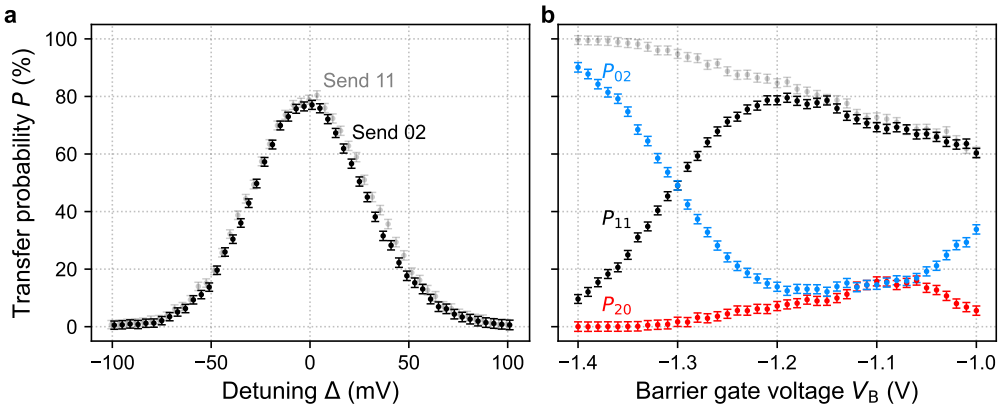

Figure 5.12: Electron-pair partitioning from a common source. **(a)** Antibunching probability P_{11} from the in-flight partitioning of an electron pair from the same (send 02; solid) and different (send 11; semi-transparent) source QDs, with maximum at 76.8 ± 0.5 % and 79.6 ± 0.3 %, respectively. **(b)** Probabilities P_{20}, P_{11} and P_{02} as a function of the voltage V_B on the barrier gate.

no signature of Pauli exclusion[2].

Although the experiment does not yield to different results, we cannot conclude that only Coulomb interaction is present. A possible scenario is that, first, the high-energy electron tunnels to the other quantum rail at the TCW entrance. Since the flight time in the coupling region is ≈ 14 ns, relaxation could recover the indistinguishability between the electrons. Note that the electron spin should be random since no magnetic field is applied. Therefore, it is still possible that Pauli exclusion could be manifested in a short period of interaction time.

In order to investigate this hypothesis, it is necessary to perform *time-resolved* manipulations during the flight of the electrons. In the next chapter, we will show our initial efforts towards the dynamical control of the barrier height to unveil the quantum state evolution in the coupling region.

5.7 Estimation of Coulomb-induced phase shift

A relevant application of the long-range Coulomb interaction is to realize a quantum phase gate for flying electron qubits. In order to estimate the phase shift from the observed electron-electron interaction, we first calculate the Coulomb energy and then relate it to the phase shift reported on non-chiral ballistic quantum interferometers. The potential simulations indicate a distance of 230 nm

[2]We further investigated the collision between three synchronized electrons (see in Appendix D.5), but the results are not exhaustively analyzed yet.

between the two electron propagating along the TCW giving a Coulomb energy of $E_C \approx 500$ µeV (see equation 48). From experiments with ballistic electrons[3] in a Mach-Zehnder setup [Yam12; Tak15; Edl17], a phase shift of π was observed on the electron wavefunction for a surface-gate-voltage variation of about 40 mV extending over 3 µm. Owing that similar phase rotation is achieved with a magnetic-period $\Delta B \approx 4.5$ mT, we then estimate the energy scale to introduce a π-shift as

$$E_\pi = -\frac{1}{2}\, g\, \mu_B\, \Delta B \approx 55 \text{ neV} \tag{55}$$

where $g \approx -0.425$ is the GaAs-specific g-factor and μ_B is the Bohr magneton. Since electron transport with a SAW is about 100 times slower than ballistic transport, we anticipate that a phase rotation of π is achievable on a propagation over a length-scale of 100 nm. Having demonstrated high-fidelity transport over tens of micrometers, such quantum manipulation would not be limited by the in-flight interaction time. Accordingly, we anticipate that the long-range Coulomb interaction of simultaneously transported electrons introduces a significant reciprocal phase shift entangling the orbital degree of freedom in a SAW-driven single-electron circuit.

5.8 Conclusion

Controlled Coulomb-coupling of single flying electrons is a key requirement to realize a quantum-processing unit where electron qubits are dynamically fed through a circuit of quantum-logic gates. In this context, the SAW-driven platform is an excellent candidate as testbed to investigate the in-flight interaction.

Here we have implemented the HOM interferometer with a circuit of coupled quantum rails at the single-electron level. Using a tunnel-coupled wire as a beam splitter, we showed our ability to have identical transmission for an electron injected from independent sources. Synchronizing the transport of two single-electrons, we were able to observe an excess in the antibunching probability up to 30 % due to electron-electron interaction. Combining precise potential simulations and the Bayes theorem, we find that the dominant mechanism is the long-range Coulomb repulsion. Investigating the influence of the moving confinement potential, we concluded that the antibunching process is present for a wide range of experimental conditions.

Finally, to investigate if this electron-electron interaction is sufficient to achieve a reciprocal phase shift of π and thus Bell-state formation, we compare the electron gating effect to previous quantum-interferometry experiments. Considering the energy scale and the interaction time, we find that such gating effect is more

[3] We note that these experiments are performed with non-depleted 2DEG, in contrary to our case.

than sufficient to induce a π-rotation in single-electron circuits based on sound. Providing evidence for a significant extent of Coulomb interaction in a tunnel-coupled wire, our results pave the way to realize two-qubit gates for single flying electrons.

CHAPTER 6

Real-time control of in-flight interaction

We have shown previously that the investigated single-electron circuit is compatible for the observation of electron-electron interaction in a setup with coupled transport rails. We found in particular that Coulomb repulsion is the dominant mechanism in SAW-assisted collision experiments. More interestingly, the strong antibunching signature ($P_{11} \approx 80$ %) was present even with a 40-µm-long coupling region (flight time ≈ 14 ns). This triggers for instance questions such as "does the electron-electron repulsion occur at a specific coupling location or over the entire length?" or "what is the minimum interaction time required for the electron partitioning process?" Ultimately, the main unknown that we want to address is: can we coherently manipulate the flying quantum state?

To investigate the in-flight dynamics of a transported electron, our strategy is to employ tailored voltage pulses with sub-nanosecond resolution to control the barrier height in *real time*. Such a time resolution is achieved in particular by combining the broadband bias tee (20 kHz to 40 GHz) connected to the tunnel-barrier gate and the cutting-edge arbitrary waveform generator (25 GHz bandwidth and up to 64 GS/s) – for details about the RF setup, see Appendix C.2.

In this chapter, we present preliminary investigations of dynamical control of the barrier height. To turn on and off the coupling between the quantum rails, we first perform calibration measurements of the barrier pulse amplitude. Employing a time-delayed voltage signal, we identify the electron arrival at the exit of the TCW. Using a synchronized pair of electrons, we investigate the required interaction time for the antibunching process.

The results presented in this chapter are from a different cool down after upgrading the RF setup. Therefore, the optimum gate voltages are slightly different than in previous experiments. In particular, we are currently using a lower SAW power of $P \approx 26$ dBm because the sample tuning for the maximum SAW power $P \approx 28$ dBm was not optimized yet. For preliminary time-resolved characterizations however, this should not be a limitation.

We would also like to emphasize that the results shown in the following sections are still under analysis. Owing to the novelty of these experiments, the data interpretation are not yet in their final stage. We note that, at the time of this writing, measurements are still being performed with the investigated sample.

6.1 Barrier pulse calibration

The first step towards time-resolved manipulations is to calibrate the pulse amplitude applied to the barrier gate. Figure 6.1a shows a SEM image of the coupling region highlighting the tunnel-barrier surface-gate (red). The bias tee allows to apply a DC bias V_B as well as a fast voltage pulse V_p to control the potential profile in the TCW.

To verify that the experimental setup is working properly, we employ a square pulse much longer than the flight-time of an electron from the source to the receiver QD ($\approx$ 22 ns; see Fig. 6.1b). We denote this as the DC limit for the RF pulse. As a reference measurement, we first set the channel-gate voltages ($V_\mathrm{U} = V_\mathrm{L} = -1.10$ V) to allow the partitioning of an electron at low barrier. We then trigger-send one electron from the lower QD and vary the static bias V_B. Figure 6.1c shows the reference probability P_{10} to catch one electron in the lower receiver QD (dotted black line; top x-axis). We observe the expected transition from two independent rails ($V_\mathrm{B} \lessapprox -1.50$ V) to a finite probability for the electron to end up in the opposite transport path.

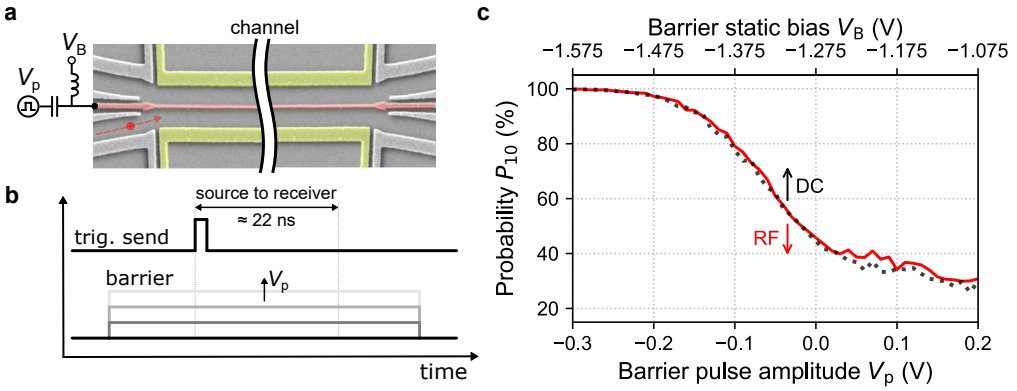

Figure 6.1: Pulse amplitude calibration. (a) SEM image of the coupling region defined by the channel gates (yellow) with indication of an electron (red) injected from the lower QD. The bias tee connected to the barrier gate (red) allows to apply a DC bias V_B and a RF voltage pulse with amplitude V_p. **(b)** Schematic of the pulse sequence for the amplitude calibration. The sending of an electron is synchronized by the trigger-send pulse on the source QD. The quantum rails have a total length $\approx$ 60 µm and the SAW propagates at a speed of $v_\mathrm{SAW} \approx 2.86$ µm/ns, which sets a flight-time $\approx$ 22 ns. A long pulse is applied to the barrier gate where the amplitude V_p is swept for the calibration experiment. **(c)** Transfer probability P_{10} (one electron at the lower receiver) with an electron sent from the lower source QD. The black dotted line corresponds to the data from sweeping the DC bias V_B (top x-axis) with no RF pulse ($V_\mathrm{p} = 0$). Similarly, the red solid line corresponds to P_{10} as a function of the pulse amplitude V_p (bottom x-axis) with $V_\mathrm{B} = -1.275$ V.

Let us now apply a long voltage pulse ($\Delta t = 500$ ns) to the barrier gate with a fixed DC bias $V_B = -1.275$ V. As we vary the pulse amplitude V_p (red line; bottom x-axis), P_{10} follows the course of the reference measurement (black dotted line). We extract from these results the reference amplitude range for turning on and off the coupling between the quantum rails with the barrier pulse.

In order to verify these arrival times, we employ a step pulse which allows the transition from a high-barrier scenario (two independent rails) to a 50:50 single-electron partitioning at a delay t_B (see pulse sequence in Fig. 6.2b). As in the previous experiment, we send one electron from the lower QD and perform single-shot measurements. Figure 6.2c shows the probability P_{10} (red) and P_{01} (blue) as a function of t_B. We identify first the DC limit for $t_B < 0$ (before sending the electron). Since the barrier is low ($V_p = 0$ V) over the entire electron trajectory, the data shows the expected 50:50 partitioning. On the contrary, when $t_B > 18$ ns (after the exit), the high barrier ($V_p = -0.3$ V) prevents the electron to end up in the opposite path, thus $P_{10} = 100$ %.

Let us now focus on the region in between these two DC limits. We observe that after the sending process ($t_B = 0$), the probability P_{10} remains constant until 2 ns after the electron arrival at the entrance ($t_B \approx 4$ ns). One explanation is

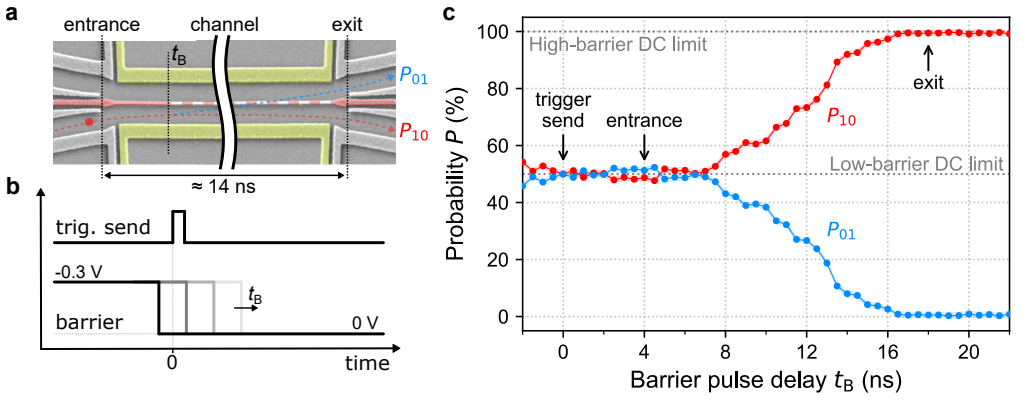

Figure 6.2: Pulse delay calibration. **(a)** SEM image of TCW with indications of the entrance, the exit and the electron injected from the lower quantum rail. The channel has a length ≈ 40 µm which means a flight-time ≈ 14 ns. **(b)** Employed pulse sequence with the trigger-send signal as a time reference ($t = 0$). A step function is applied to the barrier gate with an initial situation of no coupling between the rails (V_p=-0.3 V; high barrier; see Fig. 6.1c). The barrier is then lowered ($V_p = 0$ V) to allow electron partitioning. **(c)** Single-shot probability P_{10} (red) and P_{01} (blue) with an electron sent from the lower source QD as a function of t_B. The arrows indicates the expected time-delay with respect to the trigger-send pulse ($t = 0$) of the electron arrival to the entrance ($t \approx 4$ ns) and the exit ($t \approx 18$ ns). Each data point is the result from 2000 single-shot measurements.

that the pulse has no influence on the electron along the injection path. However, we cannot discard the scenario where the electron is excited by the non-adiabatic voltage change, but relaxed by the time it arrives at the exit. On the other hand, the probability saturates at $t_B \approx 18$ ns which is in good agreement with the expected electron arrival at the exit.

The gradual transition from 50 % to 100 % is however puzzling. This suggests that the current configuration of the electron-partitioning process requires the entire TCW ($\Delta t_B \approx 14$ ns). For example, if we turn on the coupling for half the interaction time ($\Delta t_B \approx 7$ ns; $t_B = 11$ ns), the electron has only 25 % probability to go to the opposite side. A possible explanation for such a time-dependent behavior could be the relaxation of the electron during the propagation. In order to verify this hypothesis, it is necessary to perform follow-up experiments such as investigations on the pulse amplitude.

6.2 Dynamical collision of an electron pair

Having calibrated the barrier pulse with a single electron, in the following we investigate the influence of the employed step-pulse sequence (see Fig. 6.2b) on a synchronously transported electron pair. Figure 6.3a shows the probability P_{11} (detection of one electron at each receiver QD) as a function of the pulse delay t_B from synchronized sending of a single electron from each source QD (black circles). In order to have the reference case of two independent electrons, we use the single-electron probabilities P_{10}^i and P_{01}^i where i is either A (one electron from the lower source) or B (one electron from the upper source). Considering $P_{11} = P_{10}^B \cdot P_{01}^A + P_{01}^B \cdot P_{10}^A$ (see equation 34 in Section 5.2), we then reconstruct the non-interacting P_{11} (grey squares).

Let us first focus on the reference DC limits. When the low-barrier regime covers the entire electron trajectory ($t_B < 0$), we observe an increased antibunching rate $P_{11} \approx 70$ %[1]. In contrary, having a high barrier over the entire TCW ($t_B > 18$ ns), the electrons remain in their respective rails ($P_{11} = 100$ %).

In order to evaluate the electron-electron interaction, we extract the excess in the antibunching probability ΔP_{11} (see Fig. 6.3b). We observe that ΔP_{11} decreases even when the pulse is applied before the electron arrival at the entrance ($t_B = 4$ ns). We note that the barrier gate is placed in parallel along the entire injection path (see SEM image in Fig. 4.2 from Section 4.1). One possible explanation is that this non-adiabatic pulse causes the electrons to tunnel to subsequent

[1] This value is slightly lower to the maximum reported $P_{11} \approx 80$ % in Chapter 5 because of the here-employed SAW power $P \approx 26$ dBm, which is lower than the previously-used $P \approx 28$ dBm. As mentioned previously, the reason is that these experiments were performed in a different cool down after upgrading the RF setup, and the sample tuning for the maximum SAW power was not optimized yet.

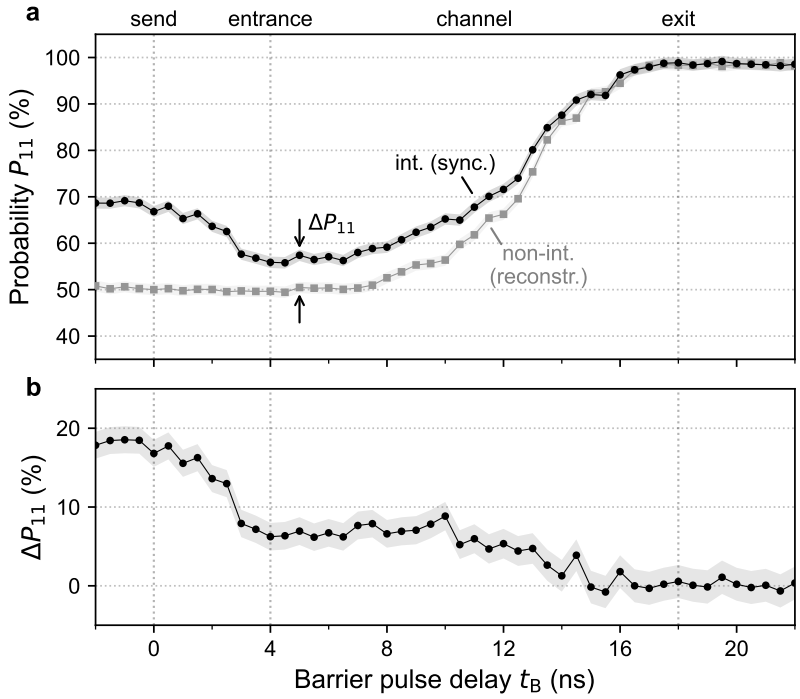

Figure 6.3: Time-resolved collision of an electron pair. (a) Probability P_{11} (one electron at the upper and the lower receiver) with synchronized sending of a single-electron from each source QD (black circles) as a function of the step-pulse delay t_B (see pulse sequence in Fig. 6.2). The non-interacting case (grey squares) is evaluated with single-electron data under the same circumstances. Reference time-delays are indicated with vertical dotted lines. Each data point is the result from 2000 single-shot measurements. **(b)** Excess in antibunching probability ΔP_{11} (see arrows in (a)) with indication of the error range (grey area).

SAW minima, and therefore the synchronization is partially lost. Turning on the coupling after the entrance, the data shows a small, but non-zero $\Delta P_{11} \approx 8$ % that remains constant for about half of the TCW length ($\Delta t_B \approx 7$ ns). Despite the ΔP_{11} reduction, this result indicates that the antibunching effect happens in a length scale shorter than the 40-µm-long coupling region.

In order to investigate the influence of the barrier pulse on the electron synchronization, we suggest that one strategy is to carefully study the pulse amplitude as well as the rising and falling slopes. We anticipate that these experiments will shed light on the observed features.

6.3 Time-resolved decoupling of quantum rails

In the previous section, we have presented experiments where the coupling is turned on at different locations in the TCW. By maintaining a high barrier after the electron enters the double-channel, we can effectively eliminate the abrupt potential near the entrance. Similarly, we can investigate the influence of the exit potential by performing the inverse pulse sequence (see schematic in Fig. 6.4a). The idea is to start with a low barrier until the coupling between the paths is removed by rising the barrier height at the pulse delay t_{B}.

Figure 6.4b shows the transfer probability P_{10} for a single electron sent from the lower (red) or the upper (blue) source QD as a function of t_{B}. The probabilities saturate at both DC limits ($t_{\mathrm{B}} < 0$ and $t_{\mathrm{B}} > 18$ ns) as expected. When the barrier height is increased during the electron propagation in the injection path ($0 < t_{\mathrm{B}} < 4$ ns), we observe a gradual change in the single-shot probabilities. The data shows moreover an asymmetry between the injection sides. We note that, in contrast to the previous step-pulse experiment (see Fig. 6.2c), here we prevent the electron to transit to the opposite quantum rail by rising the barrier at time t_{B}. Therefore, the transmission probability should reflect the energy state of the electron during its propagation. Following this argument, one possible cause for the observed change in the injection path is the electron excitation due to the non-adiabatic voltage pulse. This scenario is however not compatible with the observed asymmetry because we expect an equal pulse influence for both injection sides. Another possibility is the potential inhomogeneity caused by the ionized Si-dopants in the heterostructure [ND90; HH13]. Owing to its random distribution, an electron sent from each source QD would experience a different potential landscape along the injection rail.

Rising the barrier after the entrance ($t_{\mathrm{B}} > 4$ ns), the data shows a non-uniform course in the coupling region with an abrupt reduction at $t_{\mathrm{B}} \approx 13.5$ ns. As in the previous discussion, if the pulse leads to electron excitation, the effect should be similar at any location within the TCW. Owing to the non-gradual evolution, we can rule out this hypothesis. The other possible explanation is that the potential profile in the TCW is not uniform over the entire 40 µm length. This can be caused by small variations in the barrier-gate width, although from our SEM characterizations prior cool down, we did not see significant changes above 5 nm. This leaves us with the last possible compatible explanation that we have so far: the random distribution of Si-dopants [ND90; HH13].

Let us now perform the same pulse sequence, but with two electrons. Figure 6.4b shows the antibunching probability P_{11} as a function of the pulse delay t_{B} for a synchronized electron pair (black circles) and the reconstructed non-interacting scenario (grey squares). We observe a non-uniform P_{11} evolution in the coupling region similar to the single-electron cases. As in previous analysis,

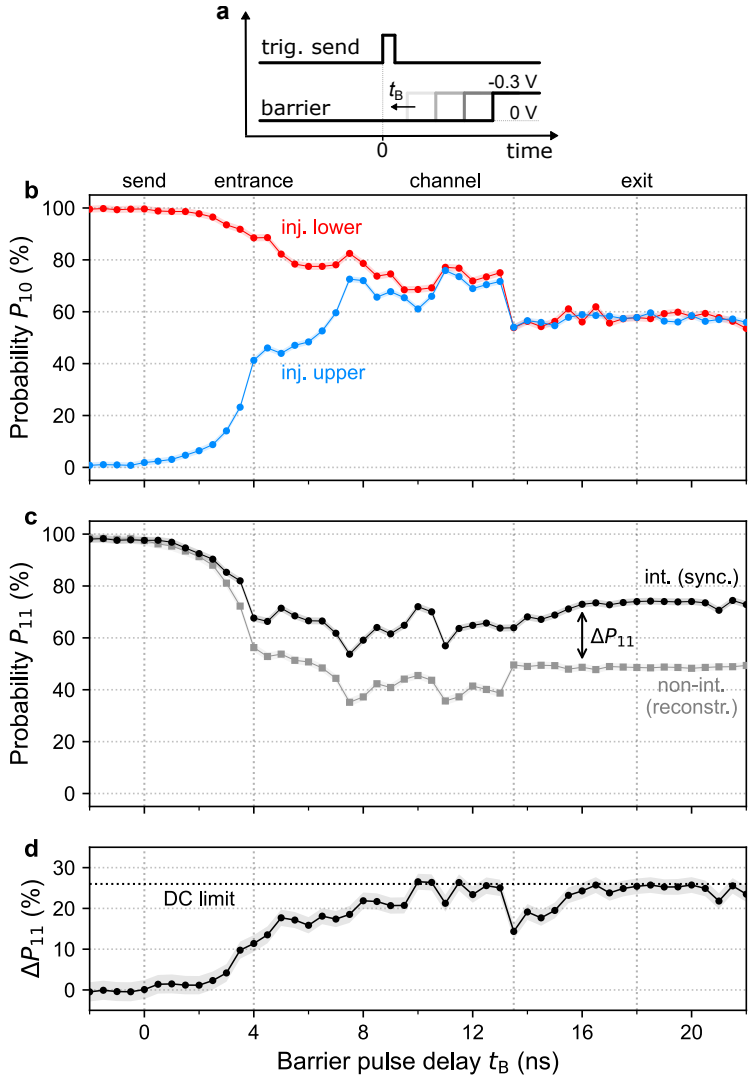

Figure 6.4: Time-resolved decoupling experiments. (a) Schematic of the pulse sequence with the trigger-delay at $t = 0$ and a step function applied on the barrier gate. The coupling between the two rails is enabled with an initial low barrier ($V_p = 0$) until the rising time t_B ($V_p = -0.3$ V). **(b)** Transfer probability P_{10} as a function of the pulse delay t_B for a single electron injected from the lower (red) or the upper (blue) source QD. **(c)** Probability P_{11} in the presence of two synchronized electrons (black circles) using the same pulsing sequence as shown in (a). The non-interacting case (grey squares) is reconstructed with the single-electron data from (b). **(d)** Excess probability ΔP_{11} as a function of the pulse rising time t_B. Each point has an error range (grey area) determined by 2000 single-shot measurements. The DC limit $\Delta P_{11} \approx 26$ % (black dotted line) corresponds to a low barrier over the entire electron trajectory.

we evaluate the excess in antibunching rate ΔP_{11} to extract the contribution from electron-electron interaction (see Fig. 6.4c). The data shows that the interaction gradually increases up to $\Delta P_{11} \approx 26$ % at $t_{\mathrm{B}} \approx 10$ ns. The matching with the DC-limit value confirms our expectation that it is not necessary to have the entire TCW for the antibunching effect to be manifested. Furthermore, since the rising of the barrier happens in the middle of the TCW, we can also conclude that the exit potential seems to have no significant influence on the antibunching rate.

6.4 Conclusion

In this chapter, we have shown preliminary results from the real-time control of the barrier height. We first employed a long square pulse on the barrier gate to calibrate the RF amplitude. Sweeping the delay of a step function, we identified the electron arrival at the different locations of the nanocircuit. Turning on dynamically the coupling between the quantum rails, we report the signature of electron-electron repulsion for various interaction times. Although the data interpretation is still on-going, these results lay the groundwork for unveiling the dynamics of the flying electron in a SAW-driven circuit of coupled quantum rails.

The presented technique has shown already promising results. Owing to the design flexibility of the voltage waveform, this method will open up a sea of possibilities. For example, we can turn on the coupling only for a short time at different locations in the TCW. This would allow for instance to study the electron relaxation during its flight or the non-uniform potential profile along the path. More interestingly, controlling the duration of this short pulse would enable investigations on coherent Rabi oscillations with a single flying electron. Owing to the energy scale of such quantum effects, we can engineer the pulse to keep the flying electron in its ground state. For example, we can avoid the abrupt potential change at the entrance by defining a falling slope from high to low barrier over few nanoseconds in the tunnel-coupled wire. In short, we consider this technique as an essential tool for in-flight quantum manipulations of a SAW-assisted flying electron.

CHAPTER 7

Acoustic chirped pulse for scalable transport

In the previous chapters, we have presented the progress of SAW-assisted single-electron transport in a circuit of coupled quantum rails. Combining for instance essential building blocks such as in-flight partitioning and synchronization of single-electron sources, we are able to exploit the interaction between a pair of flying electrons. This demonstrates the feasibility of the SAW-driven approach for performing electron-quantum-optics experiments as well as representing an excellent testbed for the electronic version of flying qubits.

Sound-driven single-electron transport has however an intrinsic limitation related to the large spatial extent of the SAW train. The quantum state of the flying electron can be perturbed by SAW modulation during the dwell time in the stationary QDs [Ber16]. Due to the presence of many potential minima accompanying the SAW (typically hundreds) it is thus difficult to transport the electron with accurate timing. To overcome this problem, delay-controlled sending process have been developed [Tak19]. Despite its versatility, this technique has however two major limitations:

- **Hardly scalable:** the number of RF components as well as AWG channels increases linearly with the number of single-electron sources to be synchronized – see Section 4.6.
- **Not compatible with high SAW power:** as the SAW amplitude increases, the metastable position required for the trigger-send technique becomes impossible to achieve – see Section 4.7.

What would be the ideal solution? Analyzing the aforementioned limitations, we find that the answer naturally emerges: an acousto-electric potential with a *single* propagating minimum.

In this chapter, we use the acoustic analogue to chirped pulses in optics [SM85] to first demonstrate the generation of a single, strongly compressed SAW. To determine the shape of the engineered SAW, we perform time-resolved measurements with a broadband IDT as SAW detector. By comparison of the experimental data with numerical simulations based on an impulse-response model, we assess the reliability of the synthesis method and outline a path towards maximum pulse compression. To show its applicability, we then let a single electron *surf*

on this acoustic wavefront and evaluate the transport efficiency between distant quantum dots. Triggering the SAW-driven sending process with a picosecond voltage pulse, we then investigate if the electron is fully confined in the central minimum of the chirped pulse. Finally, we apply a superposition of phase-shifted chirp signals to demonstrate the emission of multiple SAW pulses with precise control on their time delay.

The experiments presented in this chapter [Wan22b] are the results from a collaboration between Néel Institute (CNRS) in Grenoble and the National Institute of Advanced Industrial Science and Technology (AIST) in Japan. The design optimization, nanofabrication and IDT characterizations are performed in Grenoble. The single-electron transport measurements with chirped pulses are carried out by Shunsuke Ota and Shintaro Takada in Japan.

7.1 Pulse compression via chirp synthesis

A SAW emitted by an interdigital transducer is uniquely determined by its electrode design [Mor07; Eks17; Dum19]. Changing the unit cell pattern allows for instance the generation of higher SAW harmonics for the formation of periodic waveforms of arbitrary shapes [Sch15b]. The conceptual generalization of this Fourier-synthesis approach is the emission of a *solitary* SAW pulse. It can be achieved by the so-called chirp IDT whose frequency response is determined by its gradually changing cell periodicity λ_n. In quantum applications, this approach was so far mainly employed to broaden the IDT's pass band [Wei18]. The chirp design can however also be employed in an inverse manner – similar to the formation of an ultra-short laser pulse [SM85] – to superpose a quasi-continuum of many elementary SAWs with gradually changing wavelength to a single distinct pulse.

In this work, we aim at the emission of a solitary SAW wavefront approaching the form of a Dirac δ function. Mathematically, it is approximated via the superposition of a discrete set of frequencies f_n

$$\delta(t) \propto \int_{-\infty}^{\infty} e^{i\,2\pi\cdot f\cdot t}\,\mathrm{d}f \approx \sum_{n=1}^{N} e^{i\,2\pi\cdot f_n\cdot t} \tag{56}$$

that is mostly destructive, except around the timing $t = 0$ where all elementary waves are in phase and interfere thus constructively.

The central idea for synthesizing such a SAW pulse with a chirp-IDT design is depicted in Fig. 7.1. By subsequently driving this set of elementary waves with frequencies f_n (see equation 56) according to its gradually changing cell periodicity $\lambda_n = v_{\mathrm{SAW}}/f_n$, we allow the formation of the spatially-compressed acoustic pulse.

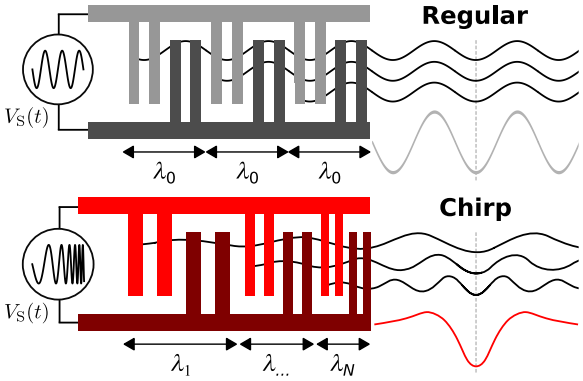

Figure 7.1: Pulse compression with chirp transducer. Schematic showing finger design, input signal V_S and SAW waveform for a regular IDT (black; reference) and a chirp IDT (red).

Applying an input signal

$$V_S(t) \propto \sin\left(2\pi \int_0^t f(\tau)\,\mathrm{d}\tau + \phi_0\right), \tag{57}$$

with properly chosen frequency modulation $f(t)$, the chirp transducer allows to excite the elementary waves with frequency f_n at the right timing to achieve the desired superposition.

The design of the chirp IDT is determined by the set of frequencies f_n. A natural choice for f_n is an evenly spaced set

$$f_n = f_1 + (n-1)\cdot\Delta f, \qquad \Delta f = \frac{f_N - f_1}{N-1} \tag{58}$$

leading to the following recurrence relation for the cell periodicity

$$\lambda_{n+1} = \frac{1}{\frac{1}{\lambda_n} + \frac{\Delta f}{v_{\mathrm{SAW}}}} \tag{59}$$

With this chirp geometry, maximal pulse compression is achieved by applying an input signal – see derivation in Appendix E.2 – with frequency modulation that follows an exponential course:

$$f(t) = f_1 \cdot \mathrm{e}^{\Delta f \cdot t} \tag{60}$$

7.2 SAW dispersion at GHz regime

To ensure that the SAW shape remains unchanged during propagation, it is primordial to verify the linearity of SAW dispersion for the frequency range of interest. Therefore, we investigate the resonant response of six regular aluminium

IDTs on a GaAs substrate at room temperature. By targeting resonance frequencies from 1 to 8 GHz, we fabricate IDTs that have cell periodicity ranging from ≈ 2.8 µm to 350 nm. We then perform transmission measurements between two identical IDTs using the experimental setup described in Section 3.2. Figure 7.2 shows a plot of the extracted resonance frequencies as a function of the wavenumber $k/2\pi = 1/\lambda_0$. The data shows a linear dispersion up to ~ 8 GHz. We deduce the SAW velocity for aluminium IDTs on GaAs via the slope of the linear fit as $v_{\mathrm{SAW}} = (2.81 \pm 0.01)$ µm/ns. These results confirm the widely linear SAW dispersion on GaAs, even at GHz regime.

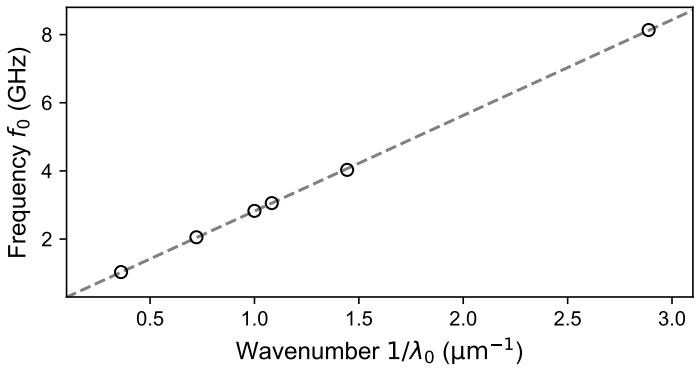

Figure 7.2: SAW-dispersion relation for aluminium IDTs on GaAs substrate. Resonance frequency for IDTs having different periodicity – here expressed as wavenumber $1/\lambda_0 = k/2\pi$. The points are extracted from Gaussian fits of distinct peaks in the transmission data (reflection data for the case of 8 GHz) from a network analyzer measurement between two identical transducers. All IDTs have a double-finger design except of the single-finger IDT for the case of 8 GHz. The slope of the linear least-squares fit (dashed line) indicates a SAW velocity $v_{\mathrm{SAW}} = (2.81 \pm 0.01)$ µm/ns.

7.3 Generation of an acoustic chirped pulse

The synthesis of the strongly compressed acousto-electric pulse is performed with a chirp transducer as shown via the scanning-electron-microscopy (SEM) image in Fig. 7.3a. It consists of $N = 167$ cells ranging from $f_1 = 0.5$ GHz to $f_N = 3$ GHz with the cell periodicity gradually changing from $\lambda_1 \approx 5.56$ µm to $\lambda_N \approx 0.92$ µm according to equation 59. The SAW traveling time to cross the device is expected to be $t_{\mathrm{IDT}} \approx 120$ ns.

To characterize the frequency response, we measure the transmission S_{21} between two identical devices (see Fig. 7.3b). In order to remove parasitic signals from reflections at the sample boundaries, the transmission data is cropped in the time-domain after Fourier transform in the range of 300 to 600 ns (expected

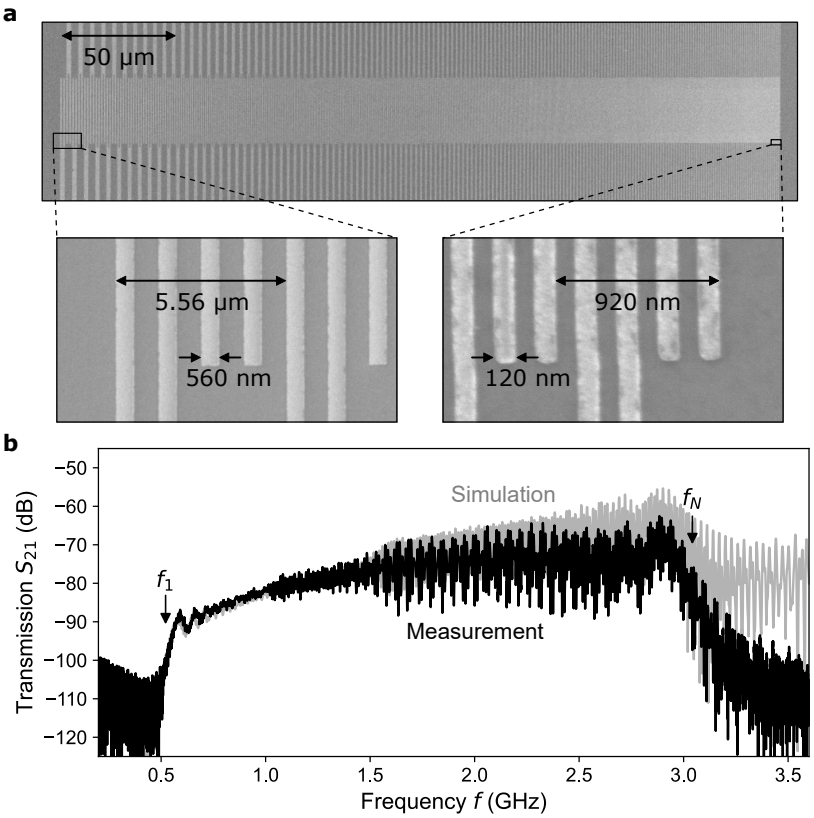

Figure 7.3: Chirp IDT. (a) SEM images of the chirp IDT with zooms (insets) in the regions of large (left) and small (right) periodicity of the interlocked electrodes. **(b)** Transmission measurement between opposing chirp IDTs (black) with simulation via the delta-function model (grey) and indications of the pass-band ranging from $f_1 \approx 0.5$ GHz to $f_N \approx 3.0$ GHz. Note that the transmission bandwidth of the radio frequency lines is not considered in the simulation.

arrival of first transient $\sim$ 310 ns) and then transformed back in the frequency domain. The transmission data shows a continuous spectrum ranging from $f_1 \approx 0.5$ GHz to $f_N \approx 3$ GHz. The response expected from the delta-function model (grey, see Section 3.3.2) reproduces the wide spectrum. The small deviation in the amplitude at the high-frequency end could be originated by the attenuation of the transmission lines and the impedance mismatch. Overall, the excellent agreement with the experimental data indicates the high quality of the fabricated chirp IDT.

Having outlayed the basic properties of the chirp IDT, let us now employ it for single-shot pulse generation. In order to study the SAW profile, we perform time-resolved measurements with a broadband detector IDT. We use the same

experimental setup as for the characterization of the regular IDT described in Section 3.2. In short, we apply a discrete input signal $V_S(t)$ to trigger for SAW formation. Owing to the piezoelectric coupling, an oscillating voltage $V_D(t)$ is induced when the acoustic wave arrives at the detector IDT. Using a fast oscilloscope, we then measure this voltage trace in real time.

The cell parameters of such a SAW detector ($\lambda_0 = 1$ µm, $N = 1.5$ unit cells) are chosen to have maximum sensitivity in the investigated frequency range – see Appendix E.1. As for the transmission signal, we apply a Fourier filter on the time-resolved data in the range of 0.4 to 3.5 GHz in order to suppress parasitic contributions from internal higher harmonics of the AWG, the amplifier responses, airborne capacitive coupling and standing waves in the radio-frequency lines.

For optimum pulse compression, it is important that the input signal matches the IDT response $V_S(t) = h(t)$. Therefore, the applied signal follows equation 60 with a duration $t_{Sig.}$ equivalent to the SAW-propagation time along the transducer $t_{IDT} \approx 120$ ns. Figure 7.4a shows the time trace of the detector signal at room temperature. We observe an initial electromagnetic crosstalk (at $t = 0$) followed by the SAW response appearing at the expected delay $t_{Det.}$. The clear contrast between the input signal duration $t_{Sig.}$ and the narrow SAW signal confirms the successful compression.

Zooming in the arrival window (see Fig. 7.4b), we observe the narrow response (black) has a single, main minimum. In order to verify that this SAW shape is consistent with the IDT design, we apply the impulse-response model as for the

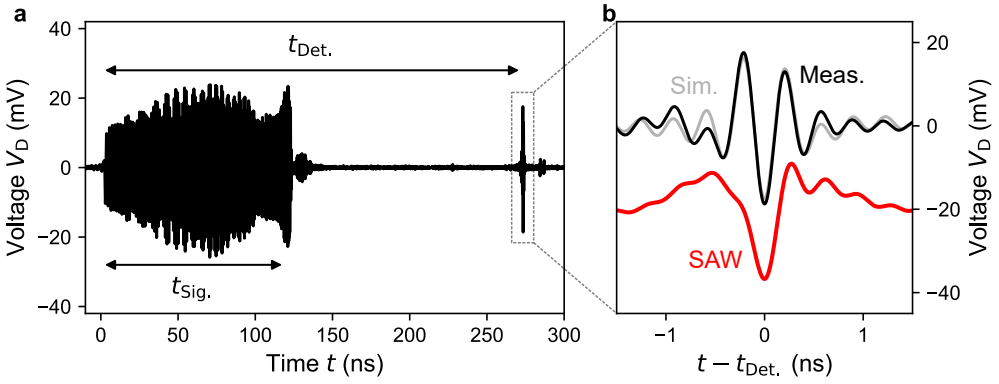

Figure 7.4: SAW profile of chirped pulse. (b) Time-resolved measurement (black) for frequency-modulated input signal applied on the chirp IDT with $t_{Sig.} \approx 120$ ns. **(c)** Zoom on the acousto-electric chirped pulse around the expected arrival time $t_{Det.}$ with impulse-response simulation (grey). The derived SAW shape (red; with offset and arbitrary units) via deconvolution of the detector response has a full width at half maximum FWHM ≈ 250 ps.

regular case (for details, see Section 3.3.4). We take into account in the simulation – see equation 22 – the response function of the chirp IDT $h(t)$ and the SAW detector $h_{\mathrm{Det.}}(t)$, and the applied input signal $V_{\mathrm{S}}(t)$. The phase offset $\phi_0 \approx \pi/2$ introduced by the amplifiers is also considered as part of the input signal $V_{\mathrm{S}}(t)$ (see equation 57). Since this model cannot account for the absolute insertion loss, we use the main peak amplitude as a fitting parameter. The expected SAW shape from the impulse-response model (grey line) reproduces the experimental data. Owing to the excellent agreement between experiment and simulation, we can extract the actual SAW shape by removing the contribution of the SAW detector $h_{\mathrm{Det.}}(t)$ from equation 22. We find that the actual SAW profile (red line with offset) has much flatter side lobes than the signal V_{D} on the broadband detector.

Slight deviations from the design are often present after fabrication that lead to minor changes in the IDT response. To compensate this irregularity for maximal pulse compression, we exploit the input signal parameters such as $t_{\mathrm{Sig.}}$ or f_1 (see equation 60). Figure 7.5 shows the broadening effect for input signals with duration $t_{\mathrm{Sig.}}$ deviating from the ideal parameter, t_{IDT}. When employing a non-ideal input signal ($V_{\mathrm{S}}(t) \neq h(t)$), each frequency is excited with a certain phase delay between them, resulting into broadening of the SAW pulse. Note that the impulse-response model (grey lines) is also able to predict the influence of non-ideal input signals. Owing to this compensation method, chirp synthesis becomes more robust against small variations due to the limits of precision in IDT fabrication.

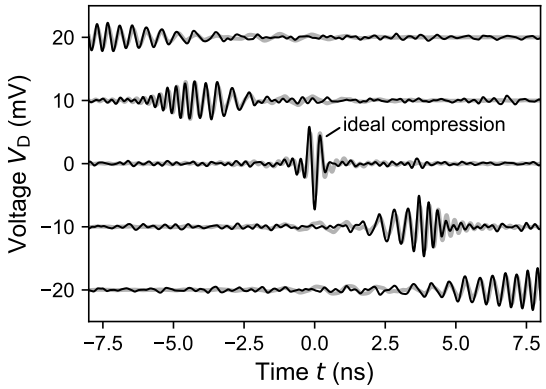

Figure 7.5: Compensation method for pulse compression. Time-resolved measurements of the SAW response (black; with offset) for an input signal with duration deviation of $t_{\mathrm{Sig.}} - t_{\mathrm{IDT}} \in [-10, -5, 0, 5, 10]$ ns (top to bottom). The grey line in the background shows the course expected from the impulse-response model.

7.4 Electron transport with compressed SAW

Let us now investigate the feasibility of this strongly-compressed acoustic pulse for single-electron transport. For this purpose, we employ the experimental setup shown in Fig. 7.6a. The chirp IDT provides the single, propagating potential minimum whose profile is characterized *in situ* by the SAW detector located

at the opposing end. In between, a straight quantum rail serves as a single-electron circuit (see Fig. 7.6b). An 8-µm-long channel connects two distant QDs, both equipped with a nearby QPC acting as highly-sensitive electrometer. The employed GaAs/AlGaAs heterostructure is the same as for previous experiments – for details, see Section 2.3. All experiments are carried out at a typical cryogenic temperature ~ 20 mK.

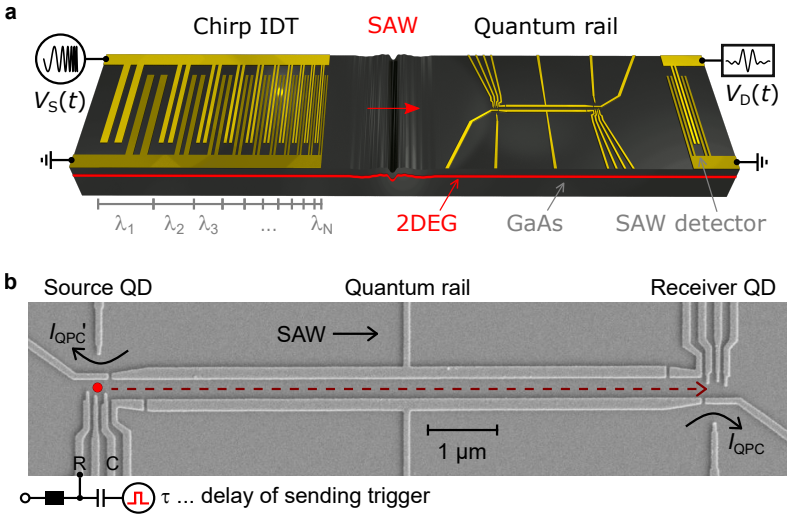

Figure 7.6: Experimental setup. (a) Schematic of chirp IDT launching a compressed SAW towards a quantum rail and a subsequent broadband SAW detector. Shown is a perspective view on the sample that is realized via metallic surface gates in a GaAs/AlGaAs heterostructure. **(b)** SEM image of the quantum rail consisting of two surface-gate defined quantum dots (QD) that are connected via a depleted transport channel. Shown are further the quantum-point-contact (QPC) electrometers that are placed next to each QD to sense the presence of electrons.

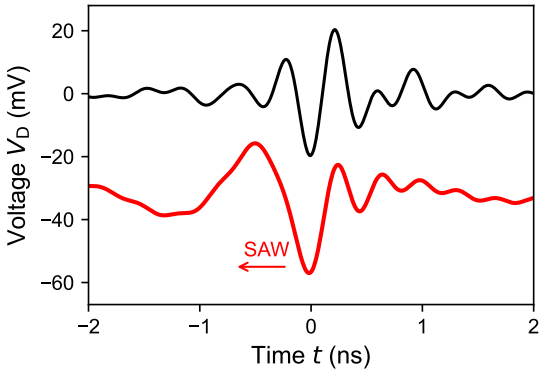

Figure 7.7: SAW profile at cryogenic conditions. Time-dependent measurement of the chirped pulse in the cryogenic setup via the SAW detector (black). The offset red line shows the corresponding SAW profile extracted by removing the detector's response function using the impulse-response model. The SAW propagation direction is indicated by the arrow.

In order to optimize the SAW profile for single-electron transport, we exploit input signal's phase offset ϕ_0 (see equation 57) to form an asymmetric chirped pulse. Note that an increased SAW velocity [PSK19] has to be taken into account for the input signal at cryogenic condition. Analyzing the SAW profile with $\phi_0 \approx 3\pi/2$, we observe a smooth ramp just before a first strongly pronounced minimum ($t < 0$) as shown in Fig. 7.7. With this choice, electron transfer is suppressed until the arrival of the leading SAW minimum as demonstrated hereafter.

To perform single-electron shuttling, for each transport sequence, we first evacuate all electrons in the system and then load one electron into the source QD. Subsequently, the chirp IDT is excited to emit the compressed SAW pulse which then propagates along the quantum rail. Figure 7.8 show the simultaneous QPC-current jumps ΔI_{QPC} at the source and the receiver QD for sending positions controlled via voltages on the reservoir (V_{R}) and the channel (V_{C}) gates. We find a region with complementary changes in the QD occupancy, indicating that the loaded electron is transported by the compressed pulse. Furthermore, the large parameter space for electron transfer suggests that chirp synthesis is a promising solution for unambiguous high-SAW-power transport.

As for the SAW-driven experiments with a regular transducer, we optimize the sending position to maximize the transfer efficiency. Figure 7.9a shows the histogram of ΔI_{QPC} at the receiver QD from 70.000 single-shot measurements.

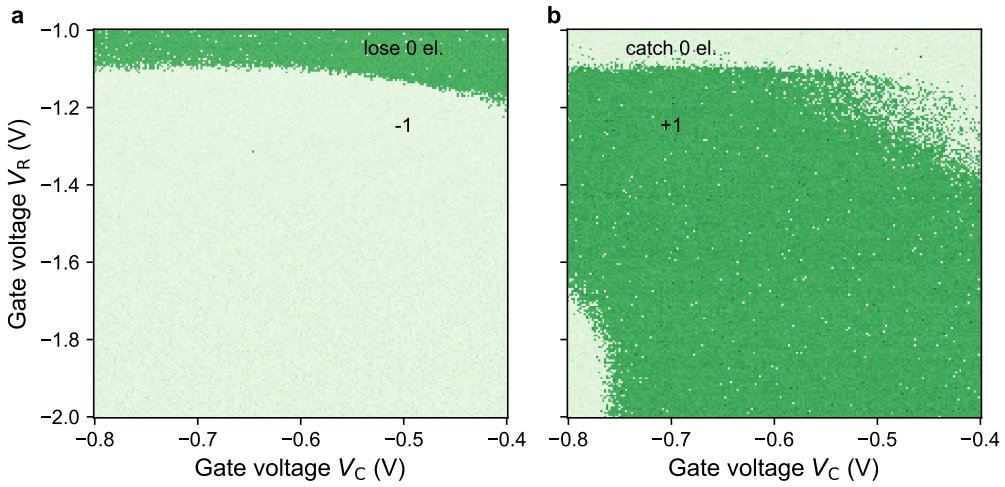

Figure 7.8: Electron transfer maps. (a) ΔI_{QPC} in the source QD after exploring the sending positions V_{R} and V_{C} in the presence of the compressed SAW pulse. 1 electron is loaded in the source QD prior SAW emission. The input signal applied to the IDT has a power $\approx$ 20.6 dBm. The color scale is chosen such that it highlights a change of one electron in the dot. **(b)** Simultaneously-measured electron occupancy map from the receiver QD with initially no electrons.

The comparison of the electrometer data shows sufficient contrast to clearly distinguish transport events. As reference, we perform each transport sequence also without loading an electron at the source QD (grey). This reference data allows to quantify the amount of undesired extra electrons injected into the system from outside (inflow). Figure 7.9b summarizes the transfer probability and the sources of error (loading, sending, catching and inflow). The negligible sending error (code 1100) indicates the high efficiency for the chirped pulse to pickup the electron from the source QD. Since we cannot distinguish between the failed events due to missed catching at the receiver dot and electron stuck events in the channel, we include both in the so-called catching error (code 1000). The overall low error rates lead to a single-electron transfer efficiency of $(99.4 \pm 0.4)\%$, similar to the highest values achieved with regular IDT design [Tak19].

Let us now investigate the transport efficiency for two electrons. Such a char-

a

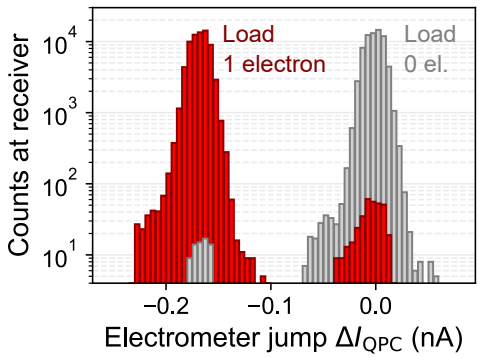

b

Probabilty	Code	Value (%)
Transfer	1001	99.4
Catching error	1000	0.4
Sending error	1100	0.0
Loading error	0000	0.1
Inflow (1 el.)	0001	0.1
Inflow (2 el.)	0002	0.0

Figure 7.9: Single-electron transport efficiency. **(a)** Histogram of jumps in the electrometer current ΔI_{QPC} at the receiver QD after launching the SAW pulse with (red) and without (grey) precedent loading of an electron in the source QD. The applied input signal for SAW formation has an amplitude $\approx$ 20.6 dBm. **(b)** Table of transfer- and error-probabilities with QD-occupation code of the events: (source before, source after, receiver before, receiver after).

Probabilty	Code	Value (%)
Transfer 2el.	2002	92.1
Missed 1el. error	2001	6.7
Missed 2el. error	2000	1.2
Sending error	2100 + 2200	0.0
Loading error	0000 + 1000	0.0
Inflow	0001 + 0002	0.1

Figure 7.10: Transport efficiency of a pair of electrons. Table of transfer- and error-probabilities with two electrons loaded in the source QD prior the SAW pulse. The code indicates the QD occupation: (source before, source after, receiver before, receiver after).

acterization is relevant for electron-quantum-optics experiments that involve confining a pair of synchronized flying electrons in the same SAW minimum. For this purpose, we perform the transport sequence after loading two electrons in the source QD. Figure 7.10 summarizes the probabilities of transfer errors and successful transport events. The negligible sending error (code 2100 + 2200) indicates that the chirped pulse can pick up two electrons with high efficiency. We find however a significant error related to the missing of one (6.7 %; code 2001) or both electrons (1.2 %; code 2000) that leads to a reduced transfer efficiency of 92.1 %. The increase in the 1e-missing error compared to the single-electron case (0.4 %; code 1000 in Fig. 7.9b) suggests that the electron is lost during the flight. We anticipate however that the transport efficiency can be improved by enhancing the single-minimum SAW amplitude.

7.5 In-flight electron distribution

For single-electron transfer with controlled timing it is necessary to verify that the electron is transported by the compressed SAW pulse. Time-of-flight measurements can unveil the in-flight distribution of the electron with high accuracy as reported in our previous work [Edl21]. However, we cannot apply this technique in the current sample design due to the lack of a barrier gate in the middle of the transport channel.

As an alternative, we employ the delay-controlled sending process [Tak19] introduced in Section 4.6. By using a fast voltage pulse injected via a bias tee on the

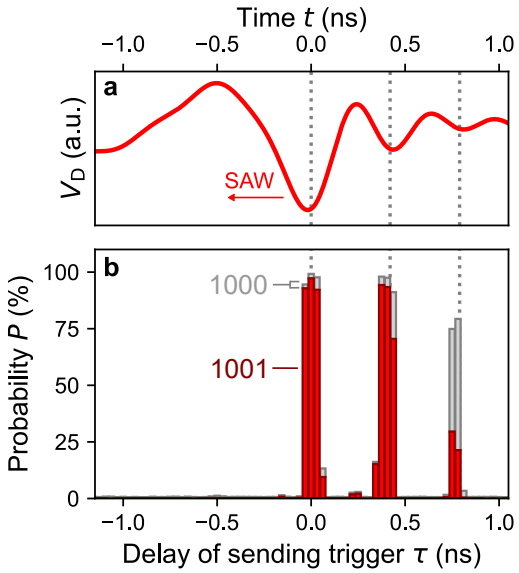

Figure 7.11: Time-resolved transport. **(a)** SAW profile (in a.u.) extracted from time-resolved measurements at cryogenic conditions (see Fig. 7.7). The arrow indicates the SAW propagation direction. The employed input power is ≈ 20.6 dBm. **(b)** Successful (1001) and failed (1000) transfer probabilities as function of the trigger delay τ of the sending process with respect to the SAW emission. The trigger pulse is applied for a duration ≈ 90 ps.

reservoir gate R of the source QD (see Fig. 7.6a), we trigger the sending process with respect to the SAW emission[1]. In this experiment, the potential landscape of the source QD is set such that the initially loaded electron is protected when the acoustic wave passes. By triggering a picosecond voltage pulse, the potential is temporary lifted to load the electron into the moving SAW. Sweeping the time delay τ of this trigger, we thus successively address each position along the SAW pulse in an attempt to transfer the electron. Figure 7.11b shows transmission probability data of such measurements with a pulse duration ≈ 90 ps. We observe three transmission peaks that emerge in congruence with the potential minima of the SAW profile – see Fig. 7.11a. Highest transport probability (code 1001) appears at the first peak ($\tau = 0$) that corresponds to the deepest minimum of the SAW pulse. The extent of 97 % sets a lower limit to the probability that the electron is emitted on arrival of that moving potential minimum at the source QD.

In order to gain insight whether the electron stays within this position as it propagates along the quantum rail, we look at the failed transfer events (code 1000). The strongly increased error at the third peak of more than 40 % indicates that it plays a rather negligible role, since without sending trigger this error is only 0.4 %. Estimating an amplitude of (19 ± 3) meV of the employed chirped pulse – see Appendix E.3 –, we cannot exclude transitions into the second minimum ($\tau \approx 0.4$ ns) during transport [Edl21]. We anticipate however reinforcement of single-minimum confinement via increased input-signal power and enhanced transducer design.

7.6 SAW engineering

The wide-ranging linearity of the SAW dispersion opens up a flexible platform to engineer any nanomechanical waveform using a single chirp IDT. Multiple δ pulses can be superposed via overlaid input signals $V_p(t)$ with deliberately chosen delay (Δt_p), phase (ϕ_p), and amplitude (A_p):

$$V(t) = \sum_{p=1}^{P} A_p \cdot V_p(t + \Delta t_p, \phi_p) \tag{61}$$

Following this approach, a sawtooth shape can be achieved for instance by superimposing uniformly delayed pulses with linearly decreasing amplitude.

For the sake of simplicity, we demonstrate this wave-engineering method by generating two pulses ($P = 2$) with arbitrary delay Δt. A relevant application

[1] In the single-electron circuit of coupled quantum rails, we applied the trigger-send pulse to the plunger gate P rather than the reservoir gate R. Both options have an equivalent effect on the delay-controlled sending process.

of such a synthesis is to improve the sequential sending of a pair of entangled electrons to observe spin interference patterns [Jad21]. Figure 7.12a shows an example of the non-trivial input signal for such a generation. From time-resolved measurements shown in Fig 7.12b, we observe a SAW profile with two identical pulses separated by the chosen delay Δt. Note that the halving in pulse amplitude compared to the single-pulse case ($\Delta t = 0$) is expected since the amplitude scales inversely with the number of superposed signals P (for $\Delta t < t_{\mathrm{IDT}}$). Owing to the linear SAW dispersion, the shape of the generated pulses is independent of the delay of the input signals V_1 and V_2. The accurate time-control of δ pulses lays the ground for on-demand emissions of arbitrary nanomechanical waveforms.

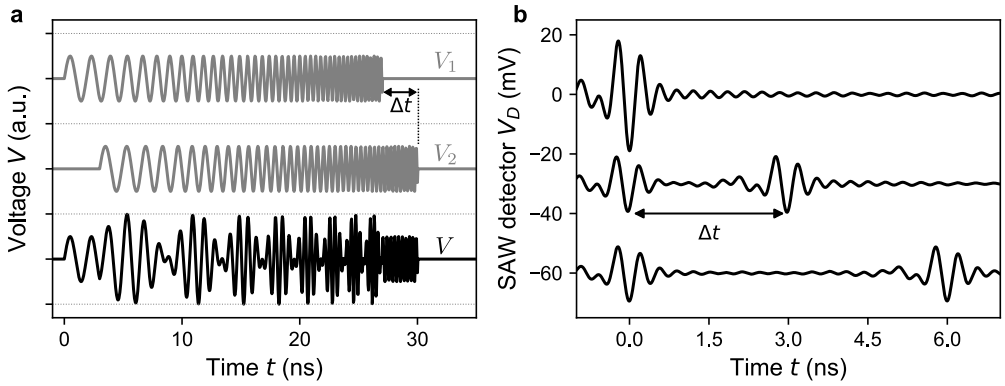

Figure 7.12: Acousto-electric wave engineering. (a) Input signal $V(t)$ composed by the superposition of $V_1(t)$ and $V_2(t)$ for the generation of two pulses with a delay Δt. **(b)** Time-resolved measurements from the SAW detector for an input signal with different time delays $\Delta t \in [0, 3, 6]$ ns.

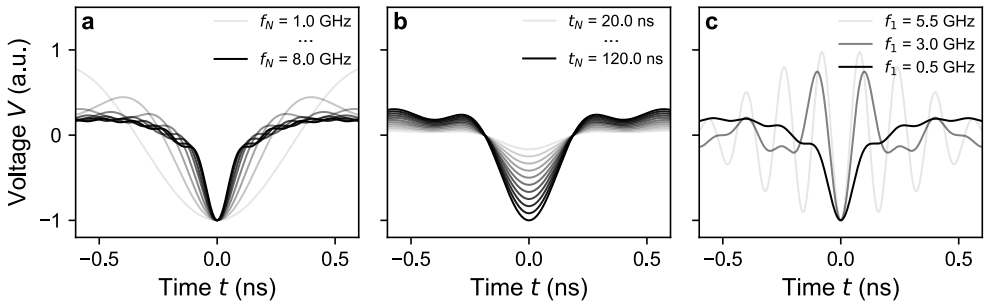

Figure 7.13: Effect of design parameters. SAW shapes of impulse-response model for changing IDT parameters. **(a)** Vary maximal frequency f_N in steps of 1 GHz, with $t_{\mathrm{IDT}} = 40$ ns and $f_1 = 0.5$ GHz. **(b)** Increase IDT length t_{IDT} in steps of 10 ns, with $f_1 = 0.5$ GHz and $f_N = 3.5$ GHz. **(c)** Reduce minimum frequency f_0 in steps of 1.5 GHz, with $t_{\mathrm{IDT}} = 40$ ns and $f_N = 7$ GHz.

The quality of the δ pulse determines the resolution of the engineered acoustic waveform. Owing to the agreement between time-dependent SAW experiment and simulation, we investigate numerically the design parameters of the chirp IDT. Figure 7.13 shows the evolution of the pulse shape for variations of the maximal frequency f_N, the IDT length t_{IDT} and the minimum frequency f_1. The simulations allow to formulate the following design rules for acousto-electric pulse generation with a chirp IDT:

1. The pulse narrows with increasing f_N – see Fig. 7.13a
2. The amplitude scales with the number of unit cells N – see Fig. 7.13b
3. Side lobes can be mitigated by reducing f_1 – see Fig. 7.13c

To form a clean acousto-electric pulse with strong potential confinement, it is thus important to design a chirp IDT with maximized length and frequency span.

7.7 Conclusion

In conclusion, we have developed a chirp synthesis method to generate in a single shot a strongly-compressed acoustic pulse. Combining the concept of Fourier synthesis and a chirp transducer operating in the frequency band of 0.5 to 3 GHz, we were able to emit a SAW pulse approaching the form of a δ function. Our investigations showed that imperfections in the transducer can be mitigated with adjusting input signal parameters, making the chirp synthesis a robust technique for reliable pulse compression.

Demonstrating a single-electron transport efficiency exceeding 99 %, we confirm robust potential confinement for unambiguous SAW-driven quantum transport. Confirming the confinement location during flight, this acoustic chirped wavefront thus represents the scalable alternative for synchronized and unambiguous SAW-driven single-electron transport from multiple sources.

Furthermore, by demonstrating the generation of two delayed acoustic pulses, we highlight that the chirp synthesis enables the possibility to engineer *arbitrary* acoustic waveforms. This method has particularly high relevance for experiments where multiple charges are transferred sequentially [Jad21].

Finally, we highlight that the demonstrated method is not restricted only to single-electron transport. We expect that the chirp approach opens up new routes for quantum experiments on interference and entanglement exploiting spin- and charge-degree of freedom of a single flying electron [BSR00; Sch15a; For17; Bäu18]. Moreover, we anticipate applications in hybrid-nanomechanical [MSF18], superconducting [Yok20a] and spintronic [Kob17; Yok20b] devices. For the latter

in particular, short SAW pulses will enable time-resolved measurements of magnetization and domain-wall displacement and will thus allow to replace optical techniques by sound [Che21].

Conclusion and perspectives

The main objective of this thesis was to implement in-flight control of a single-electron transported by sound. To achieve this goal, we started with the state-of-the-art device that consisted in a single-electron circuit of coupled quantum rails [Tak19] as reference. After identifying the bottlenecks in this sample, we developed a quantitative electrostatic model [Cha22] for optimizing the surface-gate geometry of the next generation SAW-driven electronic circuit. In parallel, we enhanced the IDT efficiency via lighter metallic electrodes, and investigated its influence on the SAW confinement threshold for unambiguous electron transport [Edl21].

All these improvements led to an optimized single-electron circuit of coupled quantum rails. We first calibrated the essential building blocks that include the single-electron sources and detectors, the synchronization technique and the tunable partitioning method in the coupling region. Motivated by the concept of Coulomb Coupler as a two-qubit gate, we decided next to asses its feasibility by investigating the electron-electron interaction with a synchronized flying electron pair [Wan22a]. Sending two electrons in the same or different SAW minima, we observed an enhanced antibunching probability up to $P_{11} \approx 80$ %. With electrostatic numerical simulations, we concluded that the dominant repulsion mechanism in our system is the Coulomb interaction. In the quest for the Coulomb Coupler, we anticipate that the estimated interaction strength will be sufficient for orbital entanglement between a pair of flying electrons.

Another important milestone for the SAW-transport platform is the demonstration of coherent manipulations of the flying quantum state. The strategy that we adopted to move towards such a challenging goal is to control the barrier height of the tunnel-coupled wire *in real-time*. Preliminary experiments using tailored voltage pulses on the barrier gate yielded already promising results. For instance, using the antibunching peak as a reference, we observed that this effect remained even with a shorter interaction time compared to previous "static" experiments.

We consider this time-resolved technique to be essential for the first demonstration of coherent in-flight manipulations. In particular, by turning on the coupling between the quantum rails for a controlled timing, we should be able to witness – within the time resolution of our instruments – any coherent oscillation of the single flying electron.

With a more complex pulse sequence, it is even possible to implement a Mach-Zehnder-like interferometer in our system. The idea is to combine a low barrier

height that allows to prepare a superposition state, with a high barrier regime that creates two independent paths. A pulse sequence of low-high-low barriers would then be similar to the MZ interferometer.

In the final chapter of this thesis, we focused on addressing an intrinsic limitation of the SAW-driven platform. Since only a single SAW minimum is needed for the electron transport, the presence of unwanted SAW modulations can perturb the quantum state of the electron [Ber16], and it also complicates the synchronization between multiple single-electron sources. We solve this problem by developing a novel SAW engineering technique based on a chirp IDT [Wan22b]. With time-resolved measurements, we demonstrate our ability to synthesize a single, strongly-compressed acoustic pulse. By showing that this SAW pulse can transfer single-electrons with almost unity efficiency, our chirp synthesis technique represents the scalable alternative for SAW-driven single-electron transport.

Appendix

A Nanofabrication

A.1 Interdigital transducers

The IDTs were fabricated using mainly electron beam lithography (ebeam). The exact steps are listed in Table A.1. Aiming for a frequency range in the GHz, the electrodes have a typical width below 125 nm with similar gap in between. Considering that the employed finger overlap is 30 µm, such a large aspect ratio represents the most challenging factor in the fabrication. In order to achieve high yield, I found out that a key aspect is to correct for the proximity effect in the ebeam-lithography process. For example, if we want to have an equal metal-gap ratio of 125 nm, we reduce the electrode width in the design by 40 % in the center, *i.e.* 75 nm, while reducing only 20 % at the boundaries.

To simplify the design process, I have developed an homemade Python module called `idtpy`[1]. Having user-friendliness in mind, this toolkit supports IDT designs such as regular, chirp, Split52 [Sch15b] and unidirectional [Dum19]. It allows to generate the commonly used GDS file that is compatible with standard lithography machines. Furthermore, it includes the delta-function model (see Section 3.3.2) and the impulse-response model (see Section 3.3.4) that facilitates the design process.

Table A.1: IDT nanofabrication recipe. Steps to fabricate an IDT, including the contacts and the metallic ground planes.

#	Method	Description
	IDT pattern	
1	Ultrasonic cleaning	10 min in acetone + 10 min in isopropanol (IPA)
2	Warming on hotplate	115 °C for 2 min + wait 5 min to cool down
3	Spin coating of resist	PMMA 3 %, 4000 rpm, 4000 rpm/s, 60 s + bake at 180 °C for 5 min
4	Ebeam lithography	Writing of IDT structures (*Nanobeam nB5*)
5	Development of resist	35 s in MIBK:IPA 1:3 + 1 min in IPA
6	Oxygen-plasma cleaning	With a power of 10 W for a duration of 10 s

[1]For more information, see `https://github.com/Junliang-Wang/idtpy`

7	Metal deposition	Ti 3 nm at 0.05 nm/s + Al 27 nm at 0.10 nm/s
8	Lift-off	N-methyl-2-pyrrolidone (NMP) at 80 °C for at least 1 h
	Contacts and ground planes	
9	Ultrasonic cleaning	20 s in acetone + 20 s in IPA
10	Spin coating of resist	S1805, 6000 rpm, 6000 rpm/s, 30 s + bake at 115 °C for 1 min
11	Laser lithography	Writing of contacts and ground plane
12	Development of resist	1 min in Microposit developer:DI H_2O 1:1 + 1 min in DI H_2O
13	Metal deposition	Ti 20 nm at 0.10 nm/s + Au 80 nm at 0.15 nm/s
14	Lift-off	At least 30 min in acetone

A.2 Surface-gate defined nanostructures

The device for SAW experiments are fabricated on a GaAs/AlGaAs heterostructure. The nanofabrication recipe is described in Table A.2. The QPC devices are fabricated following the same recipe, but without the steps corresponding to IDT fabrication.

Table A.2: Nanofabrication process for SAW devices.

#	Method	Description
	Mesa	
1	Ultrasonic cleaning	10 min in acetone + 10 min in IPA
2	Spin coating of resist	S1805, 6000 rpm, 6000 rpm/s, 30 s + bake at 115 °C for 1 min
3	Laser lithography	Mask for etching
4	Development of resist	1 min in Microposit developer:DI H_2O 1:1 + 1 min in DI H_2O
5	Etching	15 s in DI H_2O:H_2SO_4:H_2O_2 25:5:1 + 3 min in DI:H_2O. Calibrated to etch $\approx$ 120 nm.
6	Resist cleaning	2 min in Acetone + 2 min in IPA

	Ohmic contacts	
7	Spin coating of resist	S1818, 6000 rpm, 4000 rpm/s, 30 s + bake at 115 °C for 1 min
8	Laser lithography	Mask for Ohmic contacts
9	Development of resist	1 min in Microposit developer:DI H_2O 1:1 + 1 min in DI H_2O
10	Metal deposition	Ni 5 nm + Ge 60 nm + Au 120 nm + Ni 10 nm + Au 100 nm
11	Lift-off	At least 30 min in acetone
12	Ultrasonic cleaning	20 s in acetone + 20 s in IPA
13	Annealing	450 °C for 1 min in Ar environment
	Electron-beam marks	
14	Ultrasonic cleaning	30 s in acetone + 30 s in IPA
15	Spin coating of resist	S1805, 6000 rpm, 6000 rpm/s, 30 s + bake at 115 °C for 1 min
16	Laser lithography	Mask for electron-beam marks
17	Development of resist	1 min in Microposit developer:DI H_2O 1:1 + 1 min in DI H_2O
18	Metal deposition	Ti 20 nm + Au 100 nm
19	Lift-off	At least 30 min in acetone
	IDT pattern	
20	Ultrasonic cleaning	20 s in acetone + 20 s in IPA
21	Warming on hotplate	115 °C for 2 min + wait 5 min to cool down
22	Spin coating of resist	PMMA 3 %, 4000 rpm, 4000 rpm/s, 60 s + bake at 180 °C for 5 min
23	Ebeam lithography	Writing of IDT structures
24	Development of resist	35 s in MIBK:IPA 1:3 + 1 min in IPA
25	Oxygen-plasma cleaning	With a power of 10 W for a duration of 10 s
26	Metal deposition	Ti 3 nm + Al 27 nm
27	Lift-off	NMP at 80 °C for at least 1 h
	Single-electron circuit pattern	
28	Ultrasonic cleaning	20 s in acetone + 20 s in IPA

29	Warming on hotplate	115 °C for 2 min + wait 5 min to cool down
30	Spin coating of resist	PMMA 2 %, 4000 rpm, 4000 rpm/s, 60 s + bake at 180 °C for 5 min
31	Ebeam lithography	Writing of single-electron circuit
32	Development of resist	35 s in MIBK:IPA 1:3 + 1 min in IPA
33	Oxygen-plasma cleaning	With a power of 10 W for a duration of 10 s
34	Metal deposition	Ti 3 nm + Au 14 nm
35	Lift-off	NMP at 80 °C for at least 1 h
	Contacts and ground planes	
36	Ultrasonic cleaning	20 s in acetone + 20 s in IPA
37	Spin coating of resist	S1818, 6000 rpm, 4000 rpm/s, 30 s + bake at 115 °C for 1 min
38	Laser lithography	Writing of contacts and ground plane
39	Development of resist	1 min in Microposit developer:DI H_2O 1:1 + 1 min in DI H_2O
40	Metal deposition	Ti 30 nm + Au 170 nm
41	Lift-off	At least 30 min in acetone
42	Ultrasonic cleaning	20 s in acetone + 20 s in IPA

A.3 Miscellaneous problems

RBS cleaning

The standard fabrication recipe for SAW devices included an initial cleaning step in diluted solution of RBS. I realized that this process damages the surface of the GaAs substrate. Figure A.14 shows dark-field optical images of the substrate surface for increasing cleaning time in RBS. I found that even a 30 s step has a significant effect on the surface roughness. For instance, the damage is radically increased after etching (see bright regions in Fig. A.15). This effect is extremely detrimental for the success yield of IDTs because these devices are placed out

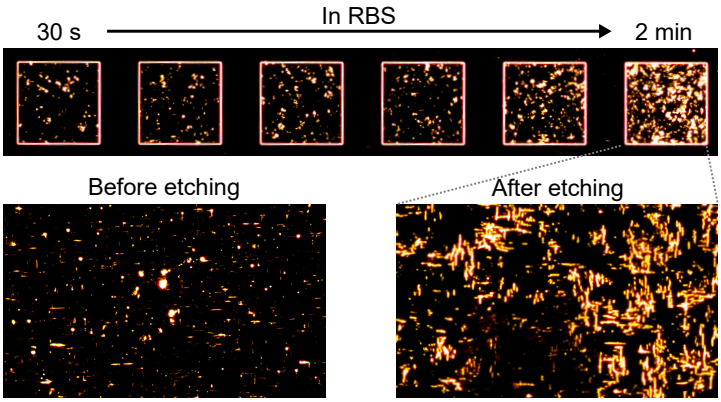

Figure A.14: RBS cleaning test. (Top) Optical images with the dark-field mode of the GaAs surface. Each region is placed in a diluted RBS solution with DI H_2O for a given duration. The bright color corresponds surface roughness. The size of each square is 200 µ. (Bottom) Zoom in the last region before and after wet etching for 15 s in DI H_2O:H_2SO_4:H_2O_2 25:5:1.

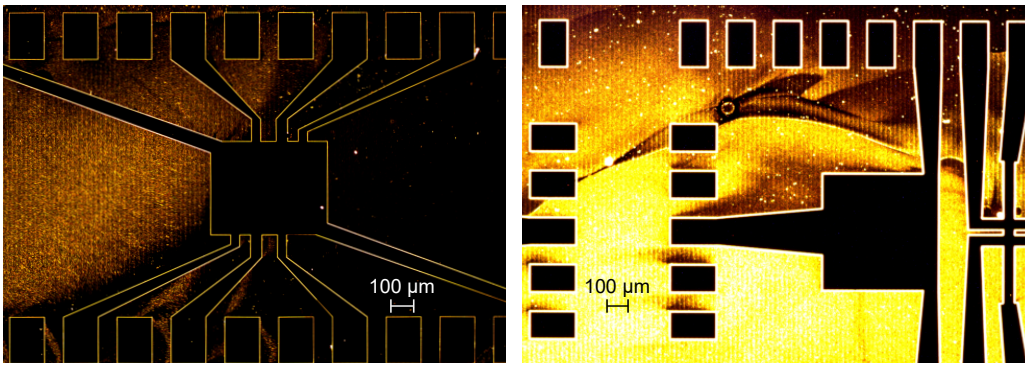

Figure A.15: Example of RBS damage. Dark-field optical images of the damage caused by RBS cleaning in typical devices. Black regions correspond to non-etched areas. The brightness is related to the surface roughness.

of the mesa, *i.e.* at the etched regions. Furthermore, the edge of the mesa has unwanted undercuts – see Fig. A.16 – that causes disconnections in the metallic gates that are deposited on top. Having identified the problems caused by RBS, I simply removed this cleaning process from our recipe.

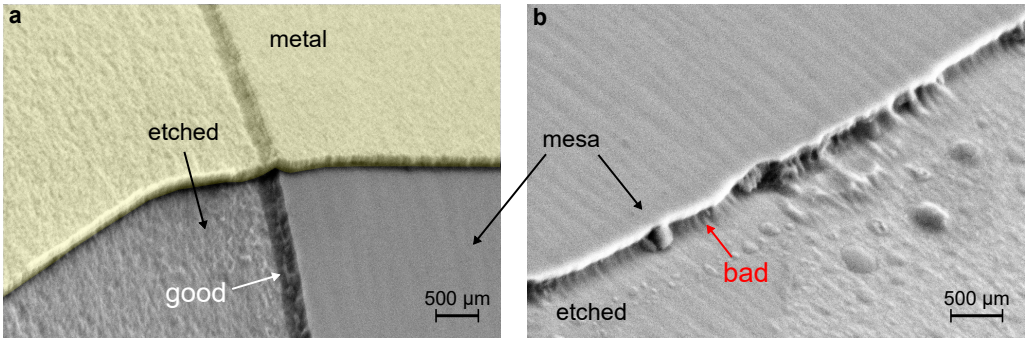

Figure A.16: Mesa. (a) Tilted SEM image near the edge of the mesa with indication of the etched area. The metallic gate (yellow) that is deposited on top has no disconnection at the mesa edge. **(b)** Sample etched after a cleaning process with RBS. The mesa edge has a significant undercut (bad) compared to the good step shown in (a).

Electron beam focus

Another important finding that helped to achieve high nanofabrication yield is related to the ebeam focus. Prior the ebeam exposition for the nanocircuit, we usually calibrate the dose with "dummy" GaAs substrate. In previous generations, we observed a deviation in the success rate between exposition on the dummy and on the HEMT. I realized that the ebeam marks in the HEMT were located in the etched region, meaning that there was a height difference of ≈ 150 nm compared to the dose test. Since the ebeam resolution is very sensitive to its focus, by placing the marks on the mesa, I successfully obtained similar fabrication yield.

Cleaving method

The last step of a sample fabrication is the cutting process. In a typical chip (10 cm×10 cm), we have usually 8 samples in a grid of 2 by 4. We first add a thick resist layer (> 2 µm) to protect the surface gates. Then, we use a scribe marking machine that is equipped with a diamond tip and a camera for the alignment. After scribing along a crystallography line, we cover the chip with a plastic film and apply pressure with a blade on the backside. It turned out that the nanostructures were destroyed after this process (often more than half of the devices). In particular, I found out that the cause was due to electrical discharges by the surface pressure perceived by the gates.

In order to solve this problem, I designed a metallic piece with a notch of 135° (see Fig. A.17). First, I ground this support piece to avoid electrical discharges. I cover the surface with a soft cloth such as a clean-room paper. I then put the chip, which was previously marked with the diamond tip, upside down on the notch. Next, by applying pressure along the scribed line with a sharp scalpel, the chip would break in two pieces. Thanks to the particular angle, even if the scalpel hits the metallic support, the pair of pieces would fall gently on the sides without receiving any surface pressure. Performing SEM characterizations with dummy nanostructures before and after performing this cleaving method, I observed that no damage was induced. Owing to this cleaving method along with the other tailored solutions, I successfully increased the nanofabrication yield above 90 %.

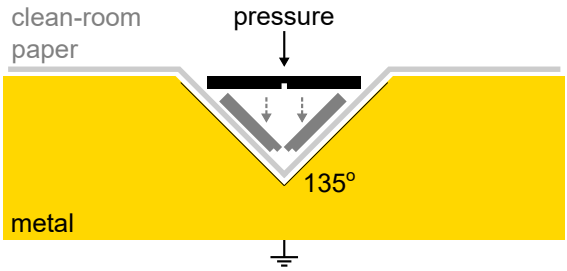

Figure A.17: Sample cleaving. The sample (black) previously scribed is placed upside down on a clean-room paper (light grey) resting on a grounded metallic piece (yellow) with a 135°-notch. Applying pressure along the scribed line with, for example, a scalpel (not shown), the sample would break into two which fall gently on the side of the walls.

B Charge density calculations in nextnano

In the following, we briefly introduce the calculations for the charge densities in the nextnano software. Extensive details of the solver can be found in Ref. [Bir07; And09]. The Poisson equation (see equation 12) and the Schrödinger equation

$$\left[\frac{\vec{p}^{\,2}}{2m_0} + eU(\vec{r})\right]\psi_n(\vec{r}) = E_n\psi_n(\vec{r}) \tag{B.62}$$

are related via the charge densities p and n (see equation 13). In the classical approach, nextnano uses the Thomas-Fermi approximation where the free carriers can be considered as

$$n_{\mathrm{cl}}(\vec{r}) = \sum_{\mu\in\mathrm{CB}} g_\mu N_\mu^{\mathrm{3D}}(\vec{r},T)\,\mathcal{F}_{1/2}\left(\frac{-E_\mu(\vec{r}) - eU(\vec{r}) + E_{F,n}(\vec{r})}{k_BT}\right) \tag{B.63}$$

$$p_{\mathrm{cl}}(\vec{r}) = \sum_{\mu\in\mathrm{VB}} g_\mu N_\mu^{\mathrm{3D}}(\vec{r},T)\,\mathcal{F}_{1/2}\left(\frac{E_\mu(\vec{r}) + eU(\vec{r}) - E_{F,p}(\vec{r})}{k_BT}\right). \tag{B.64}$$

Here, CB and VB denote for the conduction and the valence bands, μ is the chemical potential, k_B is the Boltzmann constant, T is the temperature, N_μ^{3D} is

the position- and temperature-dependent effective density of states of a three-dimensional free electron gas and the function $\mathcal{F}_n(E)$ corresponds to the Fermi-Dirac integral of order n,

On the other hand, the quantum effects are taken into account via the multi-band $\vec{k}\cdot\vec{p}$ envelope function method. In a quasi d-dimensional nanostructure, the general quantum mechanical multiband charge densities of electrons and holes are given by

$$n_{\mathrm{qm}}(\vec{r}) = \sum_{\mu\in\mathrm{CB}} \frac{g}{(2\pi)^{3-d}} \int_{\Omega_{BZ}} d^{3-d}\vec{k}_{\parallel} \left|F_i(\vec{r},\vec{k}_{\parallel})\right|^2 f\left(\frac{-E_i(\vec{k}_{\parallel}) + E_{F,n}(\vec{r})}{k_B T}\right) \tag{B.65}$$

$$p_{\mathrm{qm}}(\vec{r}) = \sum_{\mu\in\mathrm{VB}} \frac{g}{(2\pi)^{3-d}} \int_{\Omega_{BZ}} d^{3-d}\vec{k}_{\parallel} \left|F_i(\vec{r},\vec{k}_{\parallel})\right|^2 f\left(\frac{E_i(\vec{k}_{\parallel}) - E_{F,p}(\vec{r})}{k_B T}\right). \tag{B.66}$$

with appropriate envelope functions F_i and eigenenergies E_i from the Envelope Function Approximation. The factor g accounts for possible spin and valley degeneracies and the function f corresponds to the Fermi distribution.

C Cryogenic setup

C.1 DC line characterization

Our single-electron circuits are extremely sensitive to electrical discharges that can permanently damage the nanostructures. For this purpose, we keep all the gates grounded during any physical manipulation. However, I found out that abrupt voltage changes can be produced during the cool down of a sample even with the grounded DC lines. To solve this problem, I developed a method to characterize the DC lines during thermal cycling (see schematic in Fig. C.18a). The idea is to connect in parallel one or several lines to a grounded PCB. I then use an external resistor R_{ext} outside the dilution refrigerator with an input voltage V_{in}. The output voltage

$$V_{\mathrm{out}} = \frac{R_{\mathrm{eq}}}{R_{\mathrm{ext}} + R_{\mathrm{eq}}} V_{\mathrm{in}} \tag{C.67}$$

is sensitive to the equivalent resistance $R_{\mathrm{eq}} = (\sum_{i=1}^{n} 1/R_i)^{-1}$ determined by n parallel DC-line resistances. This circuit diagram is equivalent to a voltage divider. Figure C.18b shows an example of the voltage shift $\Delta V = V_{\mathrm{out}}(T = 300\ \mathrm{K}) - V_{\mathrm{out}}$ of a single DC line during a cool down with liquid N. No voltage shift is present in a stable line (grey; reference). In contrast, a "bad" line (red)

shows abrupt voltage changes (> 10 %) as the temperature varies. We verified that these unstable lines correspond indeed to the damaged gates in previous samples. We found that this was due to badly soldered connectors that have unreliable behaviors during thermal cycling. After fixing these issues, no more sample was damaged during cool down.

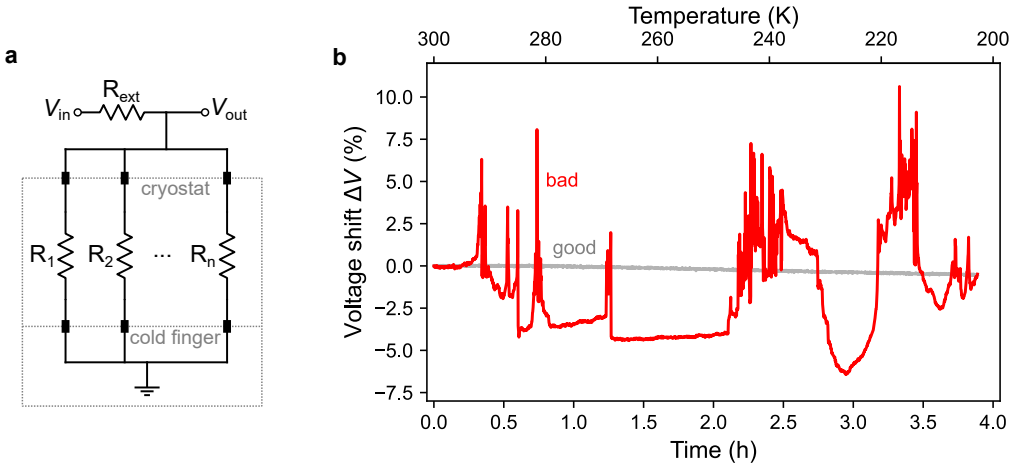

Figure C.18: Characterization of DC lines. (a) Circuit diagram of the characterization setup for the DC lines in the cryostat (grey dotted region). n parallel DC lines with resistances R_i with $i = 1, 2, ..., n$ are connected to a grounded PCB. At the room-temperature stage, an input voltage V_{in} is applied on an external resistor R_{ext}. The output voltage V_{out} is sensitive to resistance variations in the DC lines. **(b)** Voltage shift $\Delta V = V_{\text{out}}(T = 300\ \text{K}) - \text{V}_{\text{out}}$ with only one DC line as a function of time. The cryostat temperature is shown in the top x-axis. A bad line (red) can be identified from the abrupt temperature-dependent voltage changes. In contrast, a good line (grey) shows no variation.

C.2 RF line characterization

For the single-electron transport experiments and, in particular, the time-resolved control of the barrier gate, we employ a RF setup as shown in Fig. C.19a. We highlight that this setup had been constantly improved during the course of this thesis. The cryostat has a total of 4 RF lines that are attenuated between -5 dB to -6 dB. 3 broadband bias tees (SHF AG; 20 kHz to 40 GHz) enable to independently apply a DC bias and a RF signal on the source-QD plunger gates and the tunnel barrier. To generate sub-nanosecond voltage pulses, we use Keysight M8195A AWG that has a bandwidth of 20 GHz per channel. With two synchronized units, we have a total of 4 channels at 32 GS/s.

We further characterize with VNA measurements the DC and the RF part of

the setup (see Fig. C.19a and b). We note that the high-frequency transmission is currently limited by the material of the RF lines.

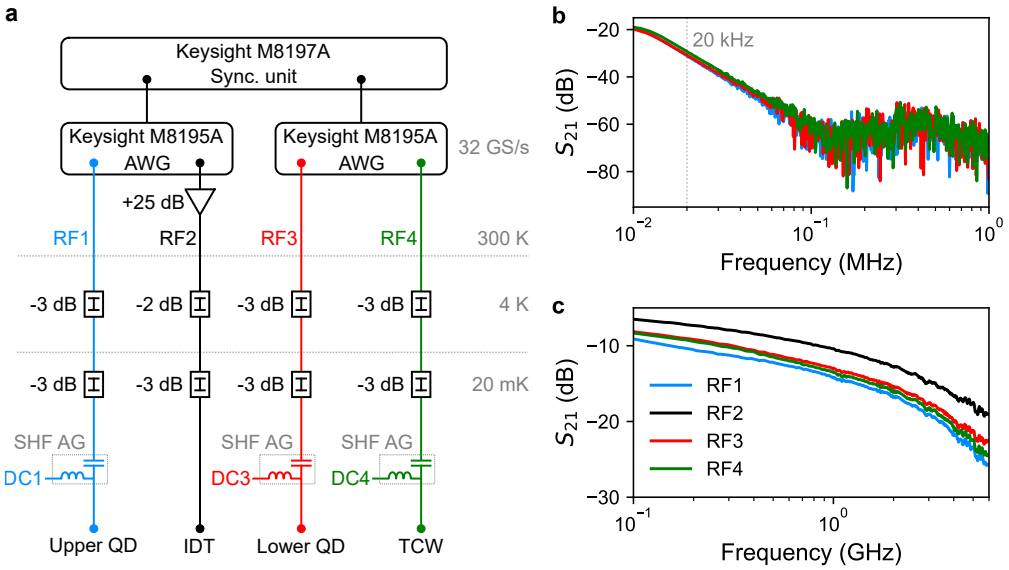

Figure C.19: RF setup of the cryostat. (a) 4 RF lines (colors) are thermalized with attenuators at 4 K and 20 mK stages. 3 broadband bias tees are employed to combine DC and RF signals. A pair of synchronized arbitrary waveform generators (AWG) provides the sub-nanosecond voltage pulses. The signal on the IDT (RF2) is enhanced with a high-power amplifier (ZHL-4W-422+) at room temperature. **(b)** Transmission S_{21} from the DC input port to the bottom SMP connector via the bias tee for the RF1 (blue), RF3 (red) and RF4 (green). The cut-off frequency is indicated at 20 kHz. **(c)** Transmission measurements from the top of the RF line to the bottom.

D Related to collision experiments

D.1 Bunching and antibunching statistics

In a Hong-Ou-Mandel (HOM) setup, the quantum nature of the incident particles determines the interference outcome. We derive in the following the expected output probabilities P_{20} (two particles at the lower detector), P_{11} (one particle at each detector) and P_{02} (two particles at the upper detector). We assume that two incoming particles injected from inputs a and b arrive simultaneously ($\tau = 0$) at a 50:50 beam splitter. After scattering, they exit to the outputs c and d.

Let us consider first the classical case where the particles do not interact with each other. In this context, the output statistics follows the Poisson distribution. The probability to find k particles at one detector is simply the ratio between

the possible scenarios $C(n,k)$ given n particles in the system, and all possible combinations 2^n:

$$P(n,k) = \frac{C(n,k)}{2^n} = \frac{n!}{k!(n-k)!}\frac{1}{2^n} \tag{D.68}$$

For $n = 2$, the final probabilities from classical statistics are then:

$$P_{20} = P(2,0) = 1/4 \tag{D.69}$$
$$P_{11} = P(2,1) = 1/2 \tag{D.70}$$
$$P_{02} = P(2,2) = 1/4 \tag{D.71}$$

When quantum statistics play a dominant role, we can express the initial state as

$$|1,1\rangle_{a,b} = \hat{a}^\dagger \hat{b}^\dagger |0,0\rangle_{a,b} \tag{D.72}$$

where $\hat{a}^\dagger$ and $\hat{b}^\dagger$ are the creation operators for the states a and b. The influence of a 50:50 beam splitter can be included as follows

$$\begin{pmatrix} \hat{a}^\dagger \\ \hat{b}^\dagger \end{pmatrix} \rightarrow \frac{1}{\sqrt{2}} \begin{pmatrix} 1 & 1 \\ 1 & -1 \end{pmatrix} \begin{pmatrix} \hat{c}^\dagger \\ \hat{d}^\dagger \end{pmatrix}. \tag{D.73}$$

Substituting the above expression into equation D.72, we find the final state

$$|1,1\rangle_{a,b} \rightarrow \frac{1}{2}(\hat{c}^\dagger + \hat{d}^\dagger)(\hat{c}^\dagger - \hat{d}^\dagger)\,|0,0\rangle_{c,d}\,. \tag{D.74}$$

Owing to the bosonic commutator relations

$$[\hat{b}_i, \hat{b}_j^\dagger] = \hat{b}_i \hat{b}_j^\dagger - \hat{b}_j^\dagger \hat{b}_i = \delta_{ij} \tag{D.75}$$
$$[\hat{b}_i, \hat{b}_j] = [\hat{b}_i^\dagger, \hat{b}_j^\dagger] = 0, \tag{D.76}$$

and the fermionic anticonmmutator relations

$$\{\hat{f}_i, \hat{f}_j^\dagger\} = \hat{f}_i \hat{f}_j^\dagger + \hat{f}_j^\dagger \hat{f}_i = \delta_{ij} \tag{D.77}$$
$$\{\hat{f}_i, \hat{f}_j\} = \{\hat{f}_i^\dagger, \hat{f}_j^\dagger\} = 0, \tag{D.78}$$

it is easy to find the output states for

$$\text{bosons} \rightarrow \frac{1}{2}|2,0\rangle + \frac{1}{2}|0,2\rangle \tag{D.79}$$
$$\text{fermions} \rightarrow |1,1\rangle \tag{D.80}$$

where the coefficients indicate the final probabilities.

D.2 Effective detuning dependence on barrier height

To investigate the effect of the barrier height in the TCW, we analyze the in-flight-partitioning data of two electrons that are sent simultaneously from the upper and lower source QDs. Figure D.20a shows the effective detuning δ extracted from in-flight-partitioning data for three different barrier-gate voltages V_B. The solid line shows a linear fit providing δ for the Bayesian model. Figure D.20b shows simulations of the maximum antibunching probability P_{11} using the Bayesian model as a function of V_B. The data points from experiment are shown as reference. Note that in the simulations σ and Δ_S are taken from single-electron partitioning measurements (see Fig. 5.5 in Section 5.1), so that δ is the only free parameter. Assuming a constant δ (dashed lines), the simulated results either over- or under-estimate P_{11}. Using however the dependency extracted from a linear square fit from Fig. D.20a (red line), the model shows a remarkable agreement over the whole voltage range.

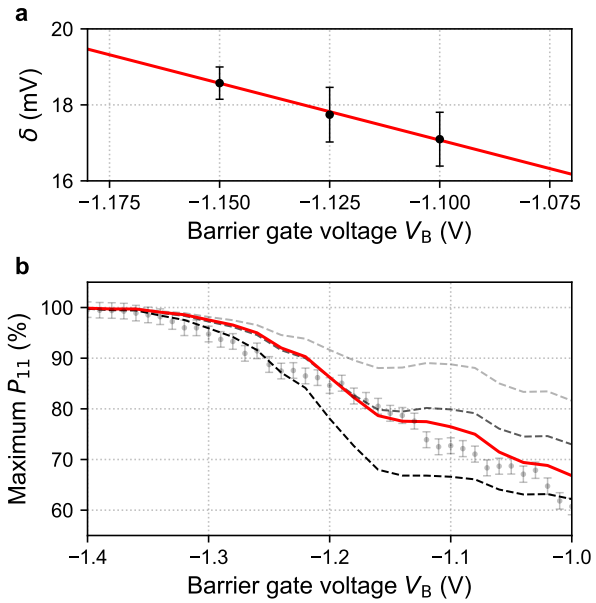

Figure D.20: Extraction of effective detuning. Detuning δ extracted from a fit with Bayesian model of two-electron-partitioning data for different barrier voltages V_B. The data points follows a linear function with slope ≈ -30 mV/V. **(b)** Simulated traces of the maximum antibunching probability P_{11} with experimental data points as reference. Dashed lines are obtained considering constant $\delta \in [10, 20, 30]$ mV (from black to grey). The red line shows the expected course by using the δ-dependency extracted from (a).

D.3 SAW confinement in electron partitioning

To investigate the effect of the confinement along the SAW propagation direction on the collision experiments, we first measure single-electron partitioning at various input power P on the IDT as reference. Figure D.21a shows the evolution of Δ_S as a function of P. The missing points around $P \approx 27$ dBm are removed due to bad calibration of the trigger-send pulse, *i.e.* no electron sent, for this SAW-power range. We find that there is only a slight deviation at the

high-power regime $P > 26$ dBm. In contrast, the transition width σ remains similar as shown in Fig. D.21b, and hence electrons have similar excitation independent on the injection side. These results indicate that, in this power range, SAW confinement has almost no influence on the single-electron partitioning.

Next, we perform the same experiment, but with two electrons. Figure D.21c shows the maximum antibunching probability P_{11} extracted from the partitioning of an electron pair. We observe a slope change in the linear dependency that we attribute to the 95 %-confinement threshold. The antibunching rate ΔP shown in Fig. 5.10a is the excess of P_{11} compared to the reference non-interacting (semi-transparent) case. Finally, to extract the effective detuning δ shown in Fig. 5.10b, we employ the Bayesian model to reproduce the course of ΔP_{11} where δ is the only fitting parameter.

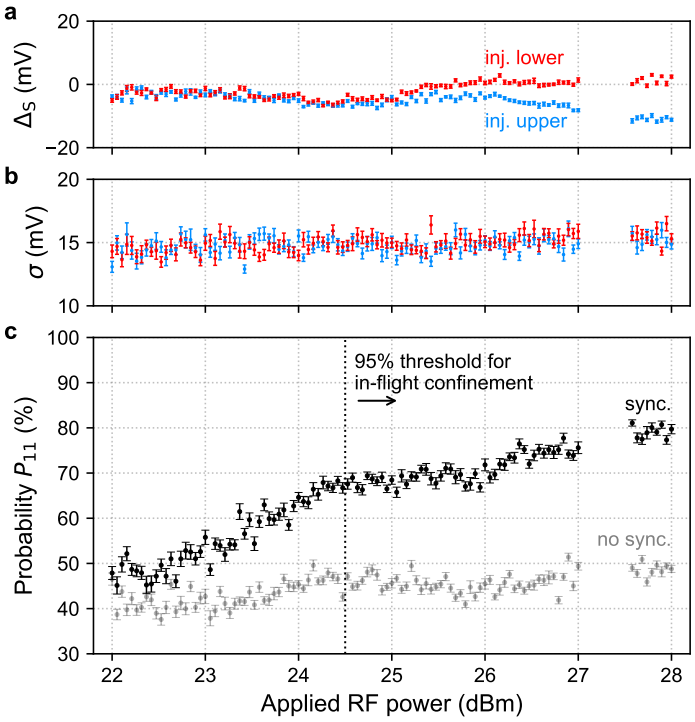

Figure D.21: Effect of SAW amplitude. Dependency on the applied input power P on the transducer for **(a)** the half-transmission position Δ_S and **(b)** the transition width σ extracted from fitting a Fermi function to a single-electron-partitioning data for an electron sent from the upper (blue) or the lower (red) source QD. **(c)** Maximum probability P_{11} extracted from the in-flight partitioning of two electrons with (black) and without (semi-transparent) synchronized transport.

D.4 Independent parameters on antibunching rate

In the following, we present our investigations on the probabilities P_{20}, P_{11}, P_{02} as a function of the potential minimum within the SAW train (see Fig. D.22) and the exit potential (see Fig. D.23). We find that the collision process does not depend on those parameters.

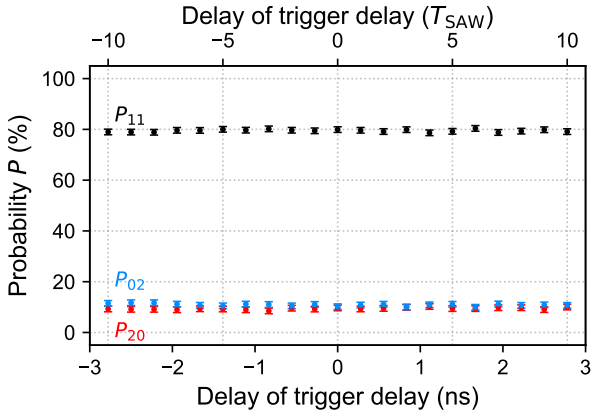

Figure D.22: Antibunching within SAW train. Transfer probabilities P_{20}, P_{11} and P_{02} where two electrons are transported together in different SAW minima. The voltage configuration of the TCW is $V_B = -1.15$ V and $V_U = V_L = -1.00$ V.

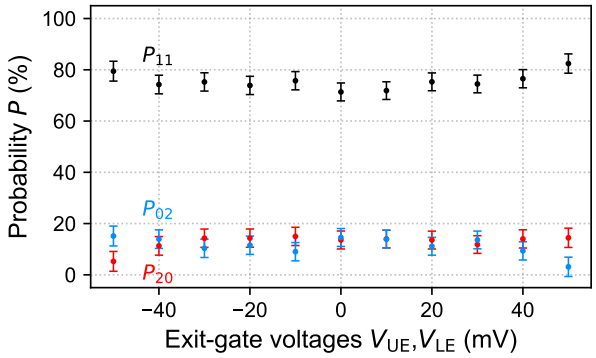

Figure D.23: TCW exit potential. Collision probabilities P_{20}, P_{11} and P_{02} for synchronized transport of a electron pair as a function of the exit potential of the coupling region controlled via voltages on the upper V_{UE} and the lower V_{LE} external surface-gates of the transport paths to the detectors (green gates in Fig. 4.2).

D.5 Partitioning of three electrons

We aim to observe signatures of Pauli exclusion principle in the collision experiments. Here, we send a total of three electrons towards the coupling region. The lower source provides a single-electron while a pair of electrons is sent together from the upper source. Figure D.24 shows the partitioning probabilities for the three-electrons synchronized transport (solid). When the electron injected from the lower source is sent at different SAW minimum (semi-transparent), we observe an asymmetry $P_{21} \neq P_{12}$ as expected. In the perfectly synchronized case, the partitioning data is fully symmetric with maximum $P_{21} = P_{12} \approx 70$ %. If

no interaction is present, we can evaluate from classical probabilities (see equation D.68) $P_{21} = P_{12} = 37.5$ %. The excess in the antibunching probability confirms the presence of electron-electron interaction.

In order to verify that Coulomb repulsion is the dominant mechanism, we would need to extend the Bayesian model to three electrons and perform realistic potential simulations. However, we have not performed such exhaustive analysis yet.

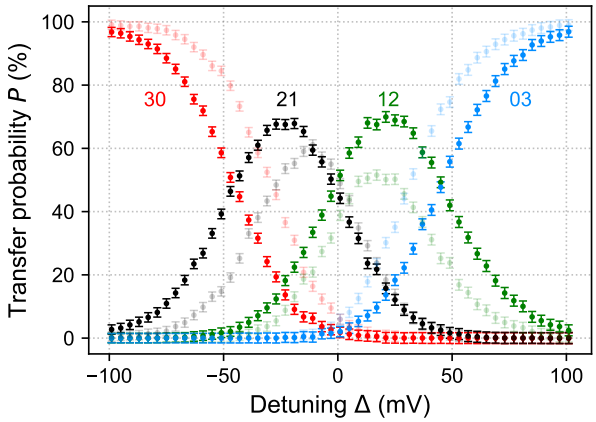

Figure D.24: Partitioning of three electrons. In-flight partitioning probabilities with three electrons. The upper QD provides two electrons together while the lower source sends an electron in the same (solid) or different (semi-transparent) SAW minima.

E Related to chirp IDT

E.1 Design of broadband SAW detector

Thanks to the inverse piezoelectric effect, when a SAW passes through another IDT, an electric signal is induced that can be recorded by a fast sampling oscilloscope. To optimize the response of the detector IDT, it is necessary to design the transducer according to the expected bandwidth of the input signal.

Generally, the response $h(t)$ of a regular IDT with N unit cells and resonant frequency f_0 is equivalent to modulating $\sin(2\pi f_0 t)$ with a rectangular function defined in the interval $0 \leq t \leq N/f_0$. Therefore, the frequency response $h(f)$ follows approximately a sinc function [Mor07]:

$$H(f) \propto \frac{\sin\left(\pi N(f - f_0)/f_0\right)}{\pi N(f - f_0)/f_0} \tag{E.81}$$

Then the characteristic bandwidth can be derived as $B = f_0/N$.

To maximize the detection sensitivity, we minimize the number of detector electrodes to one, giving $N = 1.5$ with a pair of neighboring grounded fingers. Figure E.25 shows the pass band for this geometry as function of f_0. In order

to resolve reliably the SAW response at particularly 3 GHz and below, we have chosen a detector periodicity of $\lambda_0 = 1$ µm ($f_0 \approx 2.83$ GHz).

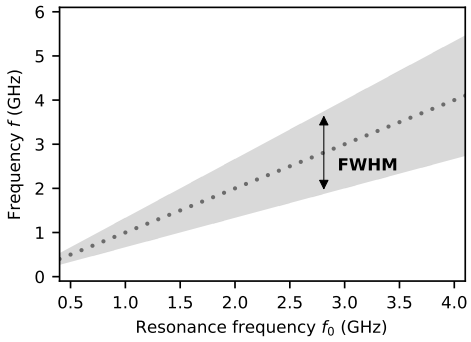

Figure E.25: Detection bandwidth. Pass band of a regular IDT with $N = 1.5$. The shaded area indicates the bandwidth of the transmission peak. The vertical double-headed arrow indicates the employed resonance frequency of the detector IDT, $f_0 \approx 2.83$ GHz.

E.2 Derivation of exponential frequency modulation

In order to have in-phase interference of the N elementary waves at the IDT's boundary, the input signal $f(t)$ must introduce the nth elementary SAW with the right delay, t_n. For an evenly spaced set of frequencies (equation 58) with a single period per step n, we obtain the excitation times:

$$t_n = \sum_{m=1}^{n} \frac{1}{f_m} \tag{E.82}$$

The resulting sum can then be expressed in terms of the digamma function Ψ:

$$t_n = \sum_{m=1}^{n} \frac{1}{f_1 + (m-1)\cdot\Delta f} = \frac{\Psi\left(\frac{f_1}{\Delta f} + n\right) - \Psi\left(\frac{f_1}{\Delta f}\right)}{\Delta f} \tag{E.83}$$

Being $f_1/\Delta f \gg 1$, this function approaches a logarithmic course:

$$\Psi(x) \overset{x\gg 1}{\approx} \ln(x) \tag{E.84}$$

Multiplying equation E.83 with Δf and applying additionally an exponential function, we thus obtain:

$$e^{\Delta f \cdot t_n} = (\underbrace{f_1 + (n-1)\cdot\Delta f}_{f_n} + \Delta f)/f_1 \tag{E.85}$$

What brings us to the desired frequency modulation of the input signal:

$$f_n = f_1 \cdot e^{\Delta f \cdot t_n} - \Delta f \overset{f_1 \gg \Delta f}{\approx} f_1 \cdot e^{\Delta f \cdot t_n} \tag{E.86}$$

as expressed in its continuous form $f(t)$ in equation 60.

E.3 Amplitude comparison of chirped pulse

Let us estimate the amplitude of the chirped pulse employed in this work with the SAW stemming from the regular IDT employed in the time-of-flight measurements reported in a previous work [Edl21]. Such comparison is valid, since the chirped pulse experiment was conducted under the same experimental conditions of the flight-time measurement – same fabrication and measurement setup. The regular IDT consists of $N = 111$ cells of period $\lambda_0 = 1$ µm. The resonance frequency that we expect for this reference IDT is $f_0 = v_{\mathrm{SAW}}/\lambda_0 \approx 2.81$ GHz. Figure 3.6 shows time-dependent measurements of a SAW train emitted from the regular transducer with a resonant input signal of duration $t_{\mathrm{Sig.}} \approx t_{\mathrm{IDT}}$. This measurement is executed under the same conditions at ambient temperature than the chirp synthesis shown in Fig. 7.4. The data shows that the chirp signal reaches approximately 80 % of the signal stemming from the SAW train of the regular IDT.

Bibliography

[Abb16] B. Abbott et al. "GW151226: Observation of Gravitational Waves from a 22-Solar-Mass Binary Black Hole Coalescence." In: *Physical Review Letters* 116.24 (2016), p. 241103. DOI: 10.1103/physrevlett.116.241103.

[ASY15] M. K. Akhlaghi, E. Schelew, and J. F. Young. "Waveguide integrated superconducting single-photon detectors implemented as near-perfect absorbers of coherent radiation." In: *Nature Communications* 6.1 (2015). DOI: 10.1038/ncomms9233.

[And09] T. Andlauer. "Optoelectronic and spin-related properties of semiconductor nanostructures in magnetic fields." PhD thesis. München: Technische Universität München, 2009.

[Aru19] F. Arute et al. "Quantum supremacy using a programmable superconducting processor." In: *Nature* 574.7779 (2019), pp. 505–510. DOI: 10.1038/s41586-019-1666-5.

[Ast08] M. Astley. "Surface-acoustic-wave-defined dynamic quantum dots." PhD thesis. 2008. DOI: 10.17863/CAM.7208.

[Axl18] C. J. Axline et al. "On-demand quantum state transfer and entanglement between remote microwave cavity memories." In: *Nature Physics* 14.7 (2018), pp. 705–710. DOI: 10.1038/s41567-018-0115-y.

[Bar56] J. Bardeen. *Semiconductor Research Leading to the Point Contact Transistor*. Nobel Lecture. 1956. URL: https://www.nobelprize.org/prizes/physics/1956/bardeen/lecture.

[BSR00] C. H. W. Barnes, J. M. Shilton, and A. M. Robinson. "Quantum computation using electrons trapped by surface acoustic waves." In: *Physical Review B* 62.12 (2000), pp. 8410–8419. DOI: 10.1103/physrevb.62.8410.

[Bar20] H. Bartolomei et al. "Fractional statistics in anyon collisions." In: *Science* 368.6487 (2020), pp. 173–177. DOI: 10.1126/science.aaz5601.

[Bar21] S. Bartolucci et al. *Fusion-based quantum computation*. 2021. DOI: 10.48550/ARXIV.2101.09310.

[Bel19] L. Bellentani et al. “Coulomb and exchange interaction effects on the exact two-electron dynamics in the Hong-Ou-Mandel interferometer based on Hall edge states.” In: *Physical Review B* 99.24 (2019), p. 245415. DOI: 10.1103/physrevb.99.245415.

[Ber00] A. Bertoni et al. “Quantum Logic Gates based on Coherent Electron Transport in Quantum Wires.” In: *Physical Review Letters* 84.25 (2000), pp. 5912–5915. DOI: 10.1103/physrevlett.84.5912.

[Ber16] B. Bertrand et al. “Fast spin information transfer between distant quantum dots using individual electrons.” In: *Nature Nanotechnology* 11.8 (2016), pp. 672–676. DOI: 10.1038/nnano.2016.82.

[Beu06] J. Beugnon et al. “Quantum interference between two single photons emitted by independently trapped atoms.” In: *Nature* 440.7085 (2006), pp. 779–782. ISSN: 1476-4687. DOI: 10.1038/nature04628. URL: https://doi.org/10.1038/nature04628.

[Bie19] A. Bienfait et al. “Phonon-mediated quantum state transfer and remote qubit entanglement.” In: *Science* 364.6438 (2019), pp. 368–371. DOI: 10.1126/science.aaw8415.

[Bie20] A. Bienfait et al. “Quantum Erasure Using Entangled Surface Acoustic Phonons.” In: *Phys. Rev. X* 10 (2 2020), p. 021055. DOI: 10.1103/PhysRevX.10.021055. URL: https://link.aps.org/doi/10.1103/PhysRevX.10.021055.

[Bir07] S. Birner et al. “nextnano: General Purpose 3-D Simulations.” In: *IEEE Transactions on Electron Devices* 54.9 (2007), pp. 2137–2142. DOI: 10.1109/ted.2007.902871.

[BE11] M. Blazek and W. Elsäßer. “Coherent and thermal light: Tunable hybrid states with second-order coherence without first-order coherence.” In: *Physical Review A* 84.6 (2011), p. 063840. DOI: 10.1103/physreva.84.063840.

[Blu07] M. D. Blumenthal et al. “Gigahertz quantized charge pumping.” In: *Nature Physics* 3.5 (2007), pp. 343–347. DOI: 10.1038/nphys582.

[Boc13] E. Bocquillon et al. “Coherence and Indistinguishability of Single Electrons Emitted by Independent Sources.” In: *Science* 339.6123 (2013), pp. 1054–1057. DOI: 10.1126/science.1232572.

[Bra56] W. H. Brattain. *Surface Properties of Semiconductors*. Nobel Lecture. 1956. URL: https://www.nobelprize.org/prizes/physics/1956/brattain/lecture/.

[BL05] S. L. Braunstein and P. van Loock. “Quantum information with continuous variables.” In: *Reviews of Modern Physics* 77.2 (2005), pp. 513–577. DOI: 10.1103/revmodphys.77.513.

[HBT56] R. H. Brown and R. Q. Twiss. "Correlation between Photons in two Coherent Beams of Light." In: *Nature* 177.4497 (1956), pp. 27–29. DOI: 10.1038/177027a0.

[Bru96] M. Brune et al. "Quantum Rabi Oscillation: A Direct Test of Field Quantization in a Cavity." In: *Physical Review Letters* 76.11 (1996), pp. 1800–1803. DOI: 10.1103/physrevlett.76.1800.

[Bäu18] C. Bäuerle et al. "Coherent control of single electrons: a review of current progress." In: *Reports on Progress in Physics* 81.5 (2018), p. 056503. DOI: 10.1088/1361-6633/aaa98a.

[Gla20] G. D. C. et al. *Design of a Single-Shot Electron detector with sub-electron sensitivity for electron flying qubit operation*. 2020. DOI: 10.48550/ARXIV.2002.03947.

[Car15] J. Carolan et al. "Universal linear optics." In: *Science* 349.6249 (2015), pp. 711–716. DOI: 10.1126/science.aab3642.

[Cha22] E. Chatzikyriakou et al. "Unveiling the charge distribution of a GaAs-based nanoelectronic device: A large experimental data-set approach." In: (2022). DOI: 10.48550/ARXIV.2205.00846.

[Che21] F. Chen et al. "Strain-induced Megahertz Oscillation and Stable Velocity of an Antiferromagnetic Domain Wall." In: *Physical Review Applied* 15.1 (2021), p. 014030. DOI: 10.1103/physrevapplied.15.014030.

[Cif09] O. Ciftja. "Classical behavior of few-electron parabolic quantum dots." In: *Physica B: Condensed Matter* 404.12-13 (2009), pp. 1629–1631. DOI: 10.1016/j.physb.2009.01.036.

[CS65] A. M. Cowley and S. M. Sze. "Surface States and Barrier Height of Metal-Semiconductor Systems." In: *Journal of Applied Physics* 36.10 (1965), pp. 3212–3220. DOI: 10.1063/1.1702952.

[Del19] P. Delsing et al. "The 2019 surface acoustic waves roadmap." In: *Journal of Physics D: Applied Physics* 52.35 (2019), p. 353001. DOI: 10.1088/1361-6463/ab1b04.

[DWM04] M. H. Devoret, A. Wallraff, and J. M. Martinis. *Superconducting Qubits: A Short Review*. 2004. DOI: 10.48550/ARXIV.COND-MAT/0411174.

[Din16] X. Ding et al. "On-Demand Single Photons with High Extraction Efficiency and Near-Unity Indistinguishability from a Resonantly Driven Quantum Dot in a Micropillar." In: *Physical Review Letters* 116.2 (2016), p. 020401. DOI: 10.1103/physrevlett.116.020401.

[DiV00] D. P. DiVincenzo. "The Physical Implementation of Quantum Computation." In: *Fortschritte der Physik* 48.9-11 (2000), pp. 771–783. DOI: https://doi.org/10.1002/1521-3978(200009)48:9/11<771::AID-PROP771>3.0.CO;2-E.

[DM03] J. P. Dowling and G. J. Milburn. "Quantum technology: the second quantum revolution." In: *Philosophical Transactions of the Royal Society of London. Series A: Mathematical, Physical and Engineering Sciences* 361.1809 (2003). Ed. by A. G. J. MacFarlane, pp. 1655–1674. DOI: 10.1098/rsta.2003.1227.

[Dub13] J. Dubois et al. "Minimal-excitation states for electron quantum optics using levitons." In: *Nature* 502.7473 (2013), pp. 659–663. DOI: 10.1038/nature12713.

[Dum19] É. Dumur et al. "Unidirectional distributed acoustic reflection transducers for quantum applications." In: *Applied Physics Letters* 114.22 (2019), p. 223501. DOI: 10.1063/1.5099095.

[Dut07] M. V. G. Dutt et al. "Quantum Register Based on Individual Electronic and Nuclear Spin Qubits in Diamond." In: *Science* 316.5829 (2007), pp. 1312–1316. DOI: 10.1126/science.1139831.

[Edl19] H. Edlbauer. "Electron-quantum-optics experiments at the single particle level." PhD thesis. 2019. URL: http://www.theses.fr/2019GREAY027.

[Edl17] H. Edlbauer et al. "Non-universal transmission phase behaviour of a large quantum dot." In: *Nature Communications* 8.1 (2017). DOI: 10.1038/s41467-017-01685-z.

[Edl21] H. Edlbauer et al. "In-flight distribution of an electron within a surface acoustic wave." In: *Applied Physics Letters* 119.11 (2021), p. 114004. DOI: 10.1063/5.0062491.

[Edl22] H. Edlbauer et al. "Semiconductor-based electron flying qubits: review on recent progress accelerated by numerical modelling." In: *EPJ Quantum Technology* 9.1 (2022). DOI: 10.1140/epjqt/s40507-022-00139-w.

[EBB71] A. B. Einstein, M. Born, and H. Born. "The Born-Einstein letters: Correspondence between Albert Einstein and Max and Hedwig Born from 1916-1955, with commentaries by Max Born;" in: 1971.

[Eks17] M. K. Ekström et al. "Surface acoustic wave unidirectional transducers for quantum applications." In: *Applied Physics Letters* 110.7 (2017), p. 073105. DOI: 10.1063/1.4975803.

[Eng13] E. Engin et al. “Photon pair generation in a silicon micro-ring resonator with reverse bias enhancement.” In: *Optics Express* 21.23 (2013), p. 27826. DOI: 10.1364/oe.21.027826.

[FDJ08] G. Fève, P. Degiovanni, and T. Jolicoeur. “Quantum detection of electronic flying qubits in the integer quantum Hall regime.” In: *Physical Review B* 77.3 (2008), p. 035308. DOI: 10.1103/physrevb.77.035308.

[Fey82] R. P. Feynman. “Simulating physics with computers.” In: *International Journal of Theoretical Physics* 21.6-7 (1982), pp. 467–488. DOI: 10.1007/bf02650179.

[Fie93] M. Field et al. “Measurements of Coulomb blockade with a noninvasive voltage probe.” In: *Physical Review Letters* 70.9 (1993), pp. 1311–1314. DOI: 10.1103/physrevlett.70.1311.

[Fis06] S. F. Fischer et al. “Energy spectroscopy of controlled coupled quantum-wire states.” In: *Nature Physics* 2.2 (2006), pp. 91–96. DOI: 10.1038/nphys205.

[Fle13] J. D. Fletcher et al. “Clock-Controlled Emission of Single-Electron Wave Packets in a Solid-State Circuit.” In: *Physical Review Letters* 111.21 (2013), p. 216807. DOI: 10.1103/physrevlett.111.216807.

[Fle19] J. D. Fletcher et al. “Continuous-variable tomography of solitary electrons.” In: *Nature Communications* 10.1 (2019). DOI: 10.1038/s41467-019-13222-1.

[For17] C. J. B. Ford. “Transporting and manipulating single electrons in surface-acoustic-wave minima.” In: *physica status solidi (b)* 254.3 (2017), p. 1600658. DOI: https://doi.org/10.1002/pssb.201600658. eprint: https://onlinelibrary.wiley.com/doi/pdf/10.1002/pssb.201600658. URL: https://onlinelibrary.wiley.com/doi/abs/10.1002/pssb.201600658.

[Fre20] L. Freise et al. “Trapping and Counting Ballistic Nonequilibrium Electrons.” In: *Physical Review Letters* 124.12 (2020), p. 127701. DOI: 10.1103/physrevlett.124.127701.

[Fuh11] D. A. Fuhrmann et al. “Dynamic modulation of photonic crystal nanocavities using gigahertz acoustic phonons.” In: *Nature Photonics* 5.10 (2011), pp. 605–609. DOI: 10.1038/nphoton.2011.208.

[Fuj04] T. Fujisawa et al. “Rotation and phase-shift operations for a charge qubit in a double quantum dot.” In: *Physica E: Low-dimensional Systems and Nanostructures* 21.2-4 (2004), pp. 1046–1052. DOI: 10.1016/j.physe.2003.11.184.

[Fèv07] G. Fève et al. “An On-Demand Coherent Single-Electron Source.” In: *Science* 316.5828 (May 2007), pp. 1169–1172. DOI: 10.1126/science.1141243.

[GZ21] M. F. Gonzalez-Zalba et al. “Scaling silicon-based quantum computing using CMOS technology.” In: *Nature Electronics* 4.12 (2021), pp. 872–884. DOI: 10.1038/s41928-021-00681-y.

[Gro14] C. W. Groth et al. “Kwant: a software package for quantum transport.” In: *New Journal of Physics* 16.6 (2014), p. 063065. DOI: 10.1088/1367-2630/16/6/063065.

[Gro96] L. K. Grover. “A fast quantum mechanical algorithm for database search.” In: *Proceedings of the twenty-eighth annual ACM symposium on Theory of computing - STOC '96*. ACM Press, 1996. DOI: 10.1145/237814.237866.

[Han07] R. Hanson et al. “Spins in few-electron quantum dots.” In: *Reviews of Modern Physics* 79.4 (2007), pp. 1217–1265. DOI: 10.1103/revmodphys.79.1217.

[HBR73] C. Hartmann, D. Bell, and R. Rosenfeld. “Impulse Model Design of Acoustic Surface-Wave Filters.” In: *IEEE Transactions on Microwave Theory and Techniques* 21.4 (1973), pp. 162–175. DOI: 10.1109/tmtt.1973.1127967.

[Hay03] T. Hayashi et al. “Coherent Manipulation of Electronic States in a Double Quantum Dot.” In: *Physical Review Letters* 91.22 (2003), p. 226804. DOI: 10.1103/physrevlett.91.226804.

[Hen99] M. Henny et al. “The Fermionic Hanbury Brown and Twiss Experiment.” In: *Science* 284.5412 (1999), pp. 296–298. DOI: 10.1126/science.284.5412.296.

[Her11] S. Hermelin et al. “Electrons surfing on a sound wave as a platform for quantum optics with flying electrons.” In: *Nature* 477.7365 (2011), pp. 435–438. DOI: 10.1038/nature10416.

[HMLS18] A Hernández-Mínguez, Y.-T. Liou, and P. V. Santos. “Interaction of surface acoustic waves with electronic excitations in graphene.” In: *Journal of Physics D: Applied Physics* 51.38 (2018), p. 383001. DOI: 10.1088/1361-6463/aad593.

[HOM87] C. K. Hong, Z. Y. Ou, and L. Mandel. “Measurement of subpicosecond time intervals between two photons by interference.” In: *Physical Review Letters* 59.18 (1987), pp. 2044–2046. DOI: 10.1103/physrevlett.59.2044.

[Hou18] H Hou et al. “Experimental verification of electrostatic boundary conditions in gate-patterned quantum devices.” In: *Journal of Physics D: Applied Physics* 51.24 (2018), p. 244004. DOI: 10.1088/1361-6463/aac376.

[Hsi20] T.-K. Hsiao et al. “Single-photon emission from single-electron transport in a SAW-driven lateral light-emitting diode.” In: *Nature Communications* 11.1 (2020). DOI: 10.1038/s41467-020-14560-1.

[HH13] P. Huang and X. Hu. “Spin qubit relaxation in a moving quantum dot.” In: *Physical Review B* 88.7 (2013), p. 075301. DOI: 10.1103/physrevb.88.075301.

[IAU01] R. Ionicioiu, G. Amaratunga, and F. Udrea. “Quantum computation with ballistic electrons.” In: *International Journal of Modern Physics B* 15.02 (2001), pp. 125–133. DOI: 10.1142/s0217979201003521.

[Ito21] R. Ito et al. “Coherent Beam Splitting of Flying Electrons Driven by a Surface Acoustic Wave.” In: *Physical Review Letters* 126.7 (2021), p. 070501. DOI: 10.1103/physrevlett.126.070501.

[Jad21] B. Jadot et al. “Distant spin entanglement via fast and coherent electron shuttling.” In: *Nature Nanotechnology* 16.5 (2021), pp. 570–575. DOI: 10.1038/s41565-021-00846-y.

[JH00] T. Janssen and A Hartland. “Accuracy of quantized single-electron current in a one-dimensional channel.” In: *Physica B: Condensed Matter* 284-288 (2000), pp. 1790–1791. DOI: 10.1016/s0921-4526(99)02978-6.

[Ji03] Y. Ji et al. “An electronic Mach–Zehnder interferometer.” In: *Nature* 422.6930 (2003), pp. 415–418. DOI: 10.1038/nature01503.

[Jul14] T. Jullien et al. “Quantum tomography of an electron.” In: *Nature* 514.7524 (2014), pp. 603–607. DOI: 10.1038/nature13821.

[Kat09] M. Kataoka et al. “Coherent Time Evolution of a Single-Electron Wave Function.” In: *Physical Review Letters* 102.15 (2009), p. 156801. DOI: 10.1103/physrevlett.102.156801.

[KRH02] H. Kiesel, A. Renz, and F. Hasselbach. “Observation of Hanbury Brown–Twiss anticorrelations for free electrons.” In: *Nature* 418.6896 (2002), pp. 392–394. DOI: 10.1038/nature00911.

[KDP80] K. v. Klitzing, G. Dorda, and M. Pepper. “New Method for High-Accuracy Determination of the Fine-Structure Constant Based on Quantized Hall Resistance.” In: *Physical Review Letters* 45.6 (1980), pp. 494–497. DOI: 10.1103/physrevlett.45.494.

[KLM01] E. Knill, R. Laflamme, and G. J. Milburn. "A scheme for efficient quantum computation with linear optics." In: *Nature* 409.6816 (2001), pp. 46–52. DOI: 10.1038/35051009.

[Kob17] D. Kobayashi et al. "Spin Current Generation Using a Surface Acoustic Wave Generated via Spin-Rotation Coupling." In: *Physical Review Letters* 119.7 (2017), p. 077202. DOI: 10.1103/physrevlett.119.077202.

[Koc07] J. Koch et al. "Charge-insensitive qubit design derived from the Cooper pair box." In: *Physical Review A* 76.4 (2007), p. 042319. DOI: 10.1103/physreva.76.042319.

[KOT11] T. Kodama, N. Osakabe, and A. Tonomura. "Correlation in a coherent electron beam." In: *Physical Review A* 83.6 (2011), p. 063616. DOI: 10.1103/physreva.83.063616.

[Lad10] T. D. Ladd et al. "Quantum computers." In: *Nature* 464.7285 (2010), pp. 45–53. DOI: 10.1038/nature08812.

[LLL96] L. S. Levitov, H. Lee, and G. B. Lesovik. "Electron counting statistics and coherent states of electric current." In: *Journal of Mathematical Physics* 37.10 (1996), pp. 4845–4866. DOI: 10.1063/1.531672.

[Liu08] H. Liu et al. "A gate-defined silicon quantum dot molecule." In: *Applied Physics Letters* 92.22 (2008), p. 222104. DOI: 10.1063/1.2938693.

[Liu98] R. C. Liu et al. "Quantum interference in electron collision." In: *Nature* 391.6664 (1998), pp. 263–265. DOI: 10.1038/34611.

[Mąd22] M. T. Mądzik et al. "Precision tomography of a three-qubit donor quantum processor in silicon." In: *Nature* 601.7893 (Jan. 2022), pp. 348–353. DOI: 10.1038/s41586-021-04292-7.

[MAI60] T. H. MAIMAN. "Stimulated Optical Radiation in Ruby." In: *Nature* 187.4736 (1960), pp. 493–494. DOI: 10.1038/187493a0.

[Mar58] W. Markowitz et al. "Frequency of Cesium in Terms of Ephemeris Time." In: *Physical Review Letters* 1.3 (1958), pp. 105–107. DOI: 10.1103/physrevlett.1.105.

[Mau16] R. Maurand et al. "A CMOS silicon spin qubit." In: *Nature Communications* 7.1 (2016). DOI: 10.1038/ncomms13575.

[McN11] R. P. G. McNeil et al. "On-demand single-electron transfer between distant quantum dots." In: *Nature* 477.7365 (2011), pp. 439–442. DOI: 10.1038/nature10444.

[Mee96] D. M. Meekhof et al. "Generation of Nonclassical Motional States of a Trapped Atom." In: *Physical Review Letters* 76.11 (1996), pp. 1796–1799. DOI: 10.1103/physrevlett.76.1796.

[MM87] A. A. Michelson and E. W. Morley. "On the relative motion of the Earth and the luminiferous ether." In: *American Journal of Science* s3-34.203 (1887), pp. 333–345. DOI: 10.2475/ajs.s3-34.203.333.

[MSF18] L. Midolo, A. Schliesser, and A. Fiore. "Nano-opto-electro-mechanical systems." In: *Nature Nanotechnology* 13.1 (2018), pp. 11–18. DOI: 10.1038/s41565-017-0039-1.

[Mon14] C. Monroe et al. "Large-scale modular quantum-computer architecture with atomic memory and photonic interconnects." In: *Physical Review A* 89.2 (2014), p. 022317. DOI: 10.1103/physreva.89.022317.

[Mor07] D. Morgan. *Surface acoustic wave filters : with applications to electronic communications and signal processing*. Amsterdam London: Academic Press, 2007. ISBN: 9780123725370.

[MO06] O. Morsch and M. Oberthaler. "Dynamics of Bose-Einstein condensates in optical lattices." In: *Reviews of Modern Physics* 78.1 (2006), pp. 179–215. DOI: 10.1103/revmodphys.78.179.

[Naj14] F. Najafi et al. "Scalable single-photon detection on a photonic chip." In: *CLEO: 2014*. OSA, 2014. DOI: 10.1364/cleo_qels.2014.fm3a.8.

[Nak20] J. Nakamura et al. "Direct observation of anyonic braiding statistics." In: *Nature Physics* 16.9 (2020), pp. 931–936. DOI: 10.1038/s41567-020-1019-1.

[NPT99] Y. Nakamura, Y. A. Pashkin, and J. S. Tsai. "Coherent control of macroscopic quantum states in a single-Cooper-pair box." In: *Nature* 398.6730 (1999), pp. 786–788. DOI: 10.1038/19718.

[Ned07] I. Neder et al. "Interference between two indistinguishable electrons from independent sources." In: *Nature* 448.7151 (2007), pp. 333–337. DOI: 10.1038/nature05955.

[Neu08] P. Neumann et al. "Multipartite Entanglement Among Single Spins in Diamond." In: *Science* 320.5881 (2008), pp. 1326–1329. DOI: 10.1126/science.1157233.

[NC09] M. A. Nielsen and I. L. Chuang. *Quantum Computation and Quantum Information*. Cambridge University Press, 2009. DOI: 10.1017/cbo9780511976667.

[ND90] J. A. Nixon and J. H. Davies. "Potential fluctuations in heterostructure devices." In: *Physical Review B* 41.11 (1990), pp. 7929–7932. DOI: 10.1103/physrevb.41.7929.

[Noi22] A. Noiri et al. “Fast universal quantum gate above the fault-tolerance threshold in silicon.” In: *Nature* 601.7893 (2022), pp. 338–342. DOI: 10.1038/s41586-021-04182-y.

[O'B03] J. L. O'Brien et al. “Demonstration of an all-optical quantum controlled-NOT gate.” In: *Nature* 426.6964 (2003), pp. 264–267. DOI: 10.1038/nature02054.

[Oli99] W. D. Oliver et al. “Hanbury Brown and Twiss-Type Experiment with Electrons.” In: *Science* 284.5412 (1999), pp. 299–301. DOI: 10.1126/science.284.5412.299.

[Pae20] S. Paesani et al. “Near-ideal spontaneous photon sources in silicon quantum photonics.” In: *Nature Communications* 11.1 (2020). DOI: 10.1038/s41467-020-16187-8.

[Pet10] K. D. Petersson et al. “Quantum Coherence in a One-Electron Semiconductor Charge Qubit.” In: *Physical Review Letters* 105.24 (2010), p. 246804. DOI: 10.1103/physrevlett.105.246804.

[Pet05] J. R. Petta et al. “Coherent Manipulation of Coupled Electron Spins in Semiconductor Quantum Dots.” In: *Science* 309.5744 (2005), pp. 2180–2184. DOI: 10.1126/science.1116955.

[PCB21] F. Pistolesi, A. Cleland, and A. Bachtold. “Proposal for a Nanomechanical Qubit.” In: *Physical Review X* 11.3 (2021), p. 031027. DOI: 10.1103/physrevx.11.031027.

[PMO09] A. Politi, J. C. F. Matthews, and J. L. O'Brien. “Shor’s Quantum Factoring Algorithm on a Photonic Chip.” In: *Science* 325.5945 (2009), pp. 1221–1221. DOI: 10.1126/science.1173731.

[PSK19] M. Powlowski, F. Sfigakis, and N. Y. Kim. “Temperature dependent angular dispersions of surface acoustic waves on GaAs.” In: *Japanese Journal of Applied Physics* 58.3 (2019), p. 030907. DOI: 10.7567/1347-4065/ab0008.

[Rab38] I. I. Rabi et al. “A New Method of Measuring Nuclear Magnetic Moment.” In: *Physical Review* 53.4 (1938), pp. 318–318. DOI: 10.1103/physrev.53.318.

[Ray85] L. Rayleigh. “On Waves Propagated along the Plane Surface of an Elastic Solid.” In: *Proceedings of the London Mathematical Society* s1-17.1 (1885), pp. 4–11. DOI: 10.1112/plms/s1-17.1.4.

[Rez16] A. R. Rezk et al. “Acoustically-Driven Trion and Exciton Modulation in Piezoelectric Two-Dimensional MoS_2.” In: *Nano Letters* 16.2 (2016), pp. 849–855. DOI: 10.1021/acs.nanolett.5b02826.

[San18] R. Santagati et al. "Witnessing eigenstates for quantum simulation of Hamiltonian spectra." In: *Science Advances* 4.1 (2018). DOI: 10.1126/sciadv.aap9646.

[San02] C. Santori et al. "Indistinguishable photons from a single-photon device." In: *Nature* 419.6907 (2002), pp. 594–597. DOI: 10.1038/nature01086.

[Sat18] K. J. Satzinger et al. "Quantum control of surface acoustic-wave phonons." In: *Nature* 563.7733 (2018), pp. 661–665. DOI: 10.1038/s41586-018-0719-5.

[Sch15a] M. Schuetz et al. "Universal Quantum Transducers Based on Surface Acoustic Waves." In: *Physical Review X* 5.3 (2015), p. 031031. DOI: 10.1103/physrevx.5.031031.

[Sch97] R. Schuster et al. "Phase measurement in a quantum dot via a double-slit interference experiment." In: *Nature* 385.6615 (1997), pp. 417–420. DOI: 10.1038/385417a0.

[Sch15b] F. J. R. Schülein et al. "Fourier synthesis of radiofrequency nanomechanical pulses with different shapes." In: *Nature Nanotechnology* 10.6 (2015), pp. 512–516. DOI: 10.1038/nnano.2015.72.

[Shi96] J. M. Shilton et al. "High-frequency single-electron transport in a quasi-one-dimensional GaAs channel induced by surface acoustic waves." In: *Journal of Physics: Condensed Matter* 8.38 (1996), pp. L531–L539. DOI: 10.1088/0953-8984/8/38/001.

[Sho56] W. B. Shockley. *Transistor Technology Evokes New Physics*. Nobel Lecture. 1956. URL: https://www.nobelprize.org/prizes/physics/1956/shockley/lecture/.

[Sho94] P. Shor. "Algorithms for quantum computation: discrete logarithms and factoring." In: *Proceedings 35th Annual Symposium on Foundations of Computer Science*. IEEE Comput. Soc. Press, 1994. DOI: 10.1109/sfcs.1994.365700.

[Sim09] C. B. Simmons et al. "Charge Sensing and Controllable Tunnel Coupling in a Si/SiGe Double Quantum Dot." In: *Nano Letters* 9.9 (2009), pp. 3234–3238. DOI: 10.1021/nl9014974.

[Smi69a] W. Smith et al. "Analysis of Interdigital Surface Wave Transducers by Use of an Equivalent Circuit Model." In: *IEEE Transactions on Microwave Theory and Techniques* 17.11 (1969), pp. 856–864. DOI: 10.1109/tmtt.1969.1127075.

[Smi69b] W. Smith et al. “Design of Surface Wave Delay Lines with Interdigital Transducers.” In: *IEEE Transactions on Microwave Theory and Techniques* 17.11 (1969), pp. 865–873. DOI: 10.1109/tmtt.1969.1127076.

[Som16] N. Somaschi et al. “Near-optimal single-photon sources in the solid state.” In: *Nature Photonics* 10.5 (2016), pp. 340–345. DOI: 10.1038/nphoton.2016.23.

[Son21] M. M. Sonner et al. “Ultrafast electron cycloids driven by the transverse spin of a surface acoustic wave.” In: *Science Advances* 7.31 (2021). DOI: 10.1126/sciadv.abf7414.

[SM85] D. Strickland and G. Mourou. “Compression of amplified chirped optical pulses.” In: *Optics Communications* 56.3 (1985), pp. 219–221. DOI: 10.1016/0030-4018(85)90120-8.

[SN06] S. Sze and K. K. Ng. *Physics of Semiconductor Devices*. John Wiley & Sons, Inc., 2006. DOI: 10.1002/0470068329.

[Tak14] S. Takada et al. “Transmission Phase in the Kondo Regime Revealed in a Two-Path Interferometer.” In: *Physical Review Letters* 113.12 (2014), p. 126601. DOI: 10.1103/physrevlett.113.126601.

[Tak15] S. Takada et al. “Measurement of the transmission phase of an electron in a quantum two-path interferometer.” In: *Applied Physics Letters* 107.6 (2015), p. 063101. DOI: 10.1063/1.4928035.

[Tak19] S. Takada et al. “Sound-driven single-electron transfer in a circuit of coupled quantum rails.” In: *Nature Communications* 10.1 (2019). DOI: 10.1038/s41467-019-12514-w.

[TH71] R. Tancrell and M. Holland. “Acoustic surface wave filters.” In: *Proceedings of the IEEE* 59.3 (1971), pp. 393–409. DOI: 10.1109/proc.1971.8180.

[Ubb14] N. Ubbelohde et al. “Partitioning of on-demand electron pairs.” In: *Nature Nanotechnology* 10.1 (2014), pp. 46–49. DOI: 10.1038/nnano.2014.275.

[Wan20] N. H. Wan et al. “Large-scale integration of artificial atoms in hybrid photonic circuits.” In: *Nature* 583.7815 (2020), pp. 226–231. DOI: 10.1038/s41586-020-2441-3.

[Wan22a] J. Wang. “Coulomb-mediated antibunching of an electron pair surfing on sound.” (To be published). 2022.

[Wan22b] J. Wang et al. “Generation of a Single-Cycle Acoustic Pulse: A Scalable Solution for Transport in Single-Electron Circuits.” In: *Physical Review X* 12.3 (2022), p. 031035. DOI: 10.1103/physrevx.12.031035.

[Wee88] B. J. van Wees et al. “Quantized conductance of point contacts in a two-dimensional electron gas.” In: *Physical Review Letters* 60.9 (1988), pp. 848–850. DOI: 10.1103/physrevlett.60.848.

[Wei18] M. Weiß et al. “Multiharmonic Frequency-Chirped Transducers for Surface-Acoustic-Wave Optomechanics.” In: *Physical Review Applied* 9.1 (2018), p. 014004. DOI: 10.1103/physrevapplied.9.014004.

[WV65] R. M. White and F. W. Voltmer. “Direct piezoelectric coupling to surface elastic waves.” In: *Applied Physics Letters* 7.12 (1965), pp. 314–316. DOI: 10.1063/1.1754276.

[Win98] D. Wineland et al. “Experimental issues in coherent quantum-state manipulation of trapped atomic ions.” In: *Journal of Research of the National Institute of Standards and Technology* 103.3 (1998), p. 259. DOI: 10.6028/jres.103.019.

[WKW86] A. Wixforth, J. P. Kotthaus, and G. Weimann. “Quantum Oscillations in the Surface-Acoustic-Wave Attenuation Caused by a Two-Dimensional Electron System.” In: *Physical Review Letters* 56.19 (1986), pp. 2104–2106. DOI: 10.1103/physrevlett.56.2104.

[Wri19] K. Wright et al. “Benchmarking an 11-qubit quantum computer.” In: *Nature Communications* 10.1 (2019). DOI: 10.1038/s41467-019-13534-2.

[Xue22] X. Xue et al. “Quantum logic with spin qubits crossing the surface code threshold.” In: *Nature* 601.7893 (2022), pp. 343–347. DOI: 10.1038/s41586-021-04273-w.

[Yac95] A. Yacoby et al. “Coherence and Phase Sensitive Measurements in a Quantum Dot.” In: *Physical Review Letters* 74.20 (1995), pp. 4047–4050. DOI: 10.1103/physrevlett.74.4047.

[Yam12] M. Yamamoto et al. “Electrical control of a solid-state flying qubit.” In: *Nature Nanotechnology* 7.4 (2012), pp. 247–251. DOI: 10.1038/nnano.2012.28.

[Yok20a] M. Yokoi et al. “Negative resistance state in superconducting NbSe 2 induced by surface acoustic waves.” In: *Science Advances* 6.34 (2020). DOI: 10.1126/sciadv.aba1377.

[Yok20b] T. Yokouchi et al. “Creation of magnetic skyrmions by surface acoustic waves.” In: *Nature Nanotechnology* 15.5 (2020), pp. 361–366. DOI: 10.1038/s41565-020-0661-1.

[Zho19] Y. P. Zhong et al. “Violating Bell’s inequality with remotely connected superconducting qubits.” In: *Nature Physics* 15.8 (2019), pp. 741–744. DOI: 10.1038/s41567-019-0507-7.

[Zho21] Y. Zhong et al. “Deterministic multi-qubit entanglement in a quantum network.” In: *Nature* 590.7847 (2021), pp. 571–575. DOI: 10.1038/s41586-021-03288-7.

[Zwa13] F. A. Zwanenburg et al. “Silicon quantum electronics.” In: *Reviews of Modern Physics* 85.3 (2013), pp. 961–1019. DOI: 10.1103/revmodphys.85.961.

Acknowledgements

As Sir Isaac Newton said once: "If I have seen further than others, it is by standing upon the shoulders of giants". The success of my PhD was only possible because of the help from countless extraordinary people.

First of all, my sincerest thanks to Chris. For me, I could not have asked for a better supervisor. From the beginning, when I was just an internship student, you gave me the freedom to experiment with new ideas while providing me with all the resources I asked for. I deeply appreciated that you always made yourself available for discussions as well as dealing with technical problems. In addition, you were not only a role model professionally, but your discipline in exercising regularly was a source of inspiration. In short, you have had a huge influence on the person I am today.

Shintaro and Hermann, you have been essential to my experimental work. Thank you for the time you spent teaching me all the technical details. Furthermore, I was always amazed by the number of new ideas generated after each of our discussions. It was simply a pleasure to work with you.

Institut Néel is fortunate to have a wide range of competent technicians. In particular, I would like to underline the essential role of Thierry Crozes, who maintains one of the most important machines of the institute: the electron beam. Thanks to your help, I was able to identify the bottlenecks in my processes, which allowed me to reach an almost perfect nanofabrication yield. Similarly, my sincere gratitude to Pierrer Perrier, whose custom-made pieces are almost artistic.

I have a special feeling for the chirp project because it started during my master internship. Pierre-André and Baptiste, thank you for training me and putting me in charge on this project despite my inexperience. On the other hand, Shunsuke, your ability to learn quickly and your hard work have taken this technique to a new level. I have no doubt that you will have a successful career in the future.

All experimentalists need support from theoreticians. Thank you Xavier for all the discussions, fresh ideas and your contagious enthusiasm. I would like to also thank Eleni for your extensive work on the simulation model. I hope the best for your next position.

During my PhD, I had the great pleasure to spend two months at nextnano GmbH. Stefan, your warmth and kindness made me feel at home from my first day. Not only did you let me work on my own ideas, but you were also willing to discuss business matters. Moreover, my stay would not have been the same

without the other members of this little family (Carola, Alex, Maria, Thomas, Kemal).

I would also like to thank all the jury members for their careful evaluation of this manuscript and my work.

Having a healthy mental state was essential to my working efficiency. For this, I am extremely grateful to the vast number of extraordinary people who surrounded me inside and outside the laboratory. Since I do not have an infinite number of pages, I will try to be brief and concise. Alvarito and David Wander, simply the best collocs I could ever asked for. David Niegemann, an inspiring role model about hard work and perseverance. Everton, one of the kindest person I have ever met. Hugo, Kimon, Roberto and Francesco, the "pastis"' gang who also loves running and skiing. Katee, Fito, Richard, Maria and Veronica, you guys are an inexhaustible source of fun and positivism. Gonzalo, Miren, Ana, Dani, Jesús and Jorge, my needed dose of Spanish culture. Seddik, Clément, Lucas, Matteo, Carlos, Jana and Aymeric, my lovely crew of random bullshit generator; thanks for all the stupid jokes, tasty food, "super safe" hikes, coffee breaks and funny memes. Bernhard, Cameron, Manu, Matias, Bruna and Martin, the rest of the BatM team who work hard, but also play hard. Sara, who supported me from the beginning of my journey in Grenoble. Alberto, Laura and Javi, even though we live so far apart, each of our reunions is an instant flashback to our childhood. Last but not least, my parents and my brother, who have been always there and never asked for anything in return.